# THREE-DIMENSIONAL ELECTRON TOMOGRAPHY OF INTEGRATED CIRCUIT DEVICES

A Dissertation

Presented to the Faculty of the Graduate School

of Cornell University

in Partial Fulfillment of the Requirements for the Degree of

Doctor of Philosophy

by

Peter Alexander Ercius

August 2009

# THREE-DIMENSIONAL ELECTRON TOMOGRAPHY OF INTEGRATED CIRCUIT DEVICES

Peter Alexander Ercius, Ph.D.

Cornell University 2009

The three-dimensional structure of integrated circuit (IC) devices can be analyzed at the nanometer scale by electron tomography using projection images generated from a scanning transmission electron microscope (STEM). The instrument samples the projected mass thickness of an object, producing image intensities with contrast capable of differentiating materials. Resulting three-dimensional reconstructions provide direct analytical analysis of structures with nanometer scale resolution along all three spatial dimensions for accurate predictions of device performance and reliability.

We apply electron tomography to reconstruct a 250nm-thick cross-section of Cu wires with Ta barrier layers and measure the conductor cross-sectional area at many points along the wire to calculate Cu resistivity. Measurements from traditional two-dimensional projection images underestimate conductor cross-sectional area due to the overlap of line edge roughness defects along the wire's length in projection. The average cross-sectional area determined from tomography measurements is 5% higher than a measurement from a two-dimensional projection of the same wire, resulting in significantly different predicted resistivities. Reconstruction of thick material cross-sections allows many measurements of device variations for a statistical analysis of critical dimensions.

Traditional STEM imaging techniques produce transmission functions with a non-monotonic dependence of intensity on thickness for thick cross-sections of common microelectronic materials, which is unsuitable for electron tomography. We introduce

a novel incoherent bright field (IBF) STEM imaging technique optimized to image cross-sections up to 1$\mu$m thick. Monte-Carlo simulations of beam scattering predict IBF-STEM is complementary to traditional incoherent STEM imaging techniques but provides superior signal-to-noise ratio and no image artifacts for ultra-thick specimens. We develop a general relationship from Monte-Carlo simulations and calculations of the Rutherford cross-section for elastic scattering that determines the suitable STEM imaging technique for any material thickness based on predicted signal-to-noise ratios.

To test IBF-STEM's suitability to electron tomography, we reconstruct a stress-void in a 250nm thick Cu wire, where traditional imaging techniques fail to provide monotonic image intensities at all tilt-angles. Experimental STEM images of the ultra-thick cross-section verify the expected transmitted electron intensity from Monte-Carlo simulations of STEM detectors with different collection angles. An IBF-STEM reconstruction provides the location and size of a stress-void in three-dimensions that is not possible with two-dimensional projection images alone.

## BIOGRAPHICAL SKETCH

Peter Ercius was born in Ann Arbor, MI to Dr. Mark and Kay Ercius, and subsequently lived in Texas, California and Arizona. He has two younger sisters who lived with him in Scottsdale, Arizona until Peter graduated from Chaparral High School in 1999. He made the long journey from the desert to the snow covered hills of Ithaca, NY to attend Cornell University with the goal of studying engineering. Four years later - after many problem sets, pre-lims, finals and soccer games - Peter graduated from Cornell with a Bachelors of Science in Applied and Engineering Physics. The gorges, soccer and academic rigor of the School of Applied and Engineering Physics were too much to resist, and Peter decided to stay in Ithaca for graduate school. He joined the research group of Dr. David Muller to study electron microscopy with applications in microelectronics. He focused on three-dimensional imaging of nanometer scale structures using electron tomography and a scanning transmission electron microscope. Peter met the love of his life, Kimberly Ehrlich, in 2005, and the two were married four years later on May 2, 2009. Soon after, Peter graduated with his Ph.D. in applied and engineering physics nearly 10 years after first arriving at Cornell University. Peter plans to continue his research with electron microscopes at the National Center for Electron Microscopy at Lawrence Berkeley National Laboratory until they finally become too nervous entrusting him with multi-million dollar research instruments.

To my family for always supporting me in every way possible.

## ACKNOWLEDGEMENTS

I feel very privileged to have studied at Cornell University for the past 10 years. The university has led me to my goal of a doctorate in physics and provided a rich community of people that I will never forget. So many people helped me throughout my college and graduate career, and I am pleased to acknowledge as many as possible.

None of this would have been possible without the academic and monetary support provided by Professor David Muller. He challenged me with constructive criticism and great ideas constantly to improve my research and writing abilities such that I never take data or submit an article without first ”seeing” it through his eyes. He is a wonderful Ph.D. advisor, allowing students to pursue their ideas while asking the right questions to keep them grounded in reality. I express my gratitude for his great support.

I sincerely thank Professors John Silcox and Jack Blakely for agreeing to sit on my thesis committee and read my thesis. Professor Blakely’s graduate classes and Professor Silcox’s knowledge in electron microscopy were very helpful during my research here at Cornell.

Professor Bruce Kusse has been a great friend and inspiration to myself since I was a sophomore in his mathematical physics class. His teaching, wisdom and friendship have made my journey from undergraduate to Ph.D. possible and memorable. He taught me everything from Green’s functions to how to change the oil in my 1998 Jeep Cherokee. He has been one of my most important supporters, and I could not have finished my graduate work without him.

Dr. Lynne Gignac and Dr. Bob Rosenburg from the IBM T.J. Watson Research Laboratory provided much needed support through the Semiconductor Research Corporation. Getting samples from industrial labs sometimes seems like pulling teeth, but these two eagerly provided samples relevant to the microelectronics community for all of the tomography work presented in this thesis. Lynne has also served as my mentor

with respect to industrial research and hosted many visits to the IBM facilites for very useful discussions and networking opportunities. I thank both Lynne and Bob for all of their support with my research and career.

Matthew Weyland was the first post-doctoral researcher in the Muller group at Cornell University, and therefore functioned as the senior graduate student for the new group. He spent more time training, teaching and helping to fix my own problems than on his own research. He taught me almost everything I know about STEM, electron tomography and British slang. My research would not have been possible except for his expertise, and I thank him for sharing that with me.

My fellow Muller group graduate students - Lena, Jerome, Aycan and Judy - all challenged me to produce better results by their own high quality research. Our discussions regarding anything both scientific and not kept even our windowless basement office a pleasant place to spend 6 years (although our first corner office upstairs was much better). I hope to collaborate with them in future research and continue our friendships outside of the laboratory. I have also very much enjoyed teaching Huolin everything I knew about tomography and seeing him quickly surpass my skills. He is always curious and energetic about microscopy, which I hope never changes. It has been a pleasure sharing knowledge with Rob, Julia and Pinshane. See you guys at future M & M conferences!

In Ithaca, my friends Paul, Rick, Julia, Dave, Pace and Heidi deserve lots of credit for keeping me normal and providing an outlet from graduate studies. Maybe someday we will all end up living near one another again and find another delapidated ”tilty” house - leaning at least 10° into a gorge - to continue our escapades.

My soccer habit was fueled by the excellent league of players in the local Ithaca United Soccer Club (IUSC). I learned much about soccer and leadership from Josh, Dan, Lisa, Tom, Anthony, Emily, Sarah, Zach, Phil, Kahled, Martin, Jano and many

MANY more during my 10 years in the league. Some of my best friendships evolved out of friendly soccer rivalries at Cass Park. Real Ithaca and the Homeboys: thanks for all of the championships!

I thank Evan, Sian, Chris, Bryon and Michelle for never losing touch even though I lived so far away from Scottsdale. They were always there to hang out when I went home and to provide encouragement to finish my Ph.D.

My parents have supported me tremendously throughout my academic career. They sparked my curiosity and work ethic which allowed me to reach this final goal. They told me on move-in day in August 1999, ”You can come home to Arizona anytime if you don’t like it here!” Even though I missed them tremendously, I stuck it out in Ithaca through sub-zero temperatures, snow, rain, canceled airline flights and lost baggage. Hopefully, I can convey a small part of my gratitude for all of their support, but I doubt there is enough space in this entire thesis to do so.

I grew much closer to my sisters, Anna and Krista, once we all entered college and realized we are actually very similar. They helped keep me grounded while home for the holidays away from graduate school, and they even visited Ithaca. Their support (current and future) means a lot to me.

Finally, meeting my wife Kim was one of the best parts of my entire Cornell experience. Even when work piled up, deadlines approached and papers needed writing, she always makes me feel like life is great. She endured endless conversations regarding vacuums, electron orbitals, broken microscopes and diffraction imaging at dinners with our research group and even managed to put the Muller group website on the first page of Google. She has supported me in this very long, complicated and confusing graduate school process while always keeping me pointed towards the light at the end of the tunnel: graduation. I love you with all my heart and look forward to the next chapters in our lives together.

## TABLE OF CONTENTS

## LIST OF TABLES

## LIST OF FIGURES

CHAPTER 1

# INTRODUCTION

The measurement and analysis of integrated circuit (IC) devices with reduced, or scaled, dimensions is critical to the further advance of computer chip technology by ensuring actual device performance matches the expected parameters used in circuit designs. Each new technology node, as detailed by the International Technology Roadmap for Semiconductors (ITRS) [1], produces smaller and denser circuits such that defects at or below the one-nanometer scale will affect the performance of devices 10 – 50nm in size. For example, roughness at material interfaces has remained at the same absolute value but now represents a larger percentage of critical device dimensions in scaled devices. The necessity to characterize increasingly fine, dense features has reached the resolution limits of traditional metrology techniques, and new methods will be necessary to analyze device failures and structural variations with nanometer resolution.

Scanning electron microscopes (SEM) are commonly used to image and measure critical dimensions of IC structures on a wafer surface, but the technique lacks the resolution required to investigate aggressively scaled features. Transmission electron microscopes (TEM) offer quantitative two-dimensional projection images with atomic scale lateral resolution, but require 10 – 50nm thick material cross-sections to minimize electron multiple scattering that degrades resolution. For past technologies, these cross-sections were considered thin compared to the features of interest but may contain significant portions of modern devices resulting in insufficient sampling. Rough material interfaces and densely patterned features will overlap in projection to produce complex, sometimes inaccurate, representations of the original structure. New metrology methods that offer measurements along all three-dimensions of a sampled volume

provide for full, accurate device characterization of modern IC technology, which now exhibit characteristic length scales << 100nm.

This thesis focuses on the use of a scanning transmission electron microscope (STEM) to produce quantitative, three-dimensional reconstructions of IC devices using electron tomography (ET) [2, 3]. Traditional STEM images are only two-dimensional projections of the sampled volume, and the overlap of features along the projection direction can produce a complex representation of the device structure. ET extracts the lost information in the projection direction from a series of projection images assuming a monotonic relationship between intensity and material thickness. The resulting quantitative three-dimensional reconstruction exhibits up to 1nm resolution capable of material phase differentiation for accurate measurements of critical device dimensions along any spatial dimension. Chapter 2 compares measurements made from three-dimensional ET reconstructions and traditional STEM projection images of relatively thick (250nm) cross-sections containing Cu, Ta and Si. Feature overlap in projection affects measurements of the extended structure contained within the sample thickness, but ET allows many accurate measurements of device variations. ET therefore provides an efficient method to measure and analyze variations within and between IC devices for an accurate prediction of circuit performance [4].

Traditional TEM imaging techniques can fail to provide proper image contrast for accurate ET reconstructions due to the highly-scattering, crystalline nature of materials commonly used in IC devices. In Chapter 3, TEM experiments and Monte-Carlo (MC) electron scattering simulations investigate these phenomenon to determine the reliability of ET reconstructions. We develop the novel incoherent bright field (IBF) STEM imaging technique optimized for reconstruction of ultra-thick material cross-sections. ET data acquisition, post-processing and analysis are considered very time intensive, and

reconstruction of large portions of a structure efficiently sample device variations [5]. The IBF technique was initially developed as a replacement for ADF-STEM imaging to provide artifact-free projection images of ultra-thick cross-sections possibly affected by contrast reversal. We show that IBF imaging conditions are superior in ultra-thick samples even before ADF-STEM reverses contrast, which provides well defined material feature boundaries for accurate structural measurements. We use the SNRs of the ADF and IBF STEM techniques as a measure for image quality to produce a general relationship determining when each method is better suited for imaging any material at a given thickness.

Chapter 4 compares the capabilities of two STEM projection imaging techniques for ET of IC devices: traditional high-angle annular dark field (HAADF) and IBF-STEM. A stress-void in a 250nm wide Cu interconnect with TaN/Ta barrier layers is reconstructed by both methods. Artifacts included in HAADF-STEM images propagate into the reconstruction, but the novel IBF-STEM imaging technique provides an accurate representation of the actual sampled structure [5].

## 1.1 The History and Evolution of Interconnects

The semiconductor industry has continually produced faster and more powerful computers by increasing the number of electrical devices integrated into a single chip. Gordon Moore, one of the founders of the Intel Corporation, predicted that the number of active devices per unit area on a computer chip would double every two years in his now famous 1965 article in *Electronics* magazine [6]. The majority of public emphasis regarding continued technological advancement is placed on the shrinking dimensions of active transistors, but less appreciated are the many wires necessary to properly connect together the source, drain and gate of each transistor. These interconnections now con-

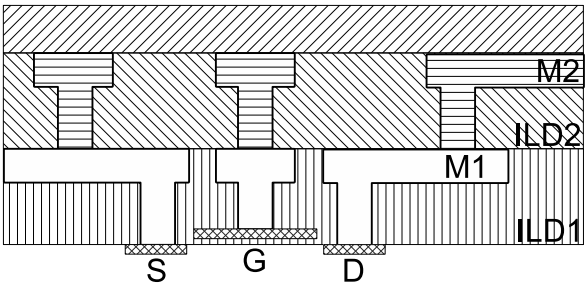


Figure 1.1: A diagram of a two level interconnect system connecting the source (S), gate (G) and drain (D) of a transistor. In-plane wires and vertical inter-layer *vias* form each level of interconnects and are labeled M1 and M2. Interlayer dielectrics (ILD) isolate each conducting wire from surrounding structures.

sist of an incredibly complex network of wires known as the back-end-of-line (BEOL), which contributes significantly to the overall performance, power consumption and heat generation of modern microprocessors. Figure 1.1 shows a two level system of interconnects indicating the complex structure created by BEOL connections and the active transistor elements. Scaling, or shrinking, of features produces opposite effects for the switching delay produced by the transistor and BEOL structures such that interconnects could potentially obstruct future scaling according to Moore's law. Transistor switching speed generally increases inversely to gate oxide thickness and channel length, but resistor/capacitor (RC) charging delays signal propagation along dense, scaled BEOL structures. As an example, very old technology built with a 1$\mu$m minimum feature size produced nominal extra delay of ~1ps for signal propagation between devices compared to the ~20ps transistor switching speed. Current 0.035$\mu$m technology exhibits vastly increased wire delay of ~250ps compared to a ~1ps transistor switches [1]. Also, power consumption due to resistive heating in interconnects recently surpassed 50% in 2007 and is expected to increase up to 80% with increased processor frequency and interconnect density. Research devoted to integrating new materials, optimizing existing

processes, and developing novel device architectures to solve BEOL performance issues is critical to the advancement of computer technology.

A necessary partnership exists between the computer engineers designing circuits and the materials engineers building devices at the nanometer scale. Circuit designs must reflect the expected capabilities of the current IC devices produced from a large range of interconnected processing tools manufactured by many different companies. During process development, materials engineers must build, measure and control device parameters while comparing results to the expectations of the entire industry. Metrology, the measurement portion of the processing cycle, provides valuable feedback of actual device composition allowing defect analysis and an accurate prediction of performance and yield for large scale integration. No structure is free from defects at the nanometer scale, and adequate sampling of device variations provides an accurate prediction of performance and reliability. Electrical and mechanical properties of materials in nanoscale features diverge from bulk-like expectations due to quantum effects and the mean-free-path of conduction electrons, which poses significant challenges for metrology to provide accurate (possibly atomic!) measurements of critical dimension with adequate sensitivity to real process variations. The success of future microelectronics devices requires unprecedented uniformity in large scale manufacturing of the nanoscale features.

### 1.1.1 Early Aluminum Metallization for IC Devices

The first metal connections between the active devices in IC circuits were created with Al and only required a single two-dimensional plane for the entire wire network. Al exhibits a resistivity of 2.7$\mu\Omega$cm, which is not the lowest among metals, but only re-

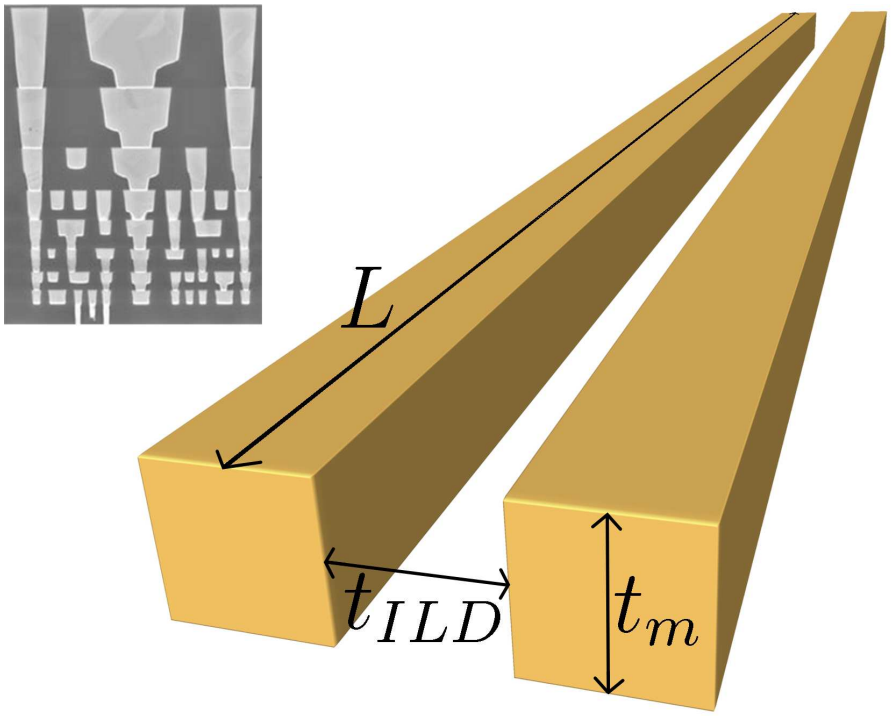


Figure 1.2: The inset SEM image shows the varying size of eight levels of interconnects in cross-section. The smallest interconnects at the bottom carry signals between neighboring devices, and large wires near the top carry long-range global signals between remote areas of the chip. The larger perspective diagram shows two parallel interconnects labeled with the critical dimensions that affect resistance/capacitance (RC) delay calculations in equation 1.1.

quires simple dry processing techniques for deposition and patterning. Feature scaling for improved processor performance leads to denser structures such that a single two-dimensional plane provided insufficient space for all of the necessary interconnections. Consequently, multiple wire layers linked by vertical inter-layer *via* connections were added to distribute power and signals across the entire chip.

Al interconnects presented several fundamental problems associated with increased current density and denser interconnect networks. The BEOL network consists of small

parallel wires separated by a thin interlayer dielectric (ILD) for signal isolation, which effectively creates many parallel plate capacitors. Signals propagating along densely packed interconnects are therefore significantly delayed according to the RC time constant for charging the capacitor-like structure. The effective wire resistance is multiplied with the formula for a simple plate capacitor to estimate the RC wire-to-wire delay by the equation

$$RC = \frac{\rho}{t_m} \frac{L^2 \epsilon_{ILD}}{t_{ILD}} \tag{1.1}$$

where $\rho, t_m, L, \epsilon_{ILD}$ and $t_{ILD}$ are the resistivity, layer thickness, interconnect length, interlayer dielectric (ILD) permitivity and ILD thickness respectively [7]. Figure 1.2 shows a diagram of two parallel interconnects labeled with each of these parameters. It is apparent from equation (1.1) that the RC time constant varies inversely with the distance between interconnects ($t_{ILD}$) leading to increased delay times for denser structures. Interestingly, equation (1.1) does not depend on the wire width $W$ alone which encourages high aspect ratio (calculated as $L/W$) features to increase the conductor cross-sectional area. Direct connections between active transistors require similarly scaled interconnects separated by the minimum attainable distance for a given technology generation, but utilizing such small wire dimensions uniformly across the entire chip introduces excessive communication delay between remote circuit blocks, which effectively negates transistor performance gains. The solution involves multi-level interconnections (MLI) of varied length and cross-section for improved performance and design flexibility. A dense local wire network separated by the minimum feature size connect neighboring devices organized into functional circuit blocks. Larger cross-section wires enable long-range global communication and power distribution across the chip with minimal delay. The RC time constant of the interconnects in each level were properly balanced with their length $L$ as necessary by equation (1.1) allowing the interconnect network to integrate with high-performance transistors. The upper-left inset of Figure 1.2 shows eight

levels of interconnects in cross-section (the ninth bottom level adds direct connections from the interconnect network to the active devices) indicating the relative varied cross-sections of local, intermediate, and global interconnects.

A problem known as electromigration affected Al interconnect lifetimes as increased current density subjected the metal to large electric fields in a constant direction [8, 9]. Al atoms tend to migrate along fast diffusion paths with low bonding energies, such as material interfaces and crystal grain boundaries, aligned with the flow of electrons resulting in the formation of ”upstream” voids. Atom migration had always occurred, but material loss in smaller interconnects amounts to a greater percentage change of total metal volume which increases the risk of interconnect failure due to high resistance and open circuits. The Al network utilized an $SiO_2$ ILD, which conveniently forms a well bonded, self passivating oxide at an interface with Al. Such high bonding at this interface left the crystal grain boundaries as the only possible fast diffusion path. A 100 year old age-hardening technique well known in macroscopic metallurgy [10] suggested introducing trace amounts of Cu into the Al to form an Al/(Cu) allow. Cu precipitates form in the Al lines and Cu decorates the alloy crystal grain boundaries, which both block dislocation movement to effectively impede electromigration [11].

Even with advanced Al processing techniques, BEOL researchers needed to replace Al with a less resistive metal to match transistor performance gains in further scaled devices. Only Ag, Cu and Au provide superior resistivities at $1.6, 1.7$ and $2.2 \mu\Omega$cm respectively, but traditional Al processing techniques are incompatible with these metals necessitating a completely innovative approach.

### 1.1.2 Modern Copper Metallization and the Dual-Damascene Process

In 1998 IBM released the first commercial products to take advantage of Cu metallization with a 0.22$\mu$m minimum feature size after ten years of development [12, 13]. Cu introduced significant improvements over older Al technology specifically pertaining to lower susceptibility to electromigration and lower interconnect resistance for decreased RC delay, power consumption, and resistive heating. Critical innovations included electroplating for Cu deposition [14, 15], chemical mechanical polishing (CMP) for wafer planarization [16–18] and reliable barrier materials to control Cu diffusion and adhesion. These innovations introduced new problems and required new metrology techniques to continue the iterative "build, measure, and improve" cycle of fabrication process improvement. Also, feature scaling demanded higher resolution metrology techniques for proper device analysis, such that three-dimensional analytical techniques are now needed to fully analyze complex, dense IC structures [11].

IBM's innovative bottom-up Cu metallization process is called Damascene and is similar to an artwork form of the same name involving inlaid metal patterns. A single interconnect layer consists of a pattern of in-plane wires and vertical vias, which can be fabricated in two separate etching steps each followed by Cu deposition and CMP planarization. The more efficient dual-Damascene technique currently in production involves simultaneous fill of sequentially patterned wire trenches and vias to halve the steps per metallization layer resulting in significant time and cost savings. This process, diagrammed in Figure 1.3, begins with the deposition of a thick ILD layer with a low dielectric constant (such as $SiO_2$) used to isolate individual metal lines. The first lithography/etching step (see Suzuki, et al [19], Madau [20] or Campbell [21]) creates the trench pattern for in-plane connections, and the second lithography/etching step adds

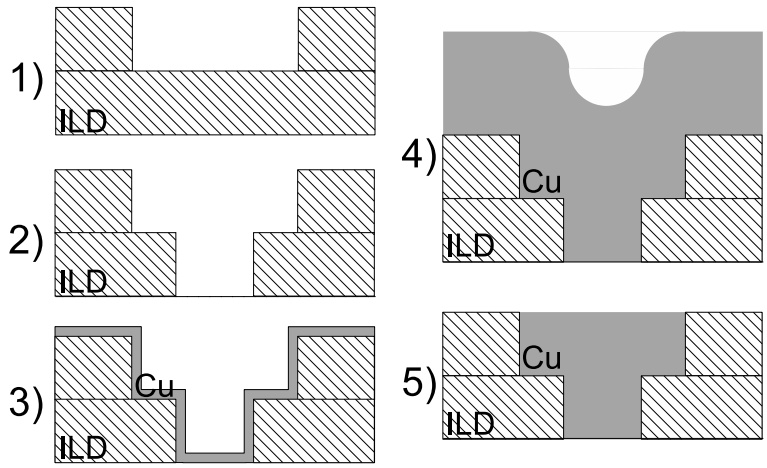


Figure 1.3: A diagram of the dual-Damascene process used for Cu metallization of modern interconnects. 1) & 2) A thick film of inter-layer dielectric (ILD) is first deposited and then patterned by two lithography/etching steps to create trenches for Cu fill. 3) A thin, continuous and conformal seed layer is evaporated by physical vapor deposition to promote void-free Cu deposition. 3) The Cu is then electroplated to overfill the ILD trenches with an *overburden*. 5) This overburden is then removed using chemical mechanical polishing (CMP) to achieve a planarized surface. The process is repeated to construct up to 11 interconnect layers in modern processors with each subsequent layer aligned to the previous layer.

round via holes for vertical inter-layer connections. A thin, conformal coating of Cu is then evaporated (by physical vapor deposition (PVD) for example) to produce a continuous seed layer for subsequent void-free Cu Damascene deposition. Next, the entire wafer is placed in an electrochemical plating bath to grow a thick conformal Cu layer that completely fills trenches and high aspect ratio via holes without voids or seams. The Cu is allowed to overfill the trench network to account for the conformal nature of the final thin film. Finally, a grinding process of chemical mechanical polishing (CMP) employs an abrasive pad and chemical slurry working in tandem to remove this excess Cu *overburden*, which planarizes the wafer surface in preparation for the next inter-

connect layer. After step 5) in Figure 1.3, a Cu filled interconnect network of planar wires and vertical vias remains according to the original etched pattern. The process is repeated with each layer aligned to the previous layer to build up a three-dimensional interconnect network for signals and power distribution across the entire chip. The steps can be rearranged and otherwise modified to optimize the process for different processing requirements such as resolution, alignment tolerances and line pitch among many other parameters [7]. Also, the simplified dual-Damascene process described here does not include barrier layers normally deposited between before the Cu seed for improved adhesion and resistance to Cu migration (see sections 1.2.1 and 1.2.2).

Computer chip performance and reliability greatly improved due to Cu metallization, but it also created new problems that could disrupt the industry's aggressive scaling schedule [1]. Though not furthered covered in this thesis, many technical hurdles were overcome to develop the Cu dual-Damascene process including optimization of the electrochemical bath for Cu deposition, a continuous PVD Cu seed layer, and CMP for efficient Cu overburden removal without contamination [13–15, 22]. This thesis instead focuses on measurements of nanoscale features buried inside microelectronic devices to predict their performance and reliability.

## 1.2 Defects in Scaled Copper Interconnects

A very basic principle of microelectronic fabrication is the precise control of the location and electrical properties of materials within very small tolerances, but the ability to accurately deposit materials with high precision is futile if significant material diffusion occurs over the lifetime of a component. Over time, diffusion has always lead to eventual device contamination and structural defects, but what constitutes a "device killing"

defect is now much smaller due to scaling [7]. Advanced metrology techniques capable of analyzing structures at high resolution are necessary to ensure devices conform to the tight tolerances required for proper operation.

### 1.2.1 Interactions Between Copper and Silicon

Cu is a well known interstitial contaminant in Si with high diffusivity and reactivity, which presented a serious problem for integration with Si processing. Cu atoms introduce unwanted energy levels deep in the Si conduction band, leading to various transistor failure mechanisms. The deep levels act as generation-recombination centers reducing electron mobility during the ”on” state and can assist electron tunneling contributing to wasteful leakage current during the ”off” state. Cu impurity energy levels also trap electronic charge within the transistor modifying charge distribution and capacitance that can produce unpredictable device behavior. In-depth treatments of these defects are offered by Taur [23] and Sze [24] for a better understanding of the extreme tolerances required in modern IC devices.

Unlike Al, Cu does not reduce the $SiO_2$ ILD to form a strongly bonded interface. Incorporating Cu into Si technology requires the addition of barrier layers compatible with both materials to control diffusion and adhesion properties at all four Cu/ILD interfaces as diagrammed in Figure 1.4. The *capping* barrier material (deposited after CMP for each dual-Damascene metallization process) extends continuously across each metallization level and possibly provides a conduction path between all in-plane interconnects. This barrier must be insulating to avoid shorting all wires together. Adhesion at the Cu/dielectric interface is not particularly strong and has become the main cause of interconnect failure as described in later sections. The barrier material at the other

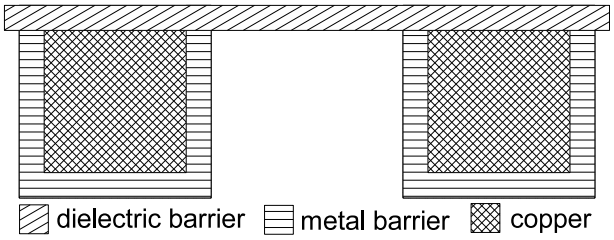


Figure 1.4: A diagram of the barrier layers surrounding Cu interconnects. Barriers are necessary to promote adhesion between the Cu conductor and surrounding ILD (not shown) and to prevent Cu diffusion into the active areas of transistors. The top *capping* barrier must be a dielectric to eliminate a possible short-circuit conduction path between all wires in a metallization layer. The metal barrier necessarily exhibits higher resistivity compared to Cu and displaces some cross-sectional area of the wire, which negatively impacts the overall current carrying capacity of the interconnect.

three interfaces (known as the *liner*) displaces a portion of the allowable interconnect cross-section, which decreases the volume available for low resistance Cu. A metallic liner material with a relatively low resistance provides a redundant electrical path that minimizes the impact to the overall current carrying capacity of the interconnect structure. Even so, it is desirable to minimize the metal liner thickness relative to the overall wire cross-section without impacting the effectiveness of the layer as a physical diffusion barrier and adhesion promoter. Scaling this layer for future technology is difficult and requires deposition of nanoscale layers with continuous conformal coverage of high aspect ratio interconnect trench and via structures. Research into novel ultrathin or zero-thickness barriers is of increased importance, but successful barrier design that simultaneously promotes adhesion and controls diffusion involves many parameters that restrict the potential materials to few options (see table I in Edelstein, *et al* [25]). Metrology techniques capable of assessing the conformal coverage and effectiveness of

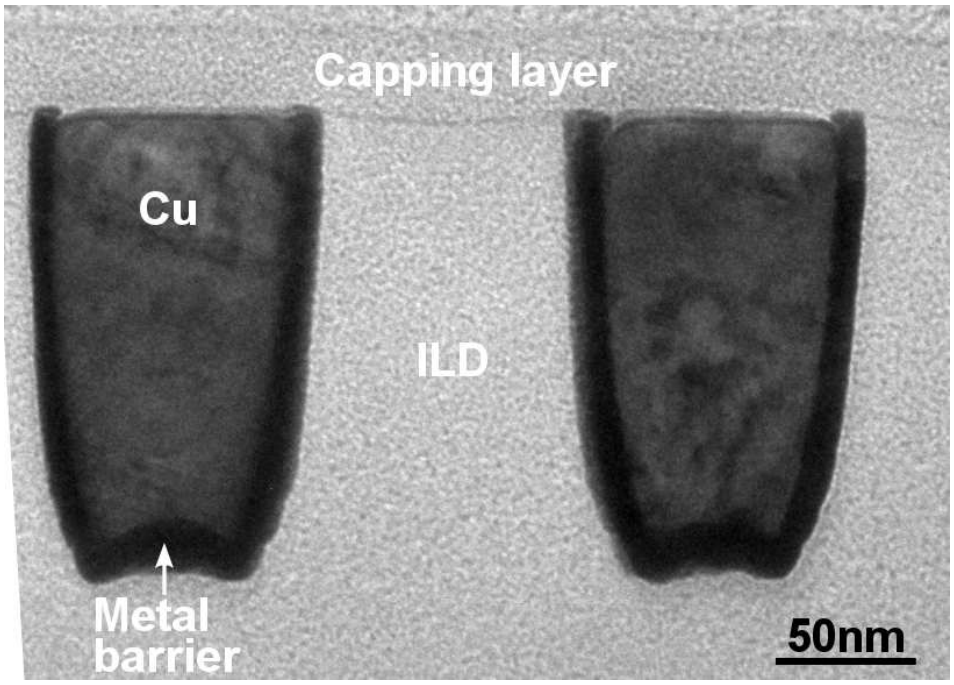


Figure 1.5: Image of a real Cu/barrier/ILD interconnect structure from a conventional transmission electron microscope. Darker pixels indicate regions with higher $Z$ numbers such that the metal barrier (barrier 2) is much darker than the other elements. The capping dielectric barrier (barrier 1) is also apparent in this image.

metallic barriers require material differentiation with nanometer scale resolution in all three spatial dimensions for full structural characterization.

Figure 1.5 is a conventional transmission electron microscope image (see section 1.4.1) of an interconnect structure showing two adjacent Cu interconnects in cross-section. The i) Cu is surrounded on three sides with a ii) metallic Ta liner and topped with a iii) SiC dielectric capping layer to avoid shorting the wires together. Ta was chosen as the metallic liner because it exhibits no solubility in Cu, and no known Cu–Ta compounds form even after annealing the metals at 600C [26]. For this specific technology node (current in ~2006), the 10nm Ta barrier was deposited by physical vapor

deposition (PVD) and occupies ~22% of the allowable 90nm interconnect width. The liner thickness is difficult to scale with the wire width for more advanced interconnect technology, which has spurred development of zero-thickness barrier materials to maximize Cu conductor contained in interconnects to support sufficient current density for denser transistor structures.

### 1.2.2 Electromigration Defects in Copper Interconnects

Electromigration is the enhanced transport of metal atoms along the direction of current flow due to momentum transfer between metal atoms and electrons flowing within the wire. Significant depletion of metal atoms from ”upstream” regions with high current density can cause open circuit connections with a significant impact on device lifetimes. The effect was first encountered in Al metal wires where crystal grain boundaries provided the fast diffusion paths (see section 1.1.1), and the phenomenon now limits Cu interconnect reliability due to multiple Cu atom migration paths. Also, the effect is enhanced as the interconnect current density increases with decreasing wire dimensions, which limits the allowable current available to circuit designers for circuit operation. Figure 1.6 shows a diagram of a polycrystalline Cu wire with a SiC dielectric capping layer and metallic Ta liners. Arrows indicate electromigration fast paths along the direction of current flow for the metal/cap interface, metal/liner interface and Cu grain boundaries. Cu metallization has produced significant improvements in electromigration over older Al metallization technology, but the phenomenon must be minimized to yield sufficient Cu reliability for extremely scaled devices.

Cu grows in a polycrystalline phase during electroplating as seen in figure 1.7a), and the grain microstructure has a large impact on the electromigration performance

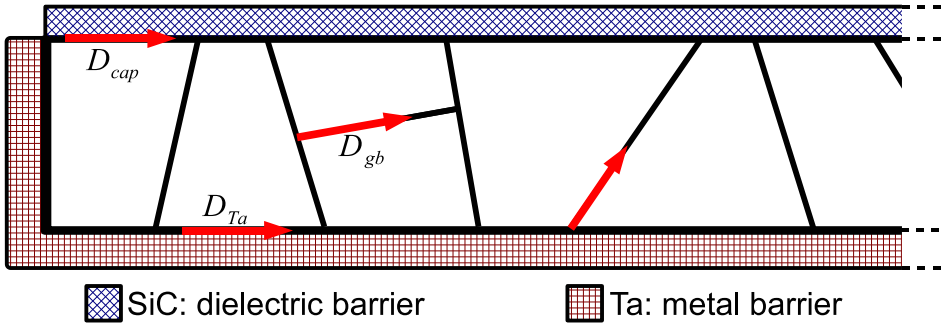


Figure 1.6: Diagram of a polycrystalline Cu layer in cross-section showing various electromigration diffusion paths. $D_{cap}$ represents electromigration at the interface of the dielectric barrier cap (usually made of a SiC derivative) and Cu conductor. $D_{Ta}$ represents electromigration along the metal/Ta barrier interface. $D_{gb}$ represents electromigration along the Cu grain boundaries. The ideal bamboo-like grain microstructure provides no grain boundaries aligned with electron flow, but real Cu grains will always deviate from the desired structure. Even so, each bamboo-like grain significantly hinders further atom migration along a wire.

of interconnects. Figure 1.7b) shows the desired microstructure consisting of large Cu grains with grain boundaries mostly perpendicular to electron flow known as *bamboo-grained* microstructure, which nearly eliminates grain boundary fast diffusion paths. The microstructure of electroplated Cu is known to rapidly evolve over time even at room temperature, and a low-temperature thermal anneal is commonly used to equilibrate the microstructure while promoting the growth of bamboo-like grains [27]. The interconnect width also affects the attainable grain microstructure such that very wide Cu wires $> 1\mu$m tend to have multiple grains within a wire width, but narrower lines support single bamboo-like grains across the wire width. Cu microstructure tends to deviate from bamboo-grains for wire widths $<$ 45nm that approach the median Cu grain size, which may impact Cu metallization reliability in future technologies [28].

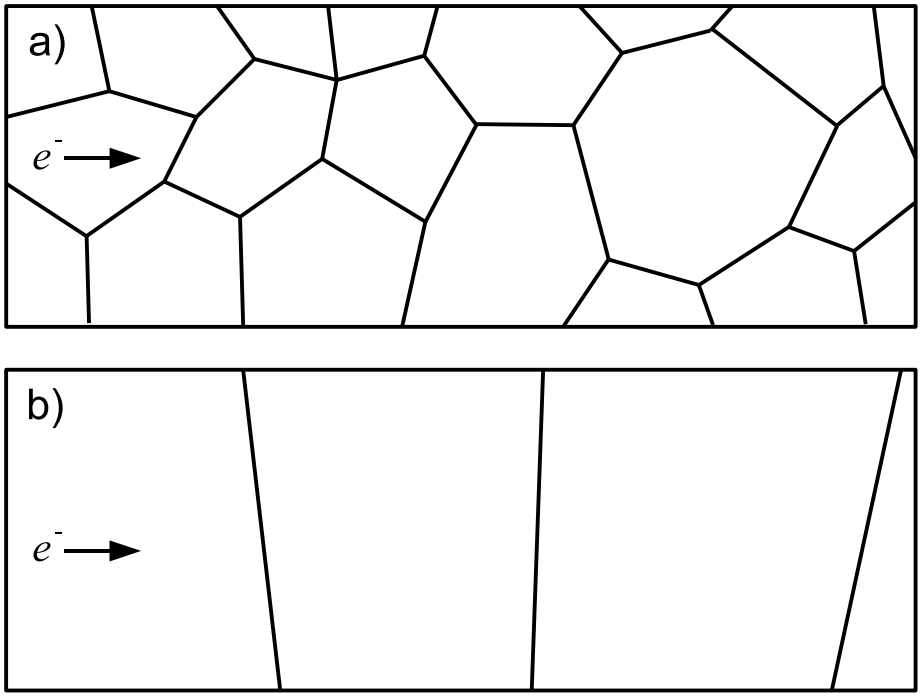


Figure 1.7: Diagram of two polycrystalline Cu films with very different microstructures where lines indicate crystal gain boundaries. a) Polycrystalline Cu with randomly oriented grain boundaries and small average grain size. The grain boundaries are fast diffusion paths electromigration. Such atom diffusion promotes void growth which may eventually result in open circuit failure. Thus, scaled interconnects exhibit reduced lifetimes. b) Bamboo-grained microstructure has crystal grain boundaries perpendicular to electron flow and large average grain size. This desired microstructure minimizes voiding of ”upstream” structures due to Cu atom electromigration along grain boundaries parallel to the flow of electrons.

For bamboo-grained Cu, the relatively weakly bonded metal/barrier interfaces provide surfaces parallel to the flow of electrons for fast atom migration, and Cu adhesion is the most important parameter for extending interconnect lifetimes [29–31]. In fact, the metal liner consists of a bi-layer structure made of Ta and TaN to further strengthen this interface. The TaN layer adheres well to the ILD (but not Cu) and the Ta layer adheres well to the Cu (but not the ILD). The liner deposition only requires a single step PVD process enhanced with N where the N supply is simply turned off to create pure Ta. The bi-layer metallic liner guards against Cu diffusion out of the interconnect, adheres well to both Cu and ILD to minimize electromigration and provides a relatively low electrical resistance with limited impact on the overall wire performance. The TaN/Ta barrier has persisted through many generations of interconnect technologies, because it uniquely satisfies all necessary adhesion and atom migration properties for successful Cu integration without compromising other important electrical attributes. The metal liner also provides a redundant electrical connection that delays or avoids open circuit device failure in the event of extensive Cu voiding. Table I in Edelstein, *et al* [25] shows the properties of many different barrier materials originally considered for Cu integration at IBM, and indicates the extensive testing necessary to engineer this effective material.

Thus, the capping dielectric barrier provides the dominant electromigration path ($D_{cap}$ in figure 1.6) for bamboo-grained Cu interconnects lined with a TaN/Ta bi-layer liner, and its exact composition is often modified between technology generations to increase Cu adhesion [1]. The dielectric cap may be replaced with a metallic material (such as CoWP) that exhibits interface bonding energies similar to bulk Cu values to drastically reduce electromigration at this interface [32, 33]. A cost-effective manufacturable process is difficult to implement; however, because the metal cap must be selectively grown only on the Cu wires or patterned in a separate process. Also, early

(published) results indicate cobalt diffuses into the Cu wires yielding increases in overall wire resistance [34].

### 1.2.3 Stress-Induced Voiding in Copper Interconnects

The migration of Cu vacancies due to mechanical stress known as stress-induced voiding (SIV) or stress migration (SM) is another major concern for the reliability of Cu interconnects [35, 36]. This phenomenon is poorly understood compared to electromigration, but it is believed that mechanical stresses associated with thermal expansion due to local resistive heating during normal power cycling of devices drives Cu vacancy diffusion within the wire. Mismatched thermal expansions of the materials that make up interconnect structures (Cu, dielectric cap, metal liner and ILD) strain the interfaces between these materials, and the regions where vertical Cu vias meet in-plane wires are common void nucleation sites [36]. Figure 1.8 shows a diagram of the affected structure and the location of a stress-induced void that commonly causes open circuit electrical failure. This problem involves the complex relationships between the materials, the processing conditions and the exact via-to-wire geometries used for any given experiment. Investigations of numerous test geometries and processing temperatures are necessary to fully explore the range of parameters that affect SM [36–38].

Sufficient vacancies capable of diffusing to a nucleation center must exist in the material for SM to create a void large enough to disrupt electron flow. The exact vacancy creation process is unknown, but many Cu vacancies may be created by mechanical stress placed on the entire IC structure during the abrasive CMP process. Also, additional vacancies are produced during thermal anneals - promoting bamboo-grained microstructure - applied after deposition of the dielectric capping layer, because grain

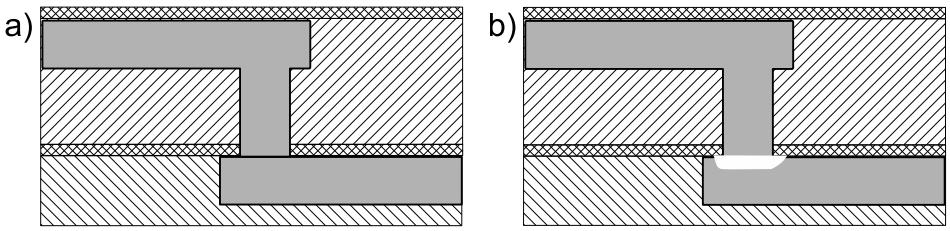


Figure 1.8: a) Diagram of the via-to-wire structure commonly affected by void coalescence due to stress-induced migration. Mechanical stresses provided by resistive heating including strain from thermal mismatch of thermal coefficients allows vacancies to migrate within the Cu interconnect. b) Void growth occurs which can lead to circuit failures due to open connections.

boundaries are eliminated allowing more efficient grain packing. Normally, excess vacancies escape the material at a free surface during thermal annealing, but barriers constrain interconnects on all sides effectively trapping vacancies within the Cu. Subsequent fabrication of another interconnect level introduces stress gradients concentrated beneath via-to-wire connections that attract vacancies, and stresses produced during normal IC operation drive vacancy diffusion, which may eventually coalesce into large voids [36, 39].

### 1.2.4 Metrology for Extending Interconnect Lifetimes

Investigations of the location, morphology and evolution of different types of EM and SM voids may determine the factors that drive atom migration and vacancy coalescence. Measurements of via-to-wire structures, the initial grain microstructure, and the final grain geometry can all yield important information about defect formation, but the three-dimensional nature of these nanometer scale structures is difficult to ascertain with traditional metrology techniques. TEMs produce two-dimensional projections

with sufficient resolution to guess at the void geometry, but three-dimensional analysis is necessary to determine more in-depth information such as the initial location of void coalescence. Chapter 4 analyzes a SM void near a via-to-wire connection in three-dimensions using ET. Changes to the geometry, material or fabrication parameters of interconnect structures susceptible to EM and SM could significantly extend Cu metallization lifetimes to the end of the ITRS roadmap [1].

## 1.3 Copper Resistivity and Size Effects

Unexpected performance challenges have arisen as BEOL wire dimensions approach an electron's mean-free-path in Cu [40, 41]. The performance of a wire as a conductor of electricity is affected by electron scattering from Cu impurities/defects, grain boundaries and interface roughness. A wire's average resistivity $\rho$ is an intrinsic property of the conducting structure that determines the resistance $R$ of a known length $L$ and cross-section $A$ by the relation

$$\rho = \frac{RA}{L} \tag{1.2}$$

Materials processing steps (such as lithography, etching and deposition) introduce local deviations from the desired smooth walls, known as line edge roughness (LER), with a negative impact on wire resistance due to increased nonspecular electron scatter at Cu/barrier interfaces [40] Interconnect designs initially assumed a constant bulk-like resistivity value $\rho$, and therefore line resistance $R$ solely increased due to geometrical effects of shrinking wires. Recent studies - such as Gignac, *et al.* [41] - show that resistivity rapidly increases inversely to cross-sectional area, colloquially referred to as the *size-effect* (see figure 1.9). LER structural variations are no longer negligible compared to critical device dimensions and must be considered in order to predict device per-

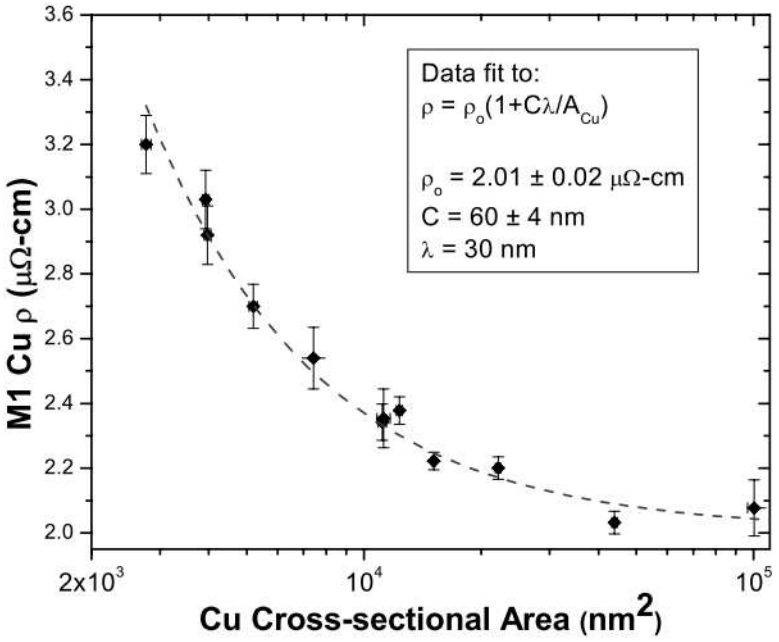


Figure 1.9: From Gignac, *et al.* [41]. Rise in measured Cu resistivity $\rho$ for decreasing interconnect cross-sectional area. This significant rise in $\rho$ threatens the performance of future interconnect generations. Similar metrology studies are essential to predicting future performance as devices approach material parameters deviate from bulk values. Each data point is the average of 4 area measurements from separate TEM cross-sections at arbitrary points along a wire. Three-dimensional analytical techniques described in this thesis provide an efficient method to sample LER variations from only one thick TEM cross-section.

formance and reliability. Therefore, complete device characterization requires accurate measurements of structural variations, whether they occur within or between devices.

Size-effect literature for Cu wire structures lacks consensus on the dominant phenomenon leading to the observed increase in apparent wire resistivity [40–51]. Two main methods exist to determine wire resistivity: direct measurement [41] of $R, A$ and $L$ to calculate $\rho$ and temperature dependent resistance measurements that allow extraction of wire $\rho$ from assumptions that the electron-phonon scattering contribution to

$\rho$ in the wire is the same as bulk and independent of size [43]. The direct measurement approach mainly suffers from difficulties in accurately measuring the wire's cross-sectional area, which is addressed in Chapter 2 of this thesis. Temperature-dependent resistance measurements avoid the need to measure physical dimensions, but must assume Matthiessen's rule holds for structures with dimensions near to the mean-free-path of electrons in the material [43]. For fine Cu lines (sub-100nm line width), the two methods differ in their estimation of $\rho$ for similar wire structures, indicating a flawed assumption in one or both of the methods [41, 47, 51]. Some reports in the literature suggest that grain-boundary scattering significantly impacts the overall resistivity of scaled wires [40, 47, 49]. Others attribute increases in wire resistivity to surface scattering [41, 46, 51], while some experiments show surface scattering decreases with wire width [44]. The LER has also been shown to impact fine line $\rho$ [45, 48]. The general lack of consensus is understandable because the main sources of size-effect induced resistivity exhibit similar dependencies on shrinking wire geometries. Acquiring results that converge on the same resistivity value for similar wires will heavily depend on statistically accurate measurements of wire cross-sectional areas, which Chapter 2 explores in detail.

## 1.4 Metrology Techniques for Measuring Critical Dimensions

The scanning electron microscope (SEM) rasters a focused beam of electrons accelerated to 10 – 30keV across a surface and is the most common technique for measuring the critical dimensions of IC structures. Incident electrons interact with atoms in the target material and generate low energy (< 50eV) secondary electrons that only escape the material if produced near the surface. Most materials exhibit similar secondary electron yields for a given incident beam energy, and therefore surface morphology produces

image contrast useful for measuring devices on the wafer surface. Another operating mode collects only incident electrons that are reflected back out of the specimen due to large-angle elastic scattering events. Back-scatter image contrast varies strongly with the atomic number of the target atoms at each raster position and is capable of material differentiation [52].

SEMs allow rapid, nondestructive imaging of surface structures with ~5nm resolution but are not capable of resolving sub-nanometer features affecting current/future devices. The incident electrons exhibit a large interaction volume due to elastic scattering events and generate detectable electrons near the surface nanometers away from the incident beam's entrance position. Therefore, SEM resolution does not generally benefit from a more focused incident electron beam. Also, SEM is a surface sensitive technique incapable of probing buried structures. Detailed analysis to determine failure modes requires higher resolution analytical techniques for continued device scaling.

A transmission electron microscope (TEM) uses a high-energy beam of electrons (>100keV) to produce atomic resolution images from material sections only 30 – 50nm thick and is indispensable to analyze the smallest device features. Incident high-energy electrons ideally undergo minimal scattering events before passing through the entire specimen and yield localized information about the target material. Time intensive sample preparation techniques [53, 54] necessary to produce such thin cross-sections are destructive and can no longer be considered thin compared to feature sizes of modern IC devices. Feature overlap in projection images of dense structures contained within a TEM cross-section complicates analysis, but a quantitative three-dimensional reconstruction of the original device structure provides unambiguous results. This thesis focuses on three-dimensional tomographic imaging of thick material cross-sections for efficient measurement of critical IC device dimensions with nanometer scale resolution.

The success of advanced IC structures will require such detailed analysis to solve the many size-effect and reliability issues currently facing the semiconductor industry.

### 1.4.1 Projection Images from a Transmission Electron Microscope

An electron microscope image is produced from electron scattering within the specimen, which gives rise to multiple contrast mechanisms depending on the type of illumination. Conventional TEM (CTEM) simultaneously illuminates an area of the specimen with a parallel electron beam, and a charge-coupled device (CCD) camera with high pixel density images the electrons transmitted through each point on the specimen. The wave-like nature of the partially coherent incident electrons yields diffraction effects and phase differences between electrons that pass through slightly different parts of the sample. Interference causes CTEM image intensities to vary abruptly across a specimen due to randomly oriented crystalline planes and slight thickness variations. Therefore, CTEM contrast in two-dimensional projections can be difficult to interpret especially for polycrystalline solid state materials [55].

A STEM rasters a beam of electrons focused to an Ångstrom sized spot across a specimen and uses post-specimen single-channel detectors to collect electrons scattered at each raster position within a given solid angle. The specific collection angles of a detector determine the dominant contrast mechanisms that form the resulting STEM image. Bright field (BF) STEM imaging uses a relatively small disc-like detector designed to collect the unscattered and low-order diffraction Bragg discs within 0 – 10mrad of the optical axis. BF-STEM is similar to CTEM by reciprocity [56–58] and produces image contrast dominated by diffraction and phase effects difficult to directly interpret for crystalline materials, because small changes in microscope defocus, specimen thickness

and specimen orientation produce abrupt changes in image contrast. Annular dark field (ADF) STEM, another common imaging technique, utilizes an annular detector to avoid the intense zero- and low-order Bragg reflections while only collecting highly-scattered electrons > 50mrad. The detector averages over many weak high-order Bragg diffraction discs as well as incoherently scattered electrons to suppress diffraction contrast and produce image intensities proportional to the atomic number $\left(\propto Z^{1.7}\right)$ and projected thickness of the material at each raster position [59]. ADF-STEM image intensities are directly interpretable, called *Z*-contrast imaging, allowing material differentiation in structures and is widely used in materials science for this purpose [60, 61].

## 1.5 Electron Tomography

Traditional TEM only produces two-dimensional projection images, but full understanding of some nanoscale structures requires three-dimensional analysis. Three-dimensional characterization and visualization of nano-sized electronic devices can be accomplished by electron tomography (ET) [2, 3, 62–67]. The technique recovers the lost information in the projection direction from a tilt-series of two-dimensional projection images acquired at many different viewing angles, assuming a monotonic relationship between image intensities and material thickness [68]. The superposition of many projection images yields an intrinsically higher signal-to-noise ratio (SNR) in reconstructions than the original projections, which improves measurement accuracy of device features defined by material interfaces. Among many other uses, the tomographic method is applied in medical computerized axial tomography (CAT) scans, which is accomplished by simultaneously rotating an x-ray source and detector around the patient to provide projections from many different viewing angles. Electron microscopes re-

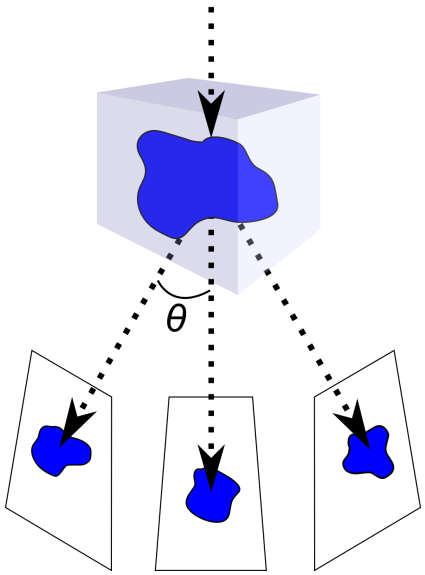


Figure 1.10: Diagram of the single-axis tilting scheme for electron tomography showing only three projections. Projections are recorded at regular tilt increments of $\theta$ as the object is rotated through a range of tilts around a single fixed axis. A typical tilt-series contains 140 projection images from $\pm 70^{\circ}$ separated by consistent $1^{\circ}$ increments.

quire a physically stable source and detector such that the object of interest is instead rotated with respect to the electron beam for the same effect.

The single-axis tilt scheme (see figure 1.10) is the most commonly used technique in ET, because it entails relatively simple methods for data acquisition and reconstruction. A specimen rotates around the fixed eucentric axis of the microscope's stage from one extreme tilting angle to the other, while projections are acquired at regular tilt increments. Ideally, a tilt-series contains projections from a complete $180^{\circ}$ rotation of the object to include information from all orientations, but typical TEM specimens (such as those discussed in this thesis) are prepared in a slab geometry for traditional single-axis high-tilt holders[1]. The maximum tilt range of traditional TEM stages is limited to ap-

[1]Notable manufacturers of high-tilt holders include Fischione Instruments, Inc. and Gatan, Inc.

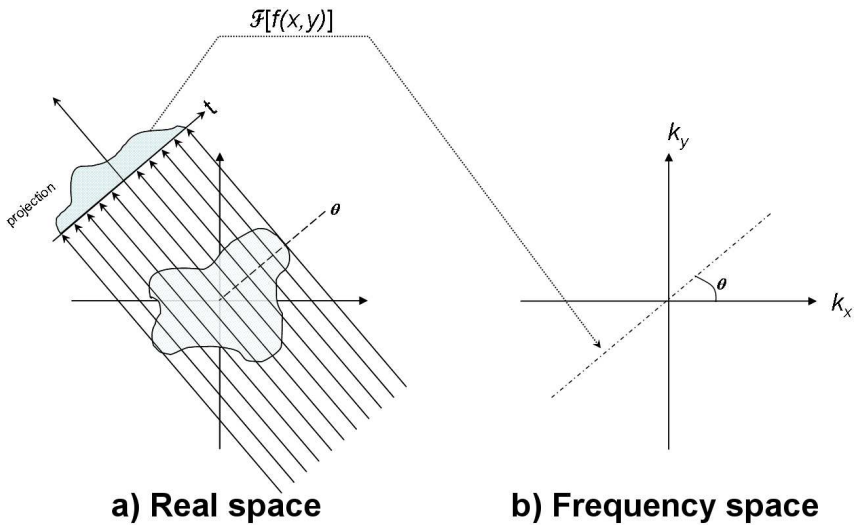


Figure 1.11: The Fourier slice theorem states that a projection of an object is equivalent to a sampling of the central plane of the object's full Fourier transform at the same angle. a) This schematic represents line-integrals (or projections) parallel to a given axis of the density of a two-dimensional object into one-dimension at an angle $\theta$. b) The Fourier transform of the projection, represented by the $\mathcal{F}$ symbol, is equivalent to a sampling of the object's full Fourier transform at the angle $\theta$. This diagram shows a simplification of the Fourier slice theorem as applied to a two-dimensional object, but it easily translates into three-dimensions.

proximately ±80° due to space limitations between electron lenses in the microscope's column. New dedicated tomography holders with a post design allow for full rotation of a needle-shaped specimen, which increases the final reconstruction resolution and eliminates artifacts [69]. Specimen preparation techniques that produce needle-shaped samples [54, 70] are not yet widely used by the electron microscopy community hindering adoption of full-rotation equipment. This thesis focuses on single-axis tilt series' of specimens prepared with the traditional slab geometry.

### 1.5.1 Fourier Space Reconstruction

The Fourier slice theorem (also known as the projection theorem) is the basic underlying principle of three-dimensional tomographic reconstruction regardless of the method used to acquire the projections. It states that a projection of an object at an angle $\theta$ is equivalent to sampling a central plane of the object's full three-dimensional Fourier transform at the same angle $\theta$. Figure 1.11 is a diagram of this mathematical theorem outlining the connection between a) the projection in real space and b) the corresponding plane sampled in Fourier (frequency) space. The Fourier transforms of a series of real-space projections acquired at many different angles can be used to fill in the object's three-dimensional Fourier transform, which is then inverted to produce a reconstruction of the original object in real space. The diagram in Figure 1.12 shows the theoretical discrete sampling of two-dimensional Fourier space along the $k_x$ and $k_z$ directions by single-axis rotation to acquire 11 projection images evenly spaced through a tilt range of $\pm 70^{\circ}$. Triangles in figure 1.12 highlight regions of Fourier space not sampled by this incomplete tilting scheme, which slightly distorts features along the projection direction (the z-axis) in the final reconstruction. Acquisition of projection images at the highest tilt angle possible minimizes the effect of this *missing wedge* of information. Herman [71] and Crowther [72] offer detailed treatments of the mathematics involved in Fourier reconstruction.

The Fourier transforms of all acquired projections properly combine to fill an object's Fourier space $F(k_x, k_y, k_z)$, and application of the three-dimensional inverse Fourier transform $\mathcal{F}^{-1}[F(k_x, k_y, k_z)]$ produces a real space approximation of the object's shape and density. This method, known as direct Fourier space reconstruction, offers a clear description of tomography's underlying principles but in practice presents difficult and computationally expensive complications. The inverse transform requires a continu-

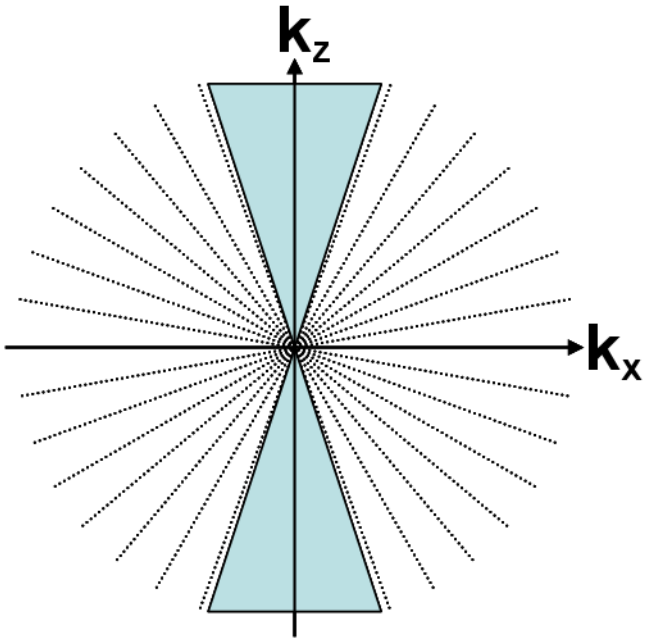


Figure 1.12: Diagram of the sampling of two-dimensional Fourier space by 14 projections from ±70° with tilt increments separated by 10°. The shaded, blue triangle highlights the missing wedge of information that is not sampled by a single-axis tilt scheme. This missing information leads to the elongation of features along the projection direction in the final reconstruction and effectively reduces the resolution by a factor < 1.3 for the indicated sampling parameters as calculated by equation (1.4).

ously varying function with a Cartesian based coordinate system, but tomographic data is acquired by discrete, radial sampling as seen in Figure 1.12. The radially sampled data requires interpolation to properly map into rectangular Cartesian space prior to Fourier inversion, and the specific interpolation method chosen greatly affects the quality of the final reconstruction [73].

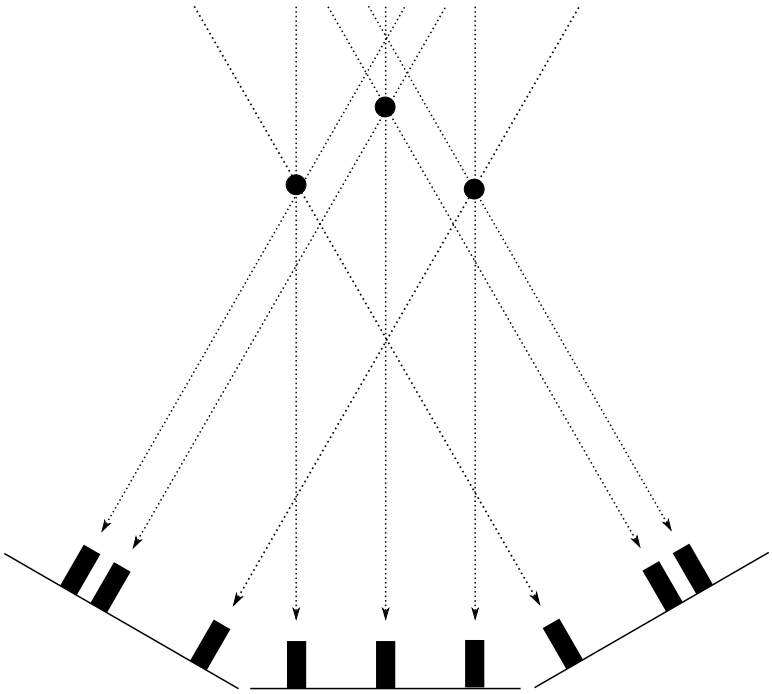

Figure 1.13: A diagram showing the projection of three dots arranged in a triangle shape. The relative arrangement of the three dots changes as perceived along different projection directions. Any one projection does not uniquely describe the actual arrangement of the dots.

### 1.5.2 The Radon Transform and Real Space Reconstruction

Modern tomographic reconstruction methods rely on the real-space Radon transform to avoid complications introduced by Fourier inversion [2, 71, 74, 75]. The Radon transform maps a three-dimensional object onto a two-dimensional plane by calculating line integrals (or projections) of the object's density through all "projection rays" parallel to a given axis. Incoherent electron scattering contrast in STEM and CTEM images is considered a line integral of the specimen's density [76, 77], and therefore the Radon function provides a mathematical framework that closely matches the tomographic method. A reconstruction from electron microscope projections reproduces the density distribu-

tion of the original object, which can be used to distinguish regions of distinct material phases in three-dimensions.

Figure 1.13 shows three one-dimensional projections of a triangular dot pattern at different angles that describe the overall shape as observed parallel to each axis, but no single projection gives a complete understanding of the actual distribution of the two-dimensional dots. To reproduce the original object, the lower-dimensional projections are extended back into the higher-dimensional space at the correct angles in a process called *back-projection* illustrated in Figure 1.14. This limited reconstruction does not faithfully reproduce the original triangle-dot formation, because it superimposes only three back-projections with a limited ±30° tilt range. Figure 1.14a) shows two extraneous dots (one above and one below) included with the original pattern from figure 1.13, which are reconstruction artifacts easily eliminated by superimposing a fourth back-projection at a higher angle as in Figure 1.14b). This exhibits the dangers of under sampling even a simple pattern and indicates that complex, extended structures require many projections from as large a tilt range as possible for an accurate reconstruction.

### 1.5.3 Filtered and Iterative Back-Projection

A fundamental connection exists between Radon space and Fourier space such that both theoretically offer equivalent methods for tomographic reconstruction [71], but the forward and reverse Radon transforms are performed completely in real space. Back-projection via the inverse Radon transform avoids the forward/inverse Fourier transforms, interpolation and filtering necessary for direct frequency space based reconstruction algorithms. Reconstructions, even by direct real-space inversion, typically yield blurred features with poorly defined fine spatial details, because as seen in figure 1.12,

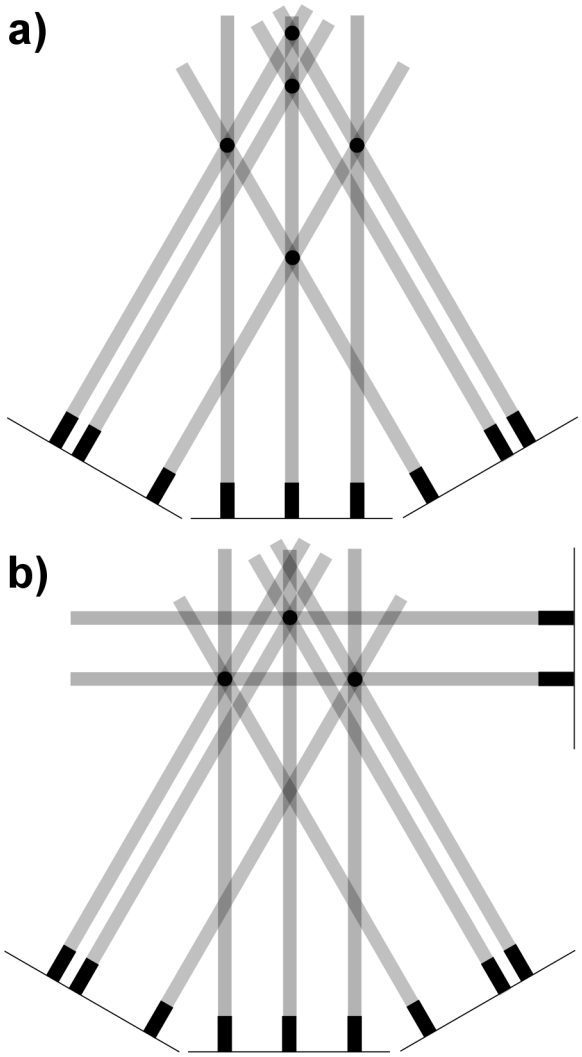


Figure 1.14: a) Direct back-projection of three Radon transforms at different angles to produce an approximation of the original distribution. Two extra dots appear due to the overlap of the back-projections, which are only reconstruction artifacts. Addition of a fourth projection at a higher angle faithfully reproduces the original three dot pattern. More complex, extended structures will require many more projections for a faithful reconstruction.

low-frequency information near the zero of the *k*-axes is oversampled as opposed to the under sampled high frequencies. The *weighted back-projection* technique convolves the reconstruction with a simple radial weighting filter that increases linearly from zero amplitude at zero frequency to a maximum at a higher cut-off frequency. The weighting filter evens out the uneven sampling distribution in Fourier space, [2, 75] and is applied after the real-space back-projection calculations are completed via the Radon transform. Weighted back-projection is currently the most widely used reconstruction technique due to its simplicity and efficiency, but more complex techniques are capable of refining the initial reconstruction to more closely match the original experimental projections.

Discrete, uneven sampling inherent in tomographic data acquisition introduces errors in the final reconstruction, but the original TEM images can be considered ideal projections of the object. The simultaneous iterative reconstruction technique (SIRT) for ET [78], outlined in figure 1.15, takes advantage of this to improve the accuracy of the final three-dimensional representation. First, an initial reconstruction is produced from the experimental projections by weighted back-projection. A series of simulated projections is generated from the initial reconstruction by application of the forward Radon transform at the same viewing angles used for the experiment. These ”re-projections” are compared to the original TEM images, considered ideal projections of the original structure, to minimize reconstruction errors introduced by discrete sampling. Back-projection of the new projections produce a second version of the reconstruction, and the process is iterated up to $\sim 30\times$ until the reconstruction produces re-projections closely matching the experiment. SIRT yields reconstructions with higher contrast compared to other non-iterative methods, but the attainable resolution - discussed in section 1.5.4 - is not well defined. Reconstructions presented in Chapters 2 and 4 of this thesis utilize SIRT for ET.

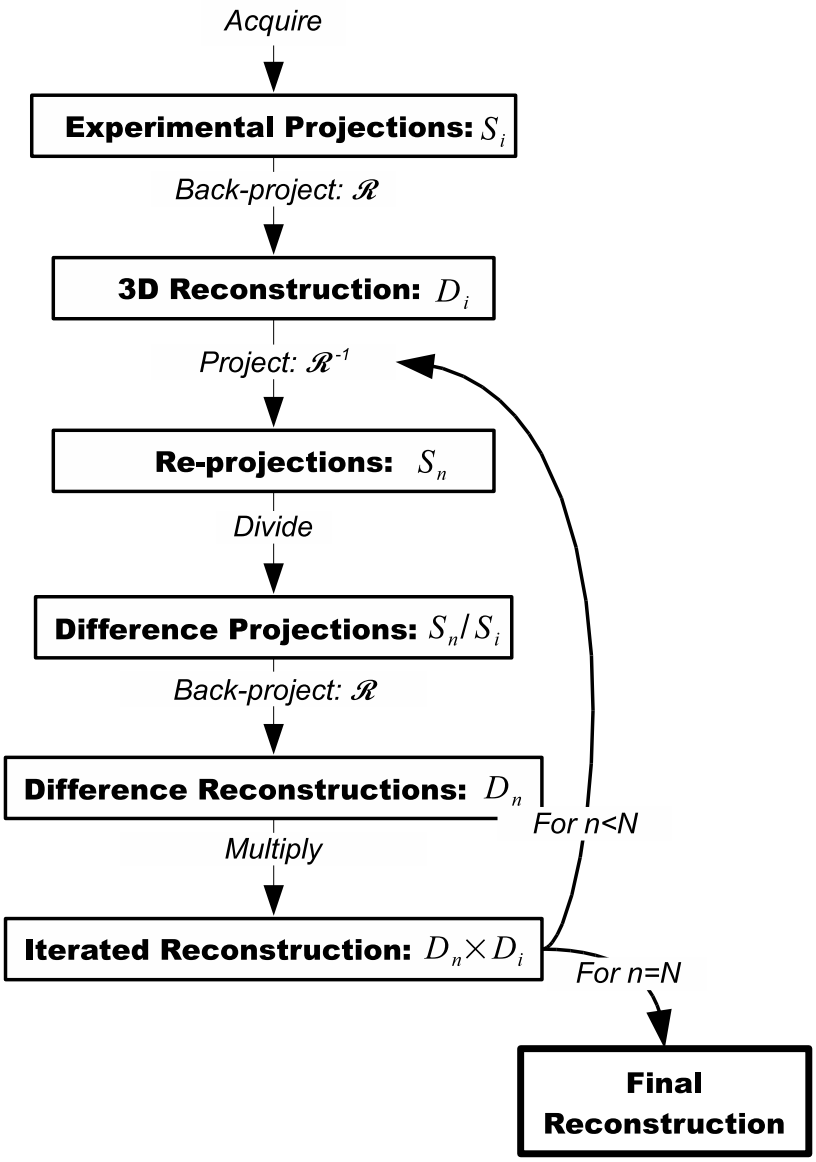


Figure 1.15: Flowchart of the simultaneous iterative reconstruction technique (SIRT) for three-dimensional electron tomography (ET). $\mathcal{R}$ and $\mathcal{R}^{-1}$ represent the Radon transform and its inverse respectively. Re-projections of a trial reconstruction are compared to the original experimental data as a reference to eliminate artifacts. Up to $N = 30$ iterations are typically used to produce to a final reconstruction.

### 1.5.4 Resolution of Electron Tomography Reconstructions

A non-iterative reconstruction from a single-axis tilt series exhibits anisotropic resolution, because the tomographic acquisition method inherently under samples the object's structure. Resolution along the tilt-axis (usually the x-axis) is equal to the original experimental resolution assuming a perfect tilt-series alignment as discussed in Appendix A. Resolution along the imaging axis perpendicular to the tilt axis (usually the y-axis) is estimated by the number of discrete projections $N$ equally spaced over ±90° used to reconstruct a volume of diameter $D$ as

$$d_y = \frac{\pi D}{N} \tag{1.3}$$

The missing wedge of information along the $k_z$ axis - unsampled due to a limited maximum tilt angle $\alpha < 90°$ - dominates resolution along the projection direction (always the z-axis in this thesis) [63]. Features in the reconstruction are stretched by an elongated factor $e_{yz}$ that affects the z-axis resolution as

$$d_z = d_y\, e_{yz} = d_y \sqrt{\frac{\alpha + \sin(\alpha)\cos(\alpha)}{\alpha - \sin(\alpha)\cos(\alpha)}} \tag{1.4}$$

Resolution along the projection direction should be maximized, because we specifically apply ET to recover this information. It is therefore essential to minimize $e_{yz}$ by maximizing the tilt range ($\alpha$) and the resolution of the original TEM projections ($d_y$). Rotation increments finer than 1°, however, do not achieve an appreciable increase in theoretical resolution but will probably lead to increased errors in tilt series alignment (see Appendix A) such that resolution is more likely diminished. The elongation factor is ≤1.3 for a maximum tilt angle exceeding 70° in both directions [69, 72].

The above treatments of tomographic resolution are based on simple theoretical filling of Fourier space by a discrete number of projections and a perfect tilt-series alignment. They are guidelines to the best achievable resolution for simple weighted back-

projection reconstructions but do not directly apply to SIRT reconstructions, which depend on parameters specific to each tilt-series such as noise and the object's shape. It is therefore impractical to define equations that describe the resolution of SIRT reconstructions beyond the precious estimations for weighted back-projections.

## 1.6 Monotonic TEM Image Intensities for Electron Tomography

For a proper three-dimensional reconstruction, ET requires image intensities that consistently provide a monotonic measurement of some property of the sampled volume in every tilted image, which is known as the *projection requirement*. The resulting reconstruction consists of voxel (the three-dimensional version of a pixel) intensities exhibiting the three-dimensional distribution of the measured parameter. As previously discussed in section 1.5.2, coherent or incoherent electron scattering within the material dominate intensities in each TEM image pixel [76, 77]. Coherent contrast mechanisms that dominate some traditional imaging techniques (see section 1.4.1) vary non-monotonically with small changes in sample thickness or rotation and produce projections inconsistent with the projection requirement. The applicability of each imaging technique to reconstruct a given structure depends on the dominant contrast due to the materials present in the sampled volume.

Images of amorphous materials that make up cellular structures are commonly acquired by CTEM's parallel illumination, and an objective aperture inserted after the specimen excludes some electrons from the image resulting in weak incoherent image contrast. Crystalline materials common in solid state devices produce strong diffraction contrast independent of the projected specimen density regardless of the presence of an objective aperture [55]. Figure 1.16a) shows a CTEM projection image of a thin

polycrystalline Cu layer in cross-section with uniform projected thickness, but diffraction effects from randomly oriented Cu grains produce intensity variations unrelated to mass-thickness. Therefore, CTEM fails the necessary projection requirement of ET for crystalline materials and is generally unsuited to three-dimensional investigations of IC devices.

The geometry and size of post-specimen electron detectors determine STEM image contrast (see section 1.4.1) [55, 60, 61]. As seen in Figure 1.16b), diffraction contrast dominates BF-STEM for crystalline materials similarly to CTEM and generally fails to provide monotonically varying image intensities even for small changes in specimen orientation. BF-STEM is suited to investigate amorphous material phases such as biological structures, but even very limited electron doses induce structural changes in these materials [79]. Radiation damage and signal-to-noise are the limiting factors that determine tomography acquisition parameters, which directly affects the attainable resolution of biological reconstructions [80–82]. CTEM is known to have a superior signal-to-noise ratio (SNR) for low dose conditions compared to STEM techniques [83], although careful control of the focused STEM beam allows the user to precisely limit irradiation of any given region [55]. Regardless, CTEM is much more common, and traditional BF-STEM is rarely utilized for ET experiments.

HAADF-STEM imaging is dominated by the density, atomic number ($Z$) and thickness of the target atoms at each raster position and generates incoherent image contrast that varies directly with specimen composition [55, 60, 84]. In Figure 1.16c), a polycrystalline Cu thin-film exhibits nearly constant intensity, because the large annular detector effectively eliminates diffraction contrast. $Z$-contrast dominates for thin cross-sections (<50nm thick) and differentiates materials by image intensity. Problems arise for HAADF-STEM in thick cross-sections of highly-scattering materials common in IC

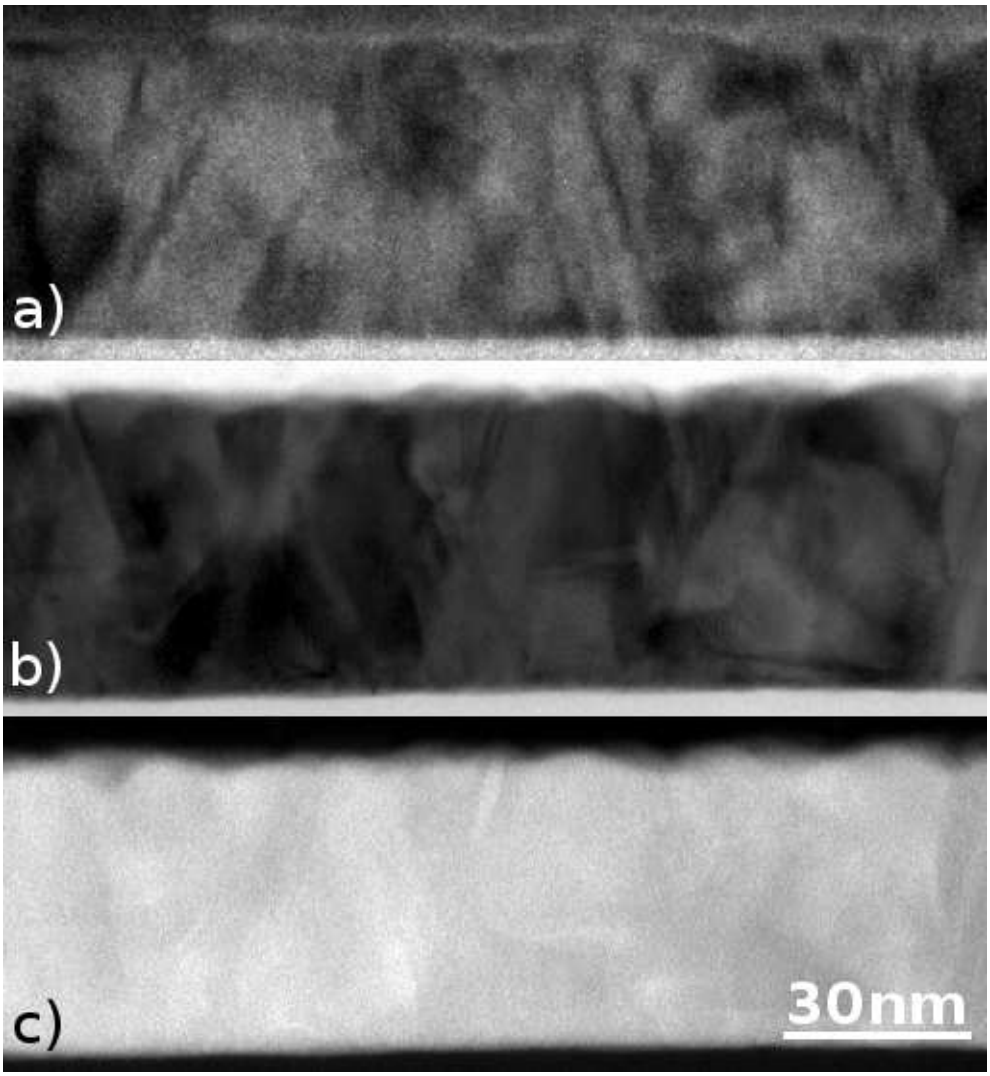


Figure 1.16: TEM images acquired with different imaging techniques of a Cu thin film in cross-section prepared such that all measured positions are of uniform thickness. a) The CTEM image shows intensity variations due to the randomly oriented Cu crystal grains. b) BF-STEM image exhibiting coherent scattering contrast very similar to the CTEM image. This imaging technique is also not suited for three-dimensional reconstructions of crystalline materials. c) HAADF-STEM image showing relatively constant intensity across the entire Cu thin film. *Z*-contrast imaging is dominated by material phase and thickness such that it provides a proper projection for electron tomography.

devices, because the detector's outer collection angle is limited due to space limitations inside the TEM column. Thick, highly-scattering materials scatter a majority of electrons beyond the range of the detector leading to a non-monotonic intensity/thickness relationship. Chapter 3 investigates this issue in depth with emphasis on reconstructing ultra-thick material cross-sections and details the novel incoherent BF-STEM technique that produces image intensities complementary to HAADF-STEM without artifacts.

## 1.7 Overview

Chapter 2 shows that cross-sectional area measurements of scaled Cu interconnects from STEM projection images are biased to low values due to the overlap of small, dense features along the projection direction. Analysis of the same wire section by three-dimensional ET provides many measurements of Cu cross-sectional area for a statistically relevant sampling of the LER contained within the sample's thickness. The wire resistivity calculated from a single measurement of a two-dimensional projection is 5% lower than the average of many measurements from a three-dimensional reconstruction. ET gives an accurate representation of the device structure for efficient sampling of interface roughness along a wire section with nanometer resolution. A cross-section thickness <50nm is equal to half the spatial frequency of LER variations along the length of this specific wire, and minimizes the effect of roughness on measurements from projection images. LER will represent a larger percentage of interconnect width in future devices, which necessitates thinner samples for area measurements from projection images to converge with the tomographic average. 50nm sample thickness is near the limitation of site specific sample preparation methods such as FIB, and three-dimensional analysis of smaller wires may be necessary to accurately predict their performance [4].

We develop the novel IBF-STEM imaging technique in chapter 3 to image, without artifacts, thick cross-sections containing highly-scattering materials. We wrote a Monte-Carlo electron single-scattering code to simulate the transmitted electron intensities collected with HAADF and IBF detectors by quantitatively modeling interactions between high-energy electrons and solids of varying thickness. HAADF-STEM exhibits contrast reversal in materials with large elastic scattering cross-sections, which produces non-monotonic image intensities unsuited for ET. IBF-STEM is a complementary imaging technique that produces monotonic image intensities for all material thicknesses [5]. Also, simulations of expected HAADF SNRs predict low-noise, high-contrast images for relatively thin specimens, but IBF-STEM provides superior image quality for ultra-thick cross-sections. We define a material thickness ($t_{1/2}$ for any material that determines the cutoff between thin sections preferably imaged by HAADF and ultra-thick sections preferably imaged by IBF. This parameter varies directly with the Rutherford elastic mean-free-path, and we develop a general relationship that determines the STEM imaging technique suitable for any material of any thickness.

In chapter 4, we investigate a via-to-wire interconnect structure containing a stress-void that possibly undercuts the via connect, but simple projection images are incapable of showing the actual void geometry or location. The 250nm wide Cu structure produces contrast reversal in HAADF-STEM images at high tilt values for ET, and the resulting reconstruction contains void artifacts that lower confidence in measurements of the actual void. We therefore apply IBF-STEM faithfully reconstruct the structure without image artifacts and directly measure the void's geometry, location and volume [5].

CHAPTER 2

# THREE DIMENSIONAL MEASUREMENT OF IC INTERCONNECTS USING ELECTRON TOMOGRAPHY

Defect analysis in integrated circuit (IC) nanostructures is of major concern for circuit reliability and large scale device integration for manufacturing. Various microscopy methods have been used to verify the properties of fabricated structures, but only transmission electron microscopy (TEM) provides the resolution needed to describe the 5 – 50nm features in modern devices. No structure is perfect at the nano-scale, and circuits are built with tolerances to account for variations introduced during materials processing steps such as lithography, etching and deposition. These variations are no longer negligible compared to device dimensions and must be considered in order to predict device performance and reliability. Complete device characterization requires accurate measurements of these variations, whether they occur within or between devices. TEM by itself is not viable for such characterization in certain microelectronics systems because the overlap of small, dense features in projection complicates image analysis. This chapter details confusing and sometimes inaccurate results obtained due to feature overlap along the projection direction in TEM images. Three-dimensional reconstruction of IC devices by electron tomography (ET) with a scanning transmission electron microscope (STEM) is used to compare the results of projection images and the full reconstructed structure.

## 2.1 Measurements to Calculate the Resistivity of Copper Interconnects

Cu interconnects can benefit from three-dimensional analysis to measure the cross-sectional areas of the Cu conductor and TaN/Ta liner at many points along a single wire. As detailed in section 1.2.1, Cu is currently used as the wire conductor in "back-end-of-line" (BEOL) structures due to its low resistivity and high resistance to electro-/stress-migration with respect to other possible interconnect materials. Still, the Cu must be lined with a TaN/Ta barrier layer to prevent migration of Cu into the semiconductor and to provide adhesion to the interlayer dielectric (ILD) surface. The performance of the wire as a conductor of electricity is affected by electron scattering from impurities/defects, grain boundaries and rough material interfaces at the wire's surface. A wire's average resistivity $\rho$ is an intrinsic property of its conducting structure that determines the resistance $R$ of a known length $L$ and cross-section $A$ by equation (1.2). Materials processing steps introduce local deviations from the desired smooth walls, known as line edge roughness (LER), with a negative impact on wire resistivity due to increased nonspecular electron scatter at the Cu/barrier interface [48].

Scanning/transmission electron microscopes (S/TEM) are currently used (either in the conventional or scanning mode) to directly measure semiconductor device features within 20 – 100nm thick sections at sub-nanometer resolutions, but by design conventional TEM and STEM only provide a projection of the imaged structure. In previous generations of devices, variations along the projection direction were considered insignificant compared to the device's lateral dimensions of interest and were typically ignored during device characterization. Modern chips contain smaller, denser structures, so significant variations in the projection direction make measurements from simple

projections potentially unreliable. Previously ignored structural defects now comprise a non-trivial percentage of some critical dimension measurements, which can produce significant variations in a device's performance. As such, traditional transmission microscopies may not be sufficient to fully characterize nanostructures, and three-dimensional imaging techniques are necessary.

### 2.1.1 The Electron Tomography Technique

Three-dimensional characterization and visualization of nano-sized electronic devices can be accomplished by ET. The technique recovers the lost information in the projection direction from a tilt-series of two-dimensional projection images acquired at many different viewing angles, assuming a monotonic relationship between image intensities and material thickness [68]. The three-dimensional nature of a reconstruction with an intrinsically higher signal-to-noise ratio (SNR) due to the superposition of many projection images improves measurement accuracy of device features that require differentiation between two different materials. This chapter reports on conductor cross-sectional area measurements used to calculate the average resistivity of ~90nm wide Cu wires lined with TaN/Ta barrier layers. The measurements are acquired by both two- and three-dimensional transmission electron imaging techniques to determine the effect of structural variations along the transmission direction contained within a cross-sectional sample's volume [4].

## 2.2 Materials and Methods

### 2.2.1 Electron Tomography of Nanowires

ET is widely practiced in the biological sciences to reconstruct cell structures using conventional transmission electron microscopy (CTEM) but has only recently been applied to amorphous inorganic materials [67]. Applying ET to crystalline materials requires a different imaging technique, because CTEM is a coherent imaging mode dominated by phase and diffraction contrast, which vary non-monotonically according to the target's internal crystallographic orientation with respect to the incident electron beam [2, 85]. High-angle annular dark field (HAADF) STEM, an alternative and incoherent imaging method, employs an annular detector to collect only highly scattered electrons from a focused, rastered beam of electrons. Pixel intensities in a STEM image are given by integrating the transmitted electrons scattered within a given solid angle as the Ångstrom sized beam rasters across the sample. Crystalline materials can diffract the incoming electrons, but a HAADF detector averages over many weak Bragg reflections to produce incoherent image intensities largely dependent on the target's atomic number ($Z$) rather than diffraction conditions within the sample [59]. High mass-thickness materials appear brighter in images due to high-angle elastic scattering of electrons, and images contain little background noise in thin ($<$ 100nm) samples. Bright field (BF) STEM employs a small circular detector to collect forward scattered electrons and produces coherent image contrast similar to CTEM, as expected by reciprocity [86].

Two TaN/Ta lined Damascene Cu wire arrangements are included in the study: a single isolated wire approximately 90nm wide and a nested structure with 9 parallel, closely packed wires approximately 80nm wide separated by 80nm of ILD. The Cu wires were fabricated using the dual-Damascene method by first etching trenches in

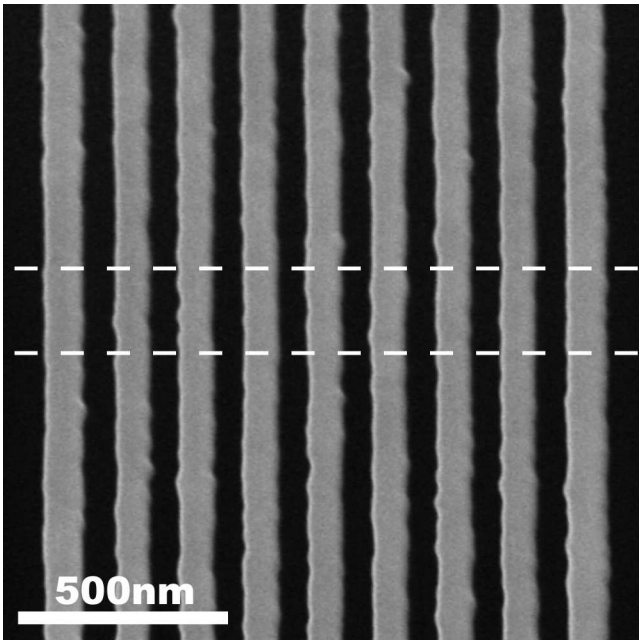


Figure 2.1: A high angle annular dark field (HAADF) STEM image showing the line-edge roughness (LER) of the copper wires from above. The white dashed lines indicate a 200nm FIB cross-section thickness. The amount of LER contained within a FIB cross-section is readily apparent.

SiCOH, a low-dielectric-constant ILD, using photo-lithography and reactive ion etching techniques [7]. Next, the trenches were filled with physical vapor deposition (PVD) TaN/Ta diffusion barriers, a PVD Cu seed, and electroplated Cu. The excess Cu overburden was then removed by chemical-mechanical polishing. Figure 2.1 shows a two-dimensional projection image of the nested wire structure as viewed from above with an FEI Tecnai F20 200keV electron microscope operated in HAADF-STEM mode. The wires exhibit prominent LER with defect spatial frequency of ~100nm along the wire's length and a ±5nm deviation perpendicular to the length. A resistance of 2,815Ω was calculated from 14 current-voltage measurements across 1mm of the center, nested wire. Resistivity is normally calculated from the wire's cross-sectional area as measured by two-dimensional transmission imaging techniques that effectively integrate the structure

along the wire's length where LER blurs the interface between the overlapping barrier and conductor.

The HAADF-STEM imaging mode is employed in an FEI Tecnai F20 electron microscope to three-dimensionally reconstruct a 250nm thick *in-situ* FIB cross-section of the nested wire structure. The ET tilt series was acquired with the optic axis along the wire length at 0° tilt, and the structure was tilted around an axis perpendicular to the spacing between the wires. 71 projection images were acquired at 2° increments from $-73°$ to 67° (inclusive), which were aligned by automatic cross-correlation and manual shifting techniques using IDL 6.1. The three-dimensional reconstruction was produced using the multiplicative SIRT algorithm described in section 1.5.3 with 45 iterations implemented in IDL 6.1 [78, 87]. This represents a significant effort during acquisition and post-processing, but the reconstruction contains quantitative, nanoscale information about the wires' internal structure over their entire length. As calculated using equations (1.3) and (1.4), the reconstruction exhibits 2nm resolution along the axis perpendicular to the spacing between the wires (the y-axis) and 4.4nm resolution along the wires' length (the z-axis). The anisotropic resolution is due to sub-pixel misalignments of the original tilt series, the missing wedge phenomenon and discrete sampling of the structure with a finite number of tilt angles [2, 69].

The Cu cross-sectional area from projection images and tomography slices was defined using segmentation tools in the Amira 3.1 software package from Mercury Computer Systems. The border of the Cu conductor was traced by hand in each case using the segmentation lasso tool with the auto trace and trace edges options enabled, allowing the computer to aid in edge finding. Error in measuring the cross-sectional area is estimated to be $< 2\%$ by repeating a wire area measurement 10 times.

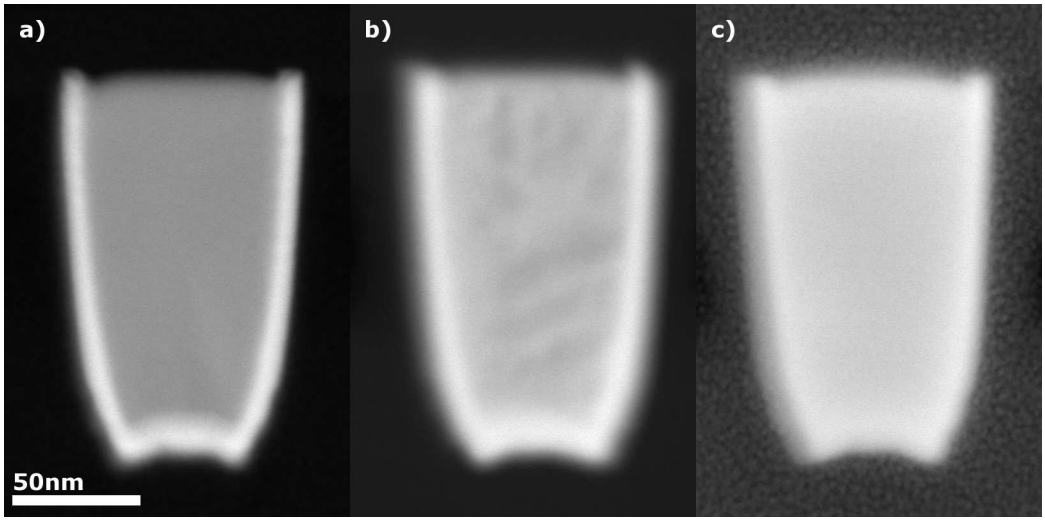


Figure 2.2: Three HAADF-STEM images of a) 280, b) 350 and c) 470nm thick cross-sections of copper wires with TaN/Ta barrier layers. The copper cross-sectional area is more difficult to distinguish from the TaN/Ta in thicker specimens partially due to the overlap of LER in projection.

A focused ion beam (FIB) was used to prepare one *in-situ* and five *ex-situ* wire cross-sections of varying thicknesses (0.28 – 0.47$\mu$m thick). Two *ex-situ* specimens were further manually thinned in the FIB to ~0.1$\mu$m. The region between the dashed lines in Figure 2.1 represents the portion of the wire contained within a 0.2$\mu$m thick FIB cross-section. LER should not be ignored for Cu area measurements from projections along a wire's length because significant variations are present within the volume of each FIB sample.

### 2.2.2 TEM Projection Imaging

Figure 2.2 shows three HAADF-STEM images of 280, 350 and 450nm thick FIB cross-sections, which indicate the difficulty involved in discerning the conductor/barrier interface as projected thickness increases. Preparation of thinner specimens minimizes

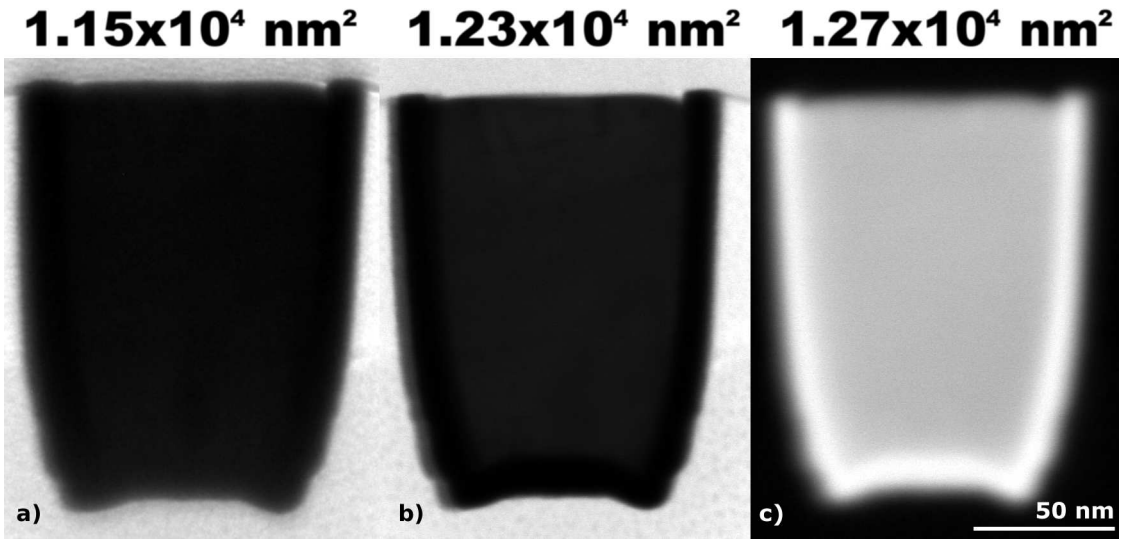


Figure 2.3: Transmission electron microscope images of the same 350nm thick isolated copper line cross-section comparing three transmission imaging techniques: a) conventional, b) bright field scanning and c) high angle annular dark field scanning. The resulting measured copper cross-sectional area is included above each image. The scanning techniques tend to yield better image contrast for the thick cross-section compared to the conventional technique.

inclusion of LER defects within the sample's volume but gives a local measurement that is not representative of the wire's actual average cross-sectional area. Therefore, many thin FIB sections are necessary to properly average measurements; a tedious and time consuming endeavor.

Different projection imaging techniques produce varied results for investigating moderately thick specimens. Figure 2.3 shows a) CTEM, b) BF-STEM and c) HAADF-STEM images of the same 350nm thick FIB wire cross-section, allowing a comparison of the diverse results obtained from different transmission imaging methods. Each image includes its measured cross-sectional area - these differ by as much as 10% -

indicating that image contrast mechanisms affect measurement results [88]. CTEM is not the optimal imaging method for very thick specimens, because it exhibits a much weaker dependence on material atomic number $Z$ than HAADF-STEM imaging. Also, the resolution of CTEM images suffers from additional chromatic aberration introduced by post-specimen imaging lenses, which are not used during HAADF-STEM imaging. Noise, low contrast and pixelation introduce subjectivity into cross-sectional area measurements, but 10 repeated measurements from the same image produce a maximum 2% area difference, which is in addition to the larger variability measured between imaging methods. CTEM images of FIB sections $\geq 0.35\mu$m thick lack sufficient contrast to discern the Cu/Ta interface, but STEM imaging techniques allow differentiation between these highly scattering materials. For low electron dose conditions typically used in biological investigations, CTEM is known to have a superior signal-to-noise ratio (SNR) in cases where radiation damage is the most important imaging factor [83]. The wires measured in this study, however, consist of robust materials that quickly conduct excess charge and heat from the irradiated area and are generally resistant to knock-on damage processes for the 200keV beam voltage used [89]. We therefore use large electron doses to attain acceptable SNR, and in figure 2.3 STEM is found to produce higher contrast for thick, dense materials contained in semiconductor electronic devices.

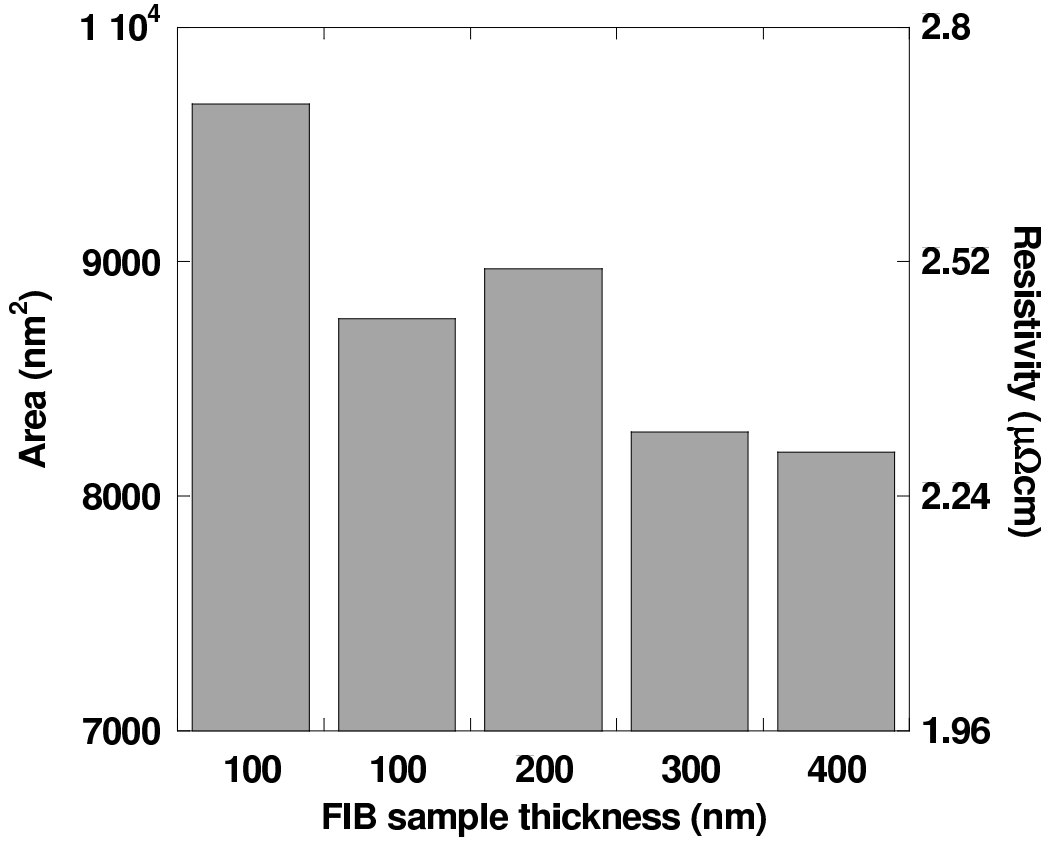


Figure 2.4: Copper cross-sectional areas and the resulting calculated resistivities of five FIB samples of varying thicknesses from the same nested wire using a STEM. The LER contained within the sampled volume causes large variations in measurements from fluctuations in roughness. There is also a systematic trend to a smaller apparent cross-sectional area due to the overlap of highly scattering barrier features in projection.

## 2.3 Results

### 2.3.1 Effects of Roughness on Measurements from Projection Images

The center nested wire's Cu cross-sectional area was measured in all five *ex-situ* FIB cross-sections utilizing the HAADF-STEM imaging technique. The cross-sections were of varied thicknesses from ~100nm – 470nm as measured in the FIB while viewing the finished sample along the cutting direction (on-edge). Figure 2.4 shows the measured conductor areas showing measurement variability due to the LER present within each cross-section's volume. A single projection image of a defect-prone structure leads to poor estimations of overall critical structural dimensions because the specific (yet arbitrarily chosen) portion of the wire contained within the sample volume may not be representative of the mean conductor cross-sectional area. As mentioned previously, size variations increasingly contribute to device performance degradation, and this trend will worsen as devices are further scaled. Defect analysis and accurate measurements of current/future nano-scale device parameters to predict performance require quantitative three-dimensional imaging techniques for full device characterization.

### 2.3.2 Three-Dimensional Analysis

The ET method is generally considered very time consuming, but in this case is efficient when compared to preparing and measuring 121 properly thinned FIB cross-sections [90] (disregarding the issue of feature overlap in projection) required to obtain a statistically similar average measurement. Figure 2.5 shows the reconstructed three-

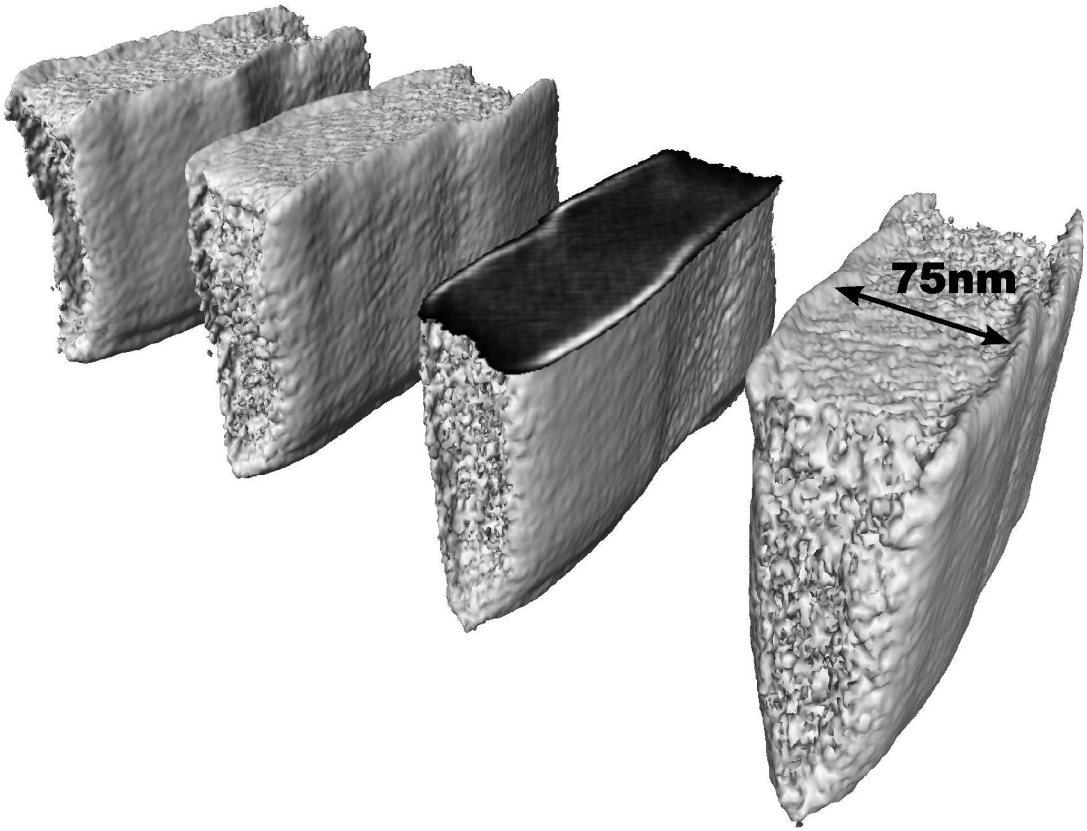


Figure 2.5: Three dimensional reconstruction of four wires lined with TaN/Ta and filled with Cu to make 75nm wide Damascene interconnects. The structures were reconstructed from 71 STEM projections at 2° tilt increments from −73° to 67° by ET. A cutaway of the top of the third wire reveals the LER contained within the sampled volume. Typical STEM projections do not show the roughness of the Cu/Ta interface which obscures wire cross-sectional area measurements, but the roughness is apparent in the three-dimensional reconstruction.

dimensional surface of four nested wires (of the total nine) with a cutaway to expose the LER contained within the sampled volume. ET allows visualization and quantitative analysis of the object's entire internal structure in all three dimensions, and the reconstructed volume was analyzed manually with segmentation tools in the Amira 3.1 software package as described earlier. Figure 2.6 shows three orthogonal cross-sections through the original reconstruction exhibiting the quality of the data and the detailed information available along all three dimensions. Figure 2.7 shows a histogram of the cross-sectional areas measured from each ET slice. The measured areas produce a mean and standard error of $(9.5 \pm 0.05) \times 10^3 \text{nm}^2$ indicating the degree of variance LER introduces within the FIB cross-section. The area measurements have a standard deviation of $0.5 \times 10^3 \text{nm}^2$. A separate two-dimensional HAADF-STEM projection image of the same wire used in the reconstruction yields an area measurement of $9.0 \times 10^3 \text{nm}^2$ which is a 5% difference from the tomographic measurements' average. The maximum error in manual cross-sectional area measurements utilizing the tools offered by the Amira software package was earlier determined to be <2%, which does not account for the discrepancies reported here.

Overlap of the wrinkled wire surface along the projected length of the wire consistently produced conductor cross-sectional area measurements lower than the tomographic average in projection images of wire cross-sections from other locations, which linearly impacts the resistivity calculated for this wire. Using the wire resistance measurement quoted earlier of $R = 2{,}815\Omega$, wire resistivity ($\rho$) is calculated by equation (1.2) using $L = 1\text{mm}$ and the tomographic average cross-sectional area to give $\rho = 2.7 \pm 0.01 \mu\Omega\text{cm}$. The same procedure was used to calculate the resistivities reported in figures 2.4 and 2.7. Also, an area measurement of the previously mentioned projection image of the same wire used for tomography measurements ($9.0 \times 10^3 \text{nm}^2$) yields $\rho = 2.5 \mu\Omega\text{cm}$, 7% lower than the tomographic average.

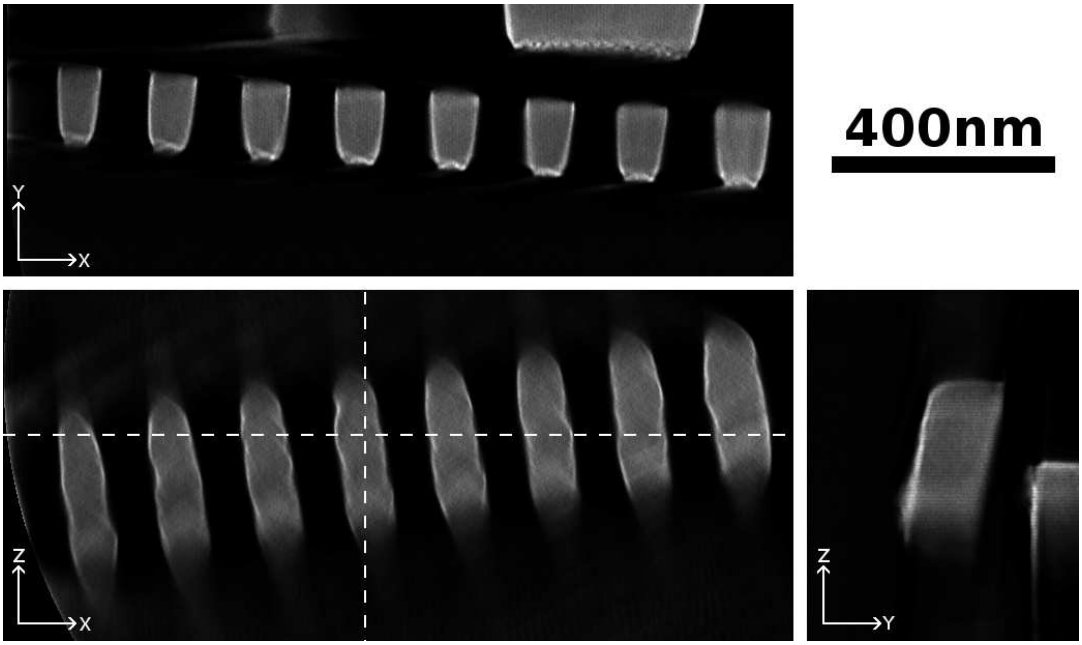


Figure 2.6: Three cross-sections through the original tomographic reconstruction showing the Cu (gray) lined with a TaN/Ta barrier (white). The lower left panel shows the detailed information only available in a three-dimensional reconstruction along the length and width of 8 separate wires. The *Z*-direction is the projection direction of the original tilt series along the STEM optical axis. White dotted lines indicate the locations of the slices shown in the other two panels. The top panel shows the wires' in cross-section as they are normally viewed for conductor area measurements. The tomography tilt axis, around which the structure was rotated to acquire a tilt series, is parallel to the *Y*-direction and passes through the center of the wire structure. The lower right panel shows a section through one wire along its length (*Z*-direction) and height (*Y*-direction). Elongation of the wire structures due to the missing wedge effect is seen along the *Z*-direction, but does not considerably affect cross-sectional area measurements.

## 2.4 Discussion

### 2.4.1 Minimum Thickness for Projection Measurements

Is it possible to avoid the discrepancy between the projected Cu cross-sectional area and the estimate provided by ET? Measurements by two-dimensional projections are biased to low values due to the overlap of the Cu conductor and its highly scattering TaN/Ta barrier layer along the wire's length. Preparation of thinner FIB specimens should allow for more accurate area measurements by excluding variations from the projected volume, but this also necessitates sampling from many points along the wire for a statistically meaningful average. Still, it is important to determine the FIB sample thickness at which projection errors are minimized in two-dimensional projections such that ET and projection analysis converge to equivalent area measurements. To determine this, different thicknesses of the reconstructed three-dimensional data are summed (re-projected) along the wire's length to produce simulated projection images. A similar method is employed in iterative tomographic reconstruction algorithms that modify a trial reconstruction according to comparisons between its simulated projections and the original STEM images until the two are consistent [78]. The simulated projection's conductor cross-sectional area is compared to the tomographic average of the same volume used to produce the simulated projection. The re-projection is accomplished by integrating pixel intensities in each reconstructed slice along the desired wire length, and the tomographic average is simply the average of the cross sectional area from each slice within a given volume. As a test, the entire reconstructed wire was re-projected along its length and compared to a normal HAADF-STEM projection. The resulting cross-sectional area from the simulated projection is $8.8 \times 10^3 \text{nm}^2$, which is 2% lower than the $9.0 \times 10^3 \text{nm}^2$ area measured from the two-dimensional HAADF-STEM projection

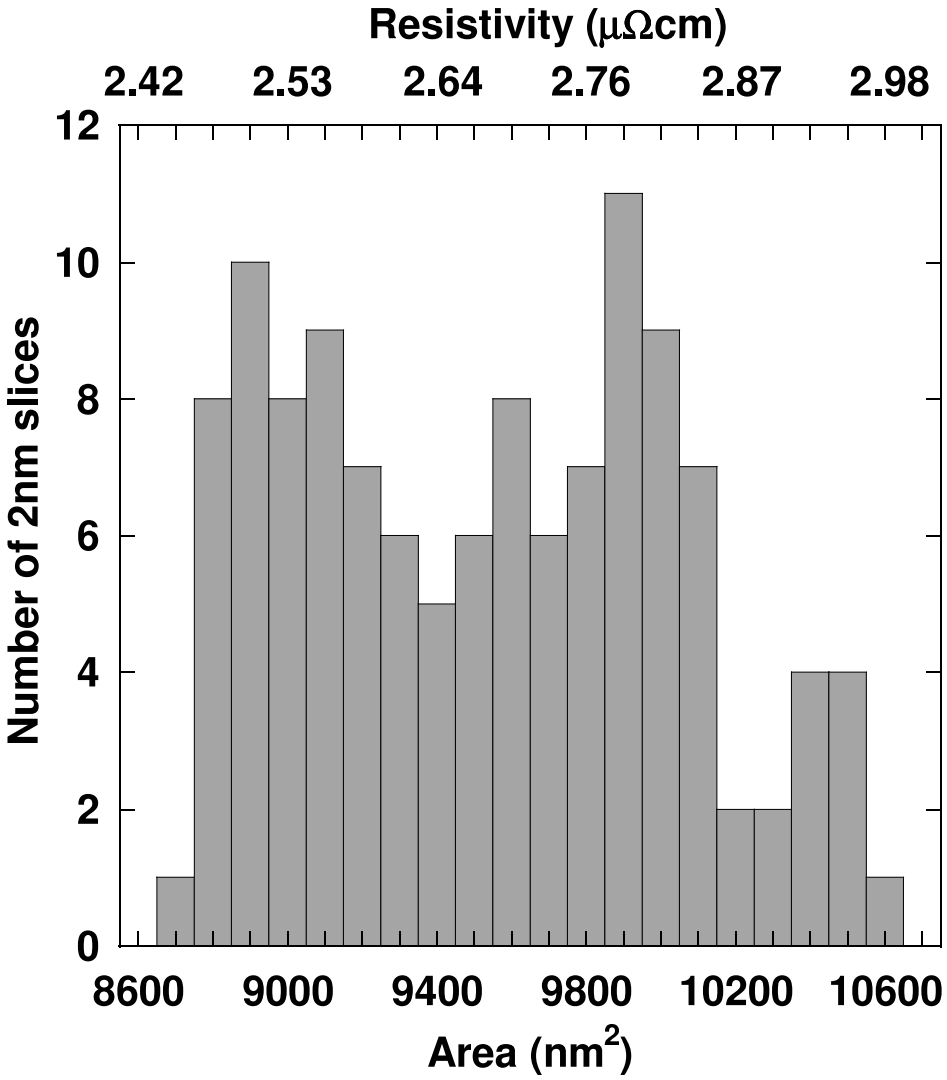


Figure 2.7: A histogram of the measured area from each tomography slice and its calculated resistivity ($\rho$) assuming a constant wire length. The measurements vary by up to 15% showing the variability introduced by LER.

image of the same structure. This difference is within the expected 2% error for cross-sectional area measurement subjectivity quoted earlier in this paper. The similarity of these two measurements demonstrates the accuracy of the ET technique and the validity of the re-projection method.

Application of the re-projection technique was then used to generate figure 2.8 and determine that statistically significant disagreement occurs between projections and the tomographic average when sample thickness exceeds 50nm, a thickness attainable by manual ion beam thinning in modern FIBs. This thickness corresponds to half of the wire's 100nm defect spatial frequency, such that cross-sections greater than 50nm thick contain significant LER defects. Overlap of these defects in two-dimensional projections bias copper area measurements to lower values with a linear impact on the calculated wire resistivity. For thicknesses below 50nm, the accuracy of cross-sectional area measurements is limited by error in area measurements. The minimum necessary TEM specimen thickness to avoid projection errors is highly dependent on the wire's LER parameters, such as the defect spatial frequency, and thus only provides an estimated ideal cross-section thickness for the wire studied here. In general, for purely two-dimensional projection STEM investigations, specimens should be sufficiently thin to avoid including structural variability within its volume. LER is predicted to scale with wire widths of future technology nodes, driving the ideal cross-section thickness to shrink below efficient specimen preparation capabilities. Thus thick-sample three-dimensional analysis techniques will be increasingly necessary. ET is capable of producing a three-dimensional model from one relatively thick FIB sample, which would allow measurement of a structure at many points for good statistical averaging.

## 2.5 Conclusions

ET was successfully implemented to measure the Cu conductor cross-sectional area in a wire with significant LER. We used the three-dimensional reconstruction of wires and liners to calculate the wire's average resistivity. Traditional STEM projection measurements are found to overestimate the resistivity as a consequence of underestimating the

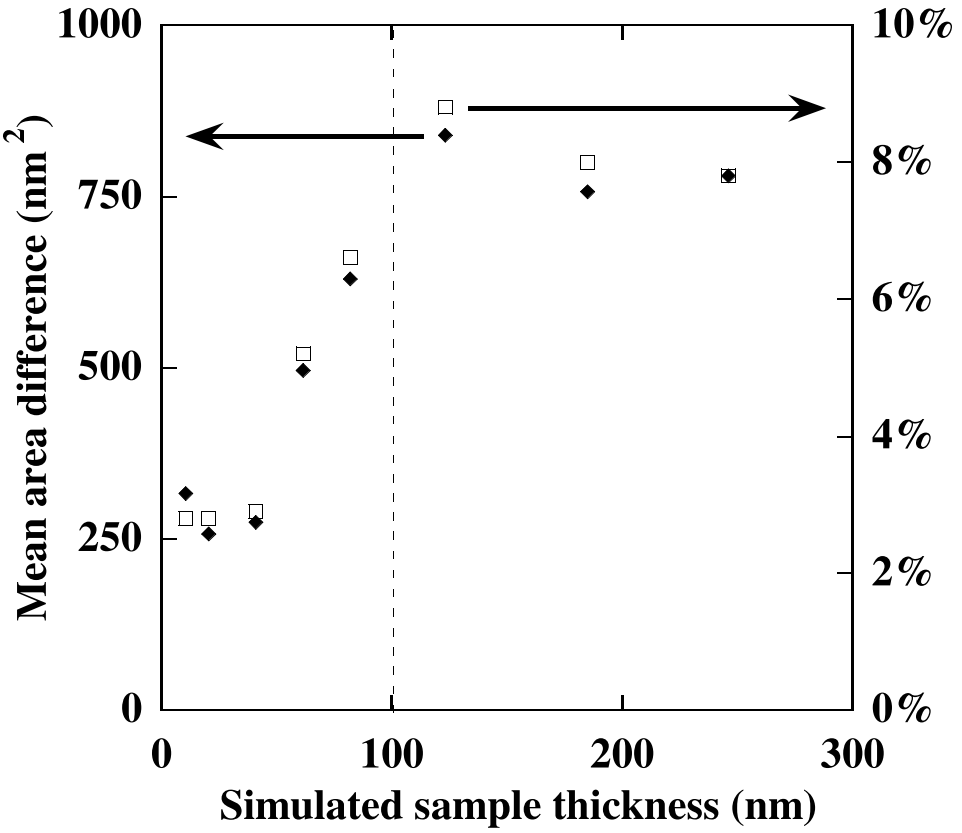


Figure 2.8: Various thicknesses of the tomographic reconstruction of the same wire used for figure 2.7 were re-projected (integrated) along the wire's length to simulate traditional projection images. The plot compares the Cu cross-sectional area measured in each reprojection to the average area of all of the reprojected tomographic slices. The maximum allowable FIB sample thickness such that LER does not greatly affect measurements is ~50nm for these 75nm wide lines. LER is projected to vary inversely with Cu wire width making this requirement an upper bound for cross-sectional measurements of future scaled wire structures.

cross-section when LER defects overlap along the wire's length in projection. These problems are overcome by ET, which produces a three-dimensional reconstruction of a structure with nanometer resolution. The time involved in data acquisition, alignment and other post-processing of ET data can be significant (see appendix A), but it provides efficient and accurate measurement of critical device dimensions while avoiding misinterpretation due to feature overlap common in traditional two-dimensional projection images. In this study, the overlap of LER defects in two-dimensional projection measurements leads to a 5% discrepancy between tomography and projection measurements, representing a significant measurement error for a critical device parameter: wire resistivity. The effect is minimized in this specific case for cross-sectional sample thicknesses <50nm, which corresponds to half the LER defect spatial frequency along the wire's length. Structural variation will become more pronounced due to scaling of micro-electronics and will necessitate the use of three-dimensional characterization for full, accurate structural analysis.

CHAPTER 3

# DEVELOPMENT OF NOVEL INCOHERENT BRIGHT FIELD STEM IMAGING TECHNIQUE

An essential condition for tomographic reconstructions is that the signal must be monotonic with thickness to avoid artifacts such as heavy particles appearing as voids. Conventional phase-contrast transmission electron microscopy (CTEM) is unsuited to electron tomography (ET) in crystal-containing specimens, because it produces non-monotonic image intensities dependent on diffraction and phase conditions within the sample rather than providing a signal related to the projected material thickness [2, 85]. CTEM is a coherent imaging mode where the image contrast changes from white to black to white again periodically with crystal thickness or tilt from a zone-axis. Instead, annular dark field (ADF) detectors collect only highly-scattered electrons within a large solid angle, averaging over many Bragg reflections, and thereby suppress phase and minimize diffraction contrast [59, 61]. As a result, incoherent imaging via ADF techniques in a scanning transmission electron microscope (STEM) have been used to reconstruct thin (<100nm) specimens [2, 65]. Even so, we find that problems arise when the object is comprised of very thick and/or high atomic number ($Z$) materials that produce increased backscatter and significant multiple scattering events to high angles. The projections undergo contrast reversals with increasing thickness. Hence, discerning whether apparent voids are due to genuinely missing material or are simply image artifacts is difficult. This phenomenon is exacerbated by the high tilts required for tomography that increase the projected thickness by a factor of three. Most common specimen preparation methods, such as focused ion beam (FIB), cannot prepare thin enough samples of dense Cu interconnect materials such as Ta and W to avoid contrast reversal artifacts. Thick sections of IC devices are also desirable for a statistically relevant sampling of critical device dimensions by ET reconstructions, but the imaging

technique must produce monotonic intensities for all material thicknesses to ensure a faithful reconstruction of the original structure.

This chapter details the development of a new STEM technique optimized for imaging ultra-thick cross-sections of highly-scattering materials, expanding the capabilities of ET for the microelectronics and materials science communities. A Monte-Carlo (MC) electron scattering program [91] written by the author with relativistic corrections is used to quantitatively model the interaction between a high-energy electron beam and a solid in order to investigate the problems that occur during the imaging of thick specimens. Simulations are compared with experiments of electron beam propagation in high mass-thickness materials to investigate the origin of the ADF contrast reversal. As a result, the novel incoherent bright field (IBF) STEM technique is developed and shown to produce monotonic image intensities at all material thicknesses [5]. The signal is complementary of an ideal ADF detector. Further, IBF-STEM exhibits a superior signal-to-noise ratio (SNR) for thick material sections such that the IBF technique is advantageous even for material thicknesses that do not undergo contrast reversals.

## 3.1 Beam Spreading in Ultra-Thick Cross-sections

The first question is how will beam broadening impact the attainable spatial resolution? As the incident electrons travel through a specimen, they undergo random inelastic collisions with the target material's atoms causing the beam to spread. Goldstein, *et al* [92] estimated the broadening of the beam according to the radius that contains 90% of the scattered incident electrons $R_{90\%}$ at a given material thickness $t$ as

$$R_{90\%} \propto \frac{(Zt^{3/2})}{E_0} \tag{3.1}$$

for a target material's atomic number $Z$ and incident electron energy $E_0$. This estimation is traditionally used to estimate the volume probed for analytical microanalysis and

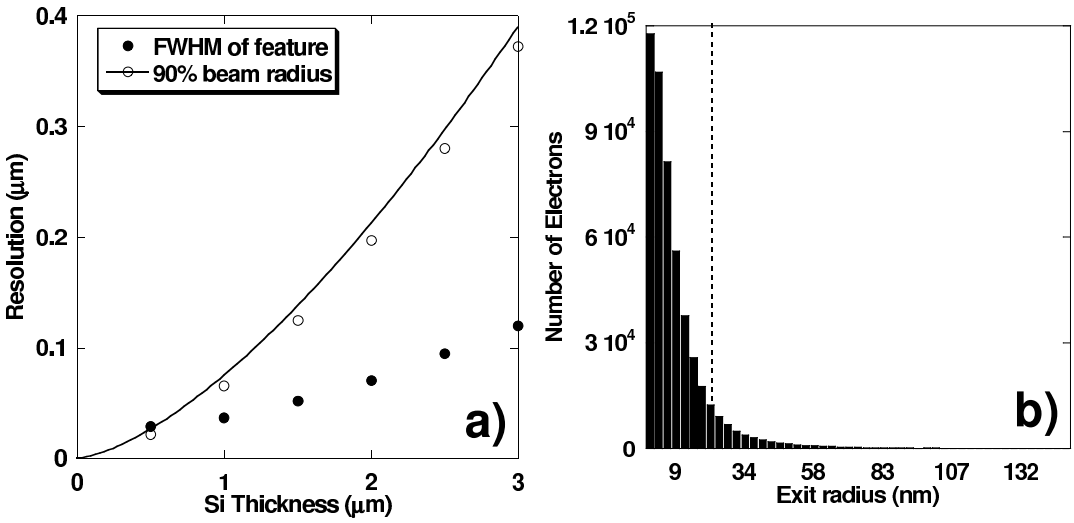


Figure 3.1: a) Monte-Carlo simulations of beam spreading in Si for 300keV incident electrons. The closed dots mark the apparent full-width at half-max (FWHM) of a buried 0.03$\mu$m Au feature as measured after the beam spreads through a given thickness of Si. This is smaller than the resolution predicted by both the simulated 90% beam radius $R_{90\%}$ (open circles) and the resolution predicted by the Goldstein formula from equation (3.1) (solid line). b) Histogram of the exit distance (radius) from the central beam of each 300keV electron after scattering through 1$\mu$m of Si. The radius containing 90% of all electrons ($R_{90\%}$ = 21nm) is indicated by a vertical dashed line. The distribution shows that the $R_{90\%}$ value is biased by few electrons that scatter to very high angles. The data was generated with Monte-Carlo single-scattering simulations of inelastic and elastic electron interactions written by the author based on Joy's work [91]

.

to approximate the attainable imaging resolution for a given specimen thickness. The closed dots in figure 3.1a) show the $R_{90\%}$ measured from MC simulations of electrons transmitted through various thicknesses of Si. The solid line on the figure shows a fit of equation (3.1) to the measured $R_{90\%}$ indicating that the simulated beam broadens consistently with Goldstein's prediction. Figure 3.1b) shows a histogram of the number of 300keV electrons that exit a given distance from the central beam after passing through 1$\mu$m of Si. For these conditions, the $R_{90\%}$ = 21nm and is shown on the plot by a vertical dashed line. This measure of resolution is biased by rare events that scatter a few electrons to large angles producing wide tails in a distribution otherwise strongly peaked at the beam's center. This implies that $R_{90\%}$ is not a good measure of resolution for imaging.

To determine the effect of beam spreading on resolution, the simulated ADF signal was recorded for a probe scanned across a 0.03$\mu$m Au feature on the exit surface of a Si substrate with various thicknesses. The full-width at half-max (FWHM) of the Au particle was determined from the ADF signal collected for each thickness to compare with the $R_{90\%}$ value. The closed dots in figure 3.1a) show the measured FWHM and indicate that the discrepancy between the FWHM of the Au test object and the $R_{90\%}$ grows with thickness. At 1$\mu$m the two measures differ by as much as a factor of five. This comparison of the two measures of resolution shows that $R_{90\%}$ gives an overly pessimistic estimate of image resolution in ultra-thick materials, and therefore image resolution can be maintained for the thicknesses required of microelectronics tomography.

Si is a very common substrate for IC devices, but it is useful to show beam spreading in other materials. Figure 3.2 shows the measured FWHM of a 0.03$\mu$m feature from a beam of 200keV electrons spread through C, Si and Cu substrates. Beam spreading in each different material scales nearly linearly with the average root-mean-square angle

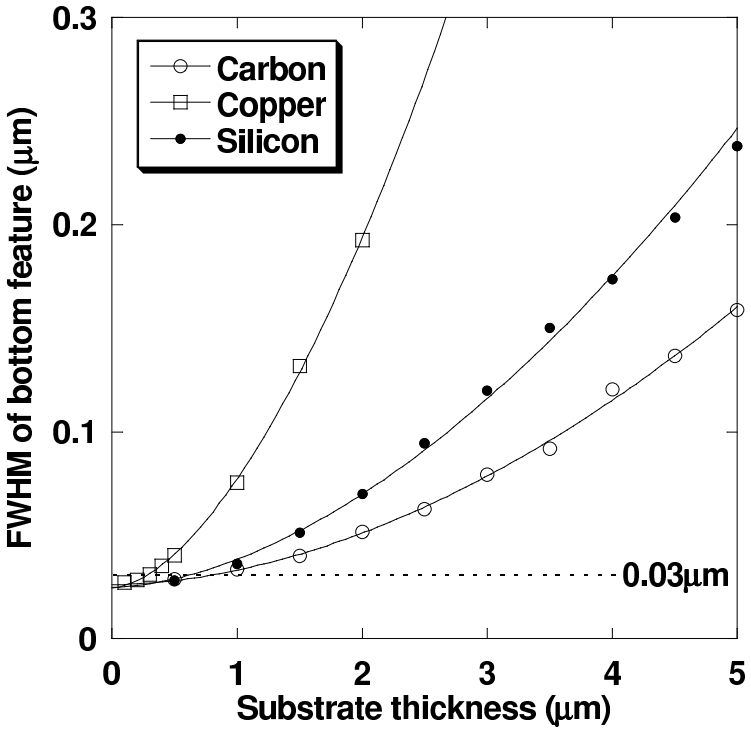


Figure 3.2: Monte-Carlo simulations of beam spreading in C, Si and Cu for 200keV incident electrons. The symbols indicate the apparent full-width at half-max (FWHM) of a buried 0.03$\mu$m Au feature as measured after the beam spreads through a given thickness of each material. The curves for each material are fit to $t^{3/2}$ as expected for multiple scattering of electrons. The horizontal dotted line shows the actual radius of the buried feature.

for multiple scattering of electrons transmitted though a material as $Zt^{3/2}\rho^{1/2}$ [93]. The materials with larger atomic number $Z$ scatter electrons more strongly producing a larger beam at the exit surface. Very thick substrates ( $>>$ 1$\mu$m) severely reduce resolution of buried features.

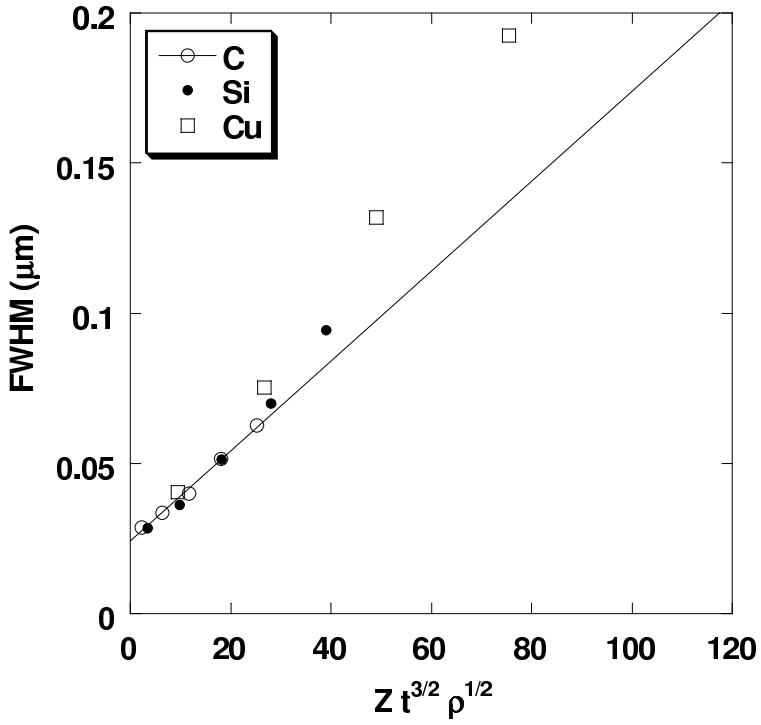


Figure 3.3: Monte-Carlo simulations of beam spreading in C, Si and Cu for 200keV incident electrons. The symbols indicate the apparent full-width at half-max (FWHM) of a buried 0.03$\mu$m Au feature as measured after the beam spreads through varied thicknesses of each material. The average root-mean-square angle for multiple scattering of electrons transmitted though a material varies as $Zt^{3/2}\rho^{1/2}$ [93], which scales nearly linearly (solid line) with the FWHM for each target material.

## 3.2 Contrast Reversals in ADF-STEM Imaging

Figure 3.4a) shows electron scatter ( > 50mrad) onto the ADF detector that commonly occurs for relatively thin material sections. The ADF's outer collection angle is limited by the available space within the microscope column such that some very highly-scattered electrons (including backscatter) are scattered beyond the outer collection range of the detector. Figure 3.4b) shows a diagram of this phenomenon.

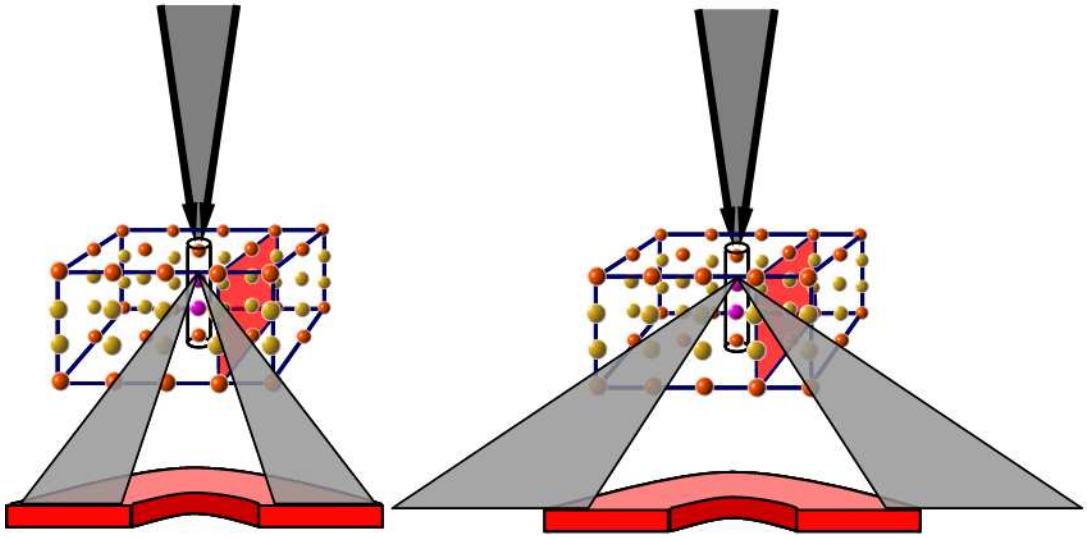

Figure 3.4: A scanning transmission electron microscope (STEM) focuses an electron beam to an Ångstrom-sized spot on the surface of a specimen and uses a post-specimen single-channel detector to collect transmitted electrons scattered within a given solid angle. The outer collection angle of an annular dark field (ADF) detector is limited by available space in the microscope column. The left diagram shows normal scattering to the ADF from a typical thin cross-section, but high mass-thickness materials can scatter the majority of electrons beyond the outer ADF collection range (backscatter is an extreme example). The loss of highly-scattered electrons results in unexpectedly lower image intensities for high-*Z* materials known as contrast reversal.

The simulated transmitted electron intensity through a Cu film as a function of thickness is shown in figure 3.5a) for ADF detectors with different inner collection angles. The peak in each curve indicates the thickness at which the image undergoes a contrast reversal and ceases to provide physically meaningful information. The effect of increasing the ADF inner collection angle only serves to delay the onset of the contrast reversal to slightly thicker material while collecting a smaller portion of the transmitted signal. The average scattering angle of electrons that escape from the exit surface of the specimen and the number of backscattered electrons increases with thickness. Every material

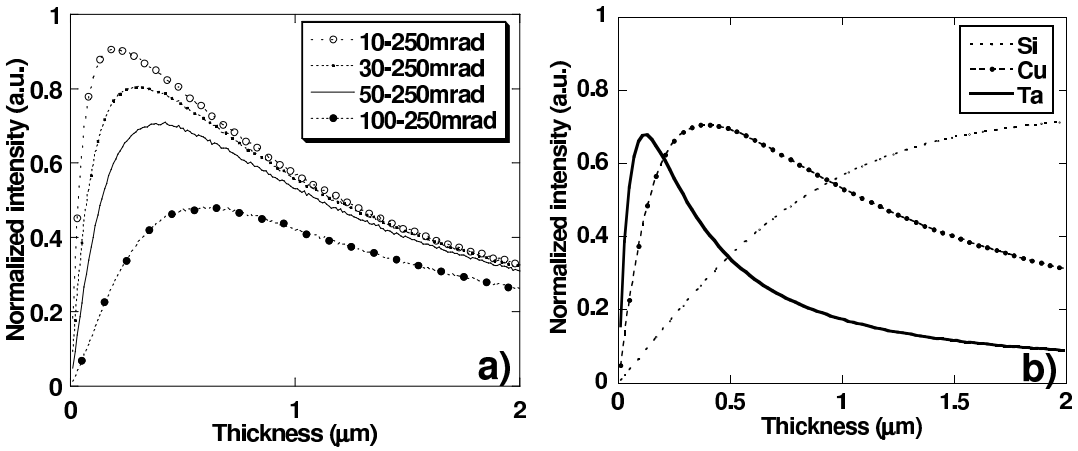


Figure 3.5: a) Simulated transmitted electron intensity of 200keV electrons scattered through Cu for annular dark field detectors with different inner detection angles. b) Transmission functions for an ADF detector collecting 100 – 250 milli-radians (mrad) for 3 elements: Ta, Cu and Si. The peak in the transmission function indicates the thickness at which a contrast reversal occurs. The contrast reversal in Ta occurs at a thickness below the limits of many sample preparation methods, such as focused ion beam milling.

will eventually undergo a contrast reversal, although it may occur at impractically large thicknesses for low-$Z$ materials such as Si.

Figure 3.5b) shows the simulated intensity of 200keV electrons transmitted through different thicknesses of Si, Cu and Ta ($Z = 14, 29, 73$ respectively) incident on an ADF-STEM detector with collection angles of 50 – 250mrad - similar to the detector used in our experiments. The peak in each intensity curve indicates the thickness at which each material undergoes a contrast reversal due to high-angle scatter and backscatter beyond the detector's range and ceases to yield monotonic image intensities. Figure 3.5b) also demonstrates the general trend that higher atomic number materials reverse contrast with thinner material due to enhanced electron scatter. The peaks of Figure 3.5b) specifically predict that Cu and Ta reverse contrast at 390nm and 120nm projected

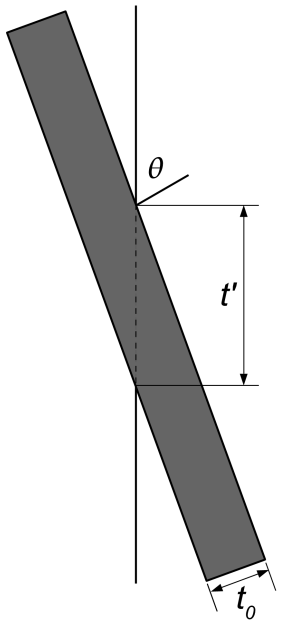


Figure 3.6: Diagram of a TEM specimen prepared in the common slab geometry with a thickness of $t_0$ that is tilted to 70° with respect to the electron beam. Projected thickness $t'$ increases as the secant of the tilting angles $\theta$ and increases by as much as 3× at the highest angles required by tomography. This results in unexpected contrast reversals during tilt-series acquisition of structures containing highly-scattering materials.

thicknesses respectively for these specific ADF detector collection angles (not shown is the Si peak at > 2$\mu$m).

The problem is especially prevalent for moderately thick cross-sections of highly-scattering materials common in IC structures due to the high tilt angles ($\geq 60°$) required for accurate reconstruction in three-dimensions. Specimens commonly prepared in a slab geometry for traditional TEM holders increase in thickness as the secant of the tilting angle $\theta$ during acquisition of a tilt-series. Figure 3.6 shows the geometry of a tilted TEM specimen with original thickness $t_0$ as seen along the tilt axis. The projected thickness $t'$ is much larger than the actual slab thickness, and such high tilting angles

can lead to a 3× increase unexpectedly causing contrast reversal for highly-scattering materials. For example, a TEM sample containing Ta must have $t_0 < 40$nm to produce monotonic image intensities throughout a tilt-series for ET. Tomographic reconstruction algorithms require image intensities be monotonic with specimen thickness throughout the range of tilts, and contrast reversal at high tilts has been shown to introduce void artifacts in three-dimensional reconstructions [5].

## 3.3 Incoherent Bright Field STEM

Electrons with incident energies common in STEM (100 – 200keV) have ranges of hundreds of microns that exceed even the thickest specimens considered here and are not stopped in the specimen [84, 94]. They must escape somewhere, and figure 3.7 shows the three possible exit regions: forward-scattered bright field (BF), highly-scattered dark field (DF) and backscattering. Contrast reversals could be avoided by collecting all electrons scattered within the DF and backscattering regions, but this is impossible to implement because it requires a detector that wraps completely around the specimen (in all but a 6° cone about the optic axis).

The same information could be obtained by collecting the complement of all highly scattered electrons in the form of the forward-scattered electrons, i.e. the 6° cone seen in figure 3.7, as a bright field (BF) signal [95]. This has been overlooked in experimental tomography, because the traditional BF-STEM signal (0 – 10mrad) suffers from coherent imaging artifacts: intensities that oscillate with thickness and zone axis orientation, similar to a CTEM image. However, incoherent simulations of the BF signal by Levine [96, 97] show this to be a promising method for imaging thick sections if there were no coherence problems. The coherence artifacts are most prevalent when the detector col-

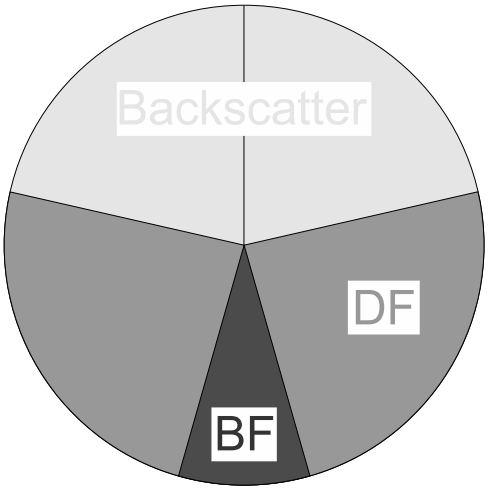


Figure 3.7: High-energy electrons have ranges much larger even than the thickness of ultra-thick TEM specimens, and therefore all incident STEM electrons must exit the specimen. This diagram labels the possible scattering regions for an electron. The forward-scattered bright field (BF) signal is the complement of the backscatter and highly-scattered dark field (DF) electrons. Thus, an incoherent BF (IBF) detector provides the same information as a "perfect" ADF detector that collects the DF and backscattered electrons but avoids contrast reversal.

lection half-angle is small. More precisely, the phase contrast that gives CTEM images their typical speckle is suppressed when the collection angle, $\theta_C$, is larger than the probe convergence, $\theta_P$ [86, 95]. The BF image becomes incoherent when $(\theta_C / \theta_P)^2 >> 1$, often taken as $(\theta_C / \theta_P)^2 \approx 3$ [59, 86], at which point it becomes the complement of the ADF signal [95, 98]. A detector half-angle more than five times larger than that of the probe-forming aperture's is usually sufficient to suppress diffraction contrast and produce the complement of the ADF image [61, 86, 95].

Figure 3.8 shows the simulated transmission functions of different Cu thicknesses for BF-STEM detectors with different detector half-angles, assuming the incoherent imaging conditions are met. All signals are monotonic, a necessary condition to reconstruct

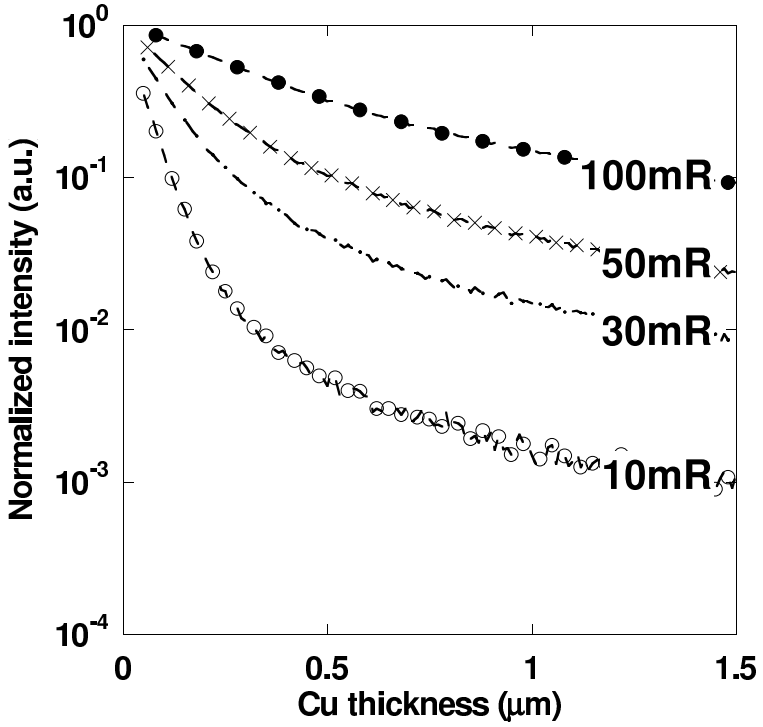


Figure 3.8: The simulated transmission function for BF-STEM detectors with different outer collection angles (in mrad) do not significantly deviate from Beer's law of exponential decay for large half-angles. The signal does not undergo a contrast reversal and allows thick sections of highly-scattering material to be reconstructed in three-dimensions.

object boundaries in ET. To correctly recover relative densities, the functional form of the curve is also required (e.g., Beer's law assumes a simple exponential decay). The BF detectors with higher half-angles produce simpler signals with higher intensities, both of which are desirable for ET. The trade off is acceptance of electrons that have spread further thus degrading spatial resolution [88, 96]. Theory by Levine gives a functional form that could be applied to extend the usable thickness range if the materials type were known [97]. This might be incorporated in an iterative refinement method where the first pass is made using Beer's law to define the boundaries of the different phases.

Table 3.1: The camera lengths and collection angles of the Fischione HAADF-STEM detector installed on the FEI Tecnai F20 microscope at Cornell University.

| Camera length (mm) | Inner collection angle (mrad) | Outer collection angle (mrad) |
|---|---|---|
| 100 | 65 | 323 |
| 80 | 84 | 418 |
| 70 | 97 | 483 |
| 50 | 125 | 623 |
| 40 | 174 | 933 |
| 30 | 226 | 1212 |

### 3.3.1 Implementation of the IBF technique

The IBF-STEM imaging technique collects all the electrons scattered at angles below 100mrad. This is a large enough angle to effectively remove the coherent properties of the image and collect more electrons for a stronger signal. Like HAADF, the signal is incoherent and scales with the atomic number ($Z$) of the scattering elements as $Z^{1.7}$ [59]. Unlike ADF imaging, the incident beam still reaches the detector, requiring a greater dynamic range for the detector, amplifier and readout electronics. Without the improved electronics, there would be little contrast between materials with similar mass-thicknesses – e.g. a-Si and $SiO_2$. Many other common materials of interest to the microelectronics industry have large atomic number differences (such as Si, Cu and Ta) and do not suffer from this drawback. Experiments were conducted in an FEI Tecnai TF20 operating in STEM mode and outfitted with a high-sensitivity Fischione HAADF detector (based on a design by Thomas and Kirkland [60]). The standard FEI preamplifier was replaced with a low-noise, high-gain Hamamatsu C7319 amplifier to increase

the dynamic range, which we know to be crucial in attaining acceptable signal-to-noise levels for the IBF method [99]. The BF detectors installed in the F20 STEM are incapable of collecting such a large range of scattered electrons and provide insufficient signal quality. Therefore, the IBF technique was implemented by shifting the beam axis between the HAADF detector's inner and outer radius (with the post-specimen diffraction shifts) to create a BF detector with the necessarily large collection angle. Table 3.1 shows the inner and outer collection angles in mrad measured for the Fischione HAADF-STEM detector installed on the FEI Tecnai F20 electron microscope at Cornell University. An IBF detector that collects 0 – 129mrad is possible by this technique at the 100mm camera length, although it does not provide a symmetrical detector.

It is important to note that IBF-STEM imaging requires a high dynamic range, low noise electron detector to distinguish small changes in transmitted intensity at each raster position from the intense, unscattered electron beam continually incident on the detector. Inadequately sensitive detectors and noisy readout electronics will produce images with insufficient contrast to distinguish materials as the beam rasters across the sample. This is the major hurdle to implementing this imaging technique in many existing microscopes, which may require some modification to amplifier and readout electronics.

## 3.4 Comparison of ADF- and IBF-STEM Imaging

So far, IBF-STEM was utilized only as a replacement for ADF-STEM imaging to provide artifact-free projection images of ultra-thick cross-sections possibly affected by contrast reversal. The two techniques provide complementary image intensities for relatively thin material sections (ignoring noise), but their SNRs exhibit opposite trends with increasing thickness due to the number of electrons scattered to each detector. Therefore,

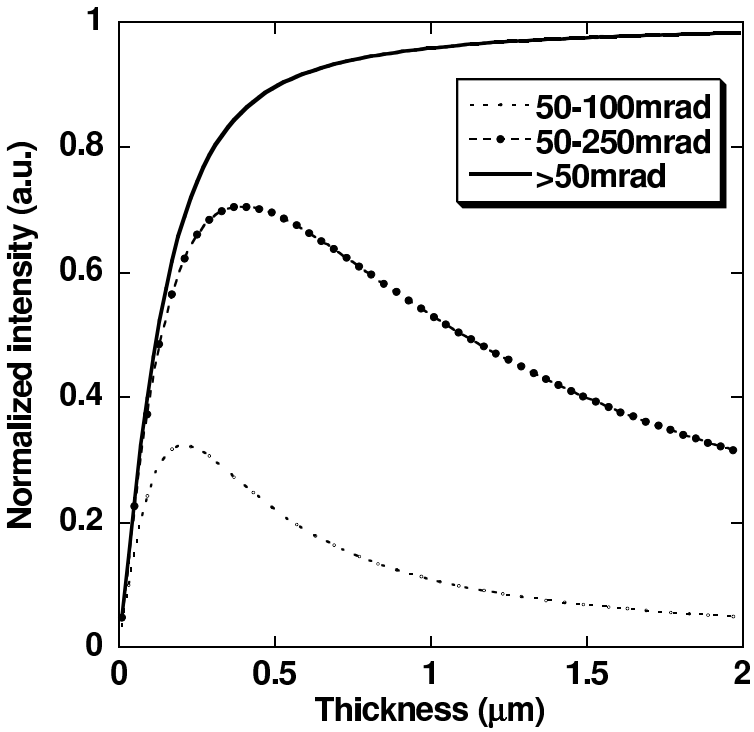


Figure 3.9: Monte-Carlo simulations of the transmitted electron signal for 200keV electrons scattered through different thicknesses of Cu. Contrast reversal occurs at greater thicknesses for larger outer collection angles. No contrast reversal occurs for a ”perfect” ADF detector that collects all highly-scattered electrons > 50mrad including backscatter.

is there a range of thicknesses for any material at which the IBF-STEM technique provides superior imaging conditions compared to ADF? In this section, the SNR is used as a measure for image quality to produce a general relationship determining which method is better suited for imaging any material at a given thickness. High SNR is especially important in metrology to distinguish materials and their interfaces for measurements critical structural dimensions.

### 3.4.1 Signal-to-Noise Ratios for STEM Imaging Techniques

To allow simple analytical comparisons, all scattering from a target material is designated as high-angle ADF (HAADF) scattering ( > 100mrad) or low-angle IBF scattering ( < 100mrad), and MC simulations of transmitted electron intensity for various materials are used to determine the expected SNRs for STEM detectors collecting electrons scattered within these two regimes. The collection efficiency of such a ”perfect” HAADF detector (perfect in that it collects even backscattered electrons), shown as a solid black line in figure 3.9, excludes contrast reversals from the simulations, but this simplification allows an analytical comparison between the HAADF and IBF imaging techniques. Allowing for a non-ideal HAADF detector reduces the HAADF SNR.

Similarly to the discussion in section 3.3 and figure 3.7, all incident electrons ($I_0$) are accounted for in the two scattering regimes being considered such that the entire system follows the equation

$$I_0 = I_{HAADF} + I_{IBF} \tag{3.2}$$

where $I_{HAADF}$ and $I_{IBF}$ are the number of electrons collected by a ”perfect” HAADF and an IBF detector respectively. To compare the useful information collected by each detector, $I_{HAADF}$ and $I_{IBF}$ must be referenced to the number of electrons collected by each technique when the beam passes only through vacuum without any scattering events. No electrons are scattered in vacuum such that the HAADF signal is simply the number of electrons collected ($I_{HAADF}$), but the unscattered beam is always incident on the IBF detector which produces a signal given by $I_0 - I_{IBF}$. Thus, the full unscattered electron beam introduces a large noise component that overwhelms IBF image intensities for thin material sections, but HAADF avoids the central beam providing lower noise in equivalent conditions. As material thickness increases, more electrons scatter out of the central beam oppositely affecting the noise of each technique, which is determined by

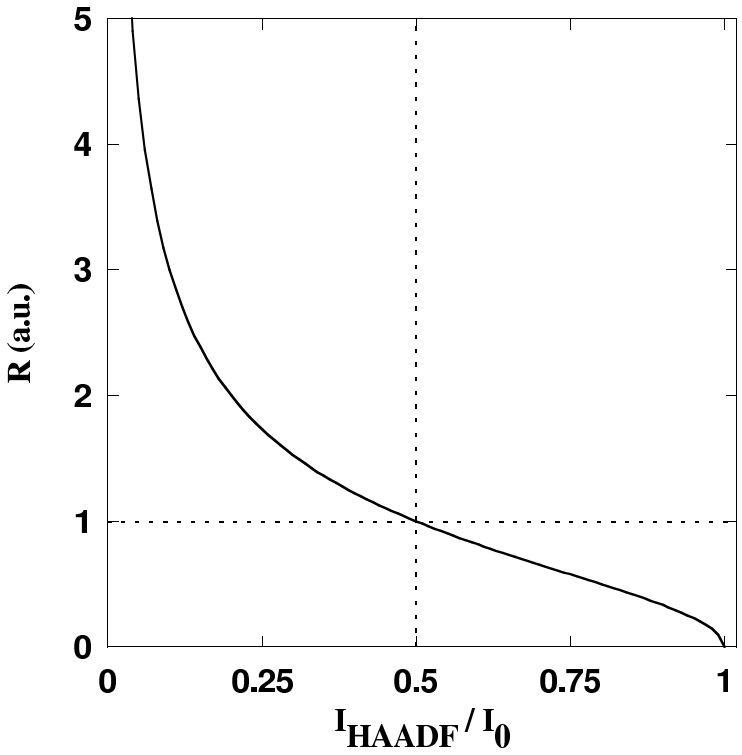


Figure 3.10: Plot of $R$, the ratio of $\mathrm{SNR}_{HAADF}$ and $\mathrm{SNR}_{IBF}$, from equation (3.6) where all electrons scattered > 100mrad are collected by a "perfect" HAADF detector (including backscatter). Image quality for the two techniques is equivalent when $\mathrm{SNR}_{HAADF} = \mathrm{SNR}_{IBF}$ which occurs when 50% of incident electrons scatter >100mrad. When this condition is met, the IBF detector provides superior imaging conditions for increased electron scattering.

the square root of the number of collected electrons. The SNRs are defined as

$$\mathrm{SNR}_{HAADF} = \frac{I_{HAADF}}{\sqrt{I_{HAADF}}} \tag{3.3}$$

$$\mathrm{SNR}_{IBF} = \frac{(I_0 - I_{IBF})}{\sqrt{I_{IBF}}} \tag{3.4}$$

Using equation (3.2), the right hand side of equation (3.4) is rewritten

$$\mathrm{SNR}_{IBF} = \frac{I_{HAADF}}{\sqrt{I_0 - I_{HAADF}}} \tag{3.5}$$

where only $I_0$ and $I_{HAADF}$ remain. Let $R$ represent the ratio of the two SNRs to give the relation

$$R \equiv \frac{\text{SNR}_{HAADF}}{\text{SNR}_{IBF}} = \sqrt{\frac{I_0}{I_{HAADF}} - 1} \tag{3.6}$$

$R$ is plotted in figure 3.10 to show that the HAADF image quality is superior to IBF when few electrons scatter to high angles such that $I_{HAADF} << I_0$ (as in thin material sections). $R$ decreases rapidly as the HAADF intensity increases until the SNRs are equivalent ($R = 1$) when

$$I_{HAADF} = \frac{I_0}{2} \tag{3.7}$$

and continues to drop. Thus, the IBF signal becomes advantageous when more than 50% of incident electrons scatter to high angles beyond the IBF detector.

### 3.4.2 General Function to Determine the IBF ”Cutoff” Thickness

An IBF detector is advantageous over a HAADF detector for material thicknesses that scatter >50% of incident electrons beyond the IBF outer collection angle. We designate this ”cutoff” thickness by $t_{1/2}$ in the following expressions and show that it strongly varies with target material and incident electron energy in table 3.2. In this section, a general relation is determined for high-energy electrons that describes the range of thicknesses suitable for either HAADF- or IBF-STEM imaging for any material.

Beer’s law describes the exponential attenuation due to scattering of an incident electron beam transmitted through a thickness $t$ of a target material as

$$I = I_0 e^{-\rho\, t/x_{el}} \tag{3.8}$$

where $\rho$ is the density with units $\text{g} \cdot \text{cm}^{-3}$ and $x_{el}$ is the material’s elastic mean-free-path for electrons with units $\text{g} \cdot \text{cm}^{-2}$ [84]. Substituting in the condition from equation (3.7)

into equation (3.8) gives

$$\frac{I_0}{2} = I_0\, e^{-\rho\, t_{1/2}/x_{el}} \tag{3.9}$$

which relates the elastic mean-free-path to the cutoff thickness $t_{1/2}$ for any material. Further, the actual distance between elastic scattering events $\Lambda_{el}$ (with units of cm) is given by dividing $x_{el}$ by the material's density

$$\Lambda_{el} = \frac{x_{el}}{\rho} \tag{3.10}$$

Substituting for this and rearranging the terms in equation (3.9) yields

$$t_{1/2} = \Lambda_{el} \ln(2) \tag{3.11}$$

which predicts a linear relationship between $t_{1/2}$ and $\Lambda_{el}$. Table 3.2 tabulates $t_{1/2}$ for various materials (with the pertinent material parameters) and incident energies as determined from MC simulations, but an analytical determination of the elastic mean-free-path is useful to determine the cutoff thickness for any material.

### 3.4.3 The Rutherford Elastic Mean-Free-Path

The Rutherford total elastic cross-section for large-angle scattering ($\sigma_{el}$ is used to estimate the elastic mean-free-path $\Lambda_{el}$ of electrons scattering in any material is given by

$$\sigma_{el} = \left(\frac{E + E_0}{E + 2E_0}\right)^2 \left(\frac{2\pi q^4}{(8\pi\epsilon_0)^2}\right)\left(\frac{Z^{1.7}}{E^2}\right)\left[\cot^2\left(\frac{\theta}{2}\right)\right] \tag{3.12}$$

where $E$ is the incident electron energy, $E_0$ is the electron rest energy, $\epsilon_0$ is the permitivity of free space, $q$ is the electron charge and $\theta$ is the electron scattering angle [84]. The analytically derived Rutherford cross-section varies as $Z^2$, but a more accurate prediction of scattering from the high-$Z$ materials under investigation is obtained using the empirically determined $Z^{1.7}$ parameter [59]. Absolute values for $\sigma_{el}$ calculated with

Table 3.2: Material parameters used in calculations and simulations of the cut-off thickness ($t_{1/2}$) for an IBF detector with outer collection angle of 100mrad. $t_{1/2}$ is determined from Monte-Carlo single-scattering simulations as the thickness at which 50% of incident electrons scatter >100mrad. $t_{1/2}$ is too large to simulate for 200 and 300keV incident electrons.

| | Z | $A_t$ (g) | $\rho$ (g · cm$^{-3}$) | 100keV $t_{1/2}$ ($\mu$m) | 200keV $t_{1/2}$ ($\mu$m) | 300keV $t_{1/2}$ ($\mu$m) |
|---|---|---|---|---|---|---|
| Ta | 73 | 180.9479 | 16.65 | 0.035 | 0.09 | 0.16 |
| Cu | 29 | 63.546 | 8.92 | 0.11 | 0.305 | 0.55 |
| Si | 14 | 28.086 | 2.33 | 0.67 | 1.93 | 3.3 |
| Au | 79 | 196.97 | 19.32 | 0.025 | 0.073 | 0.13 |
| C | 6 | 12.0107 | 1.2 | 2.5 | N/A | N/A |
| Ge | 32 | 72.61 | 5.323 | 0.175 | 0.49 | 0.88 |
| Mo | 42 | 95.94 | 10.22 | 0.075 | 0.21 | 0.37 |
| Ti | 22 | 47.867 | 4.54 | 0.26 | 0.75 | 1.35 |

equation (3.12) do not agree well with experiments due to the failure of the Born approximation in high-$Z$ materials and insufficiently accounting for screening of the target atoms' nucleus [84, 100]. However, equation (3.12) is useful to find a proportionality relationship with the IBF cutoff thickness $t_{1/2}$ as in equation (3.11). To this end, $\sigma_{el}$ is related to the actual distance between elastic scattering events $\Lambda_{el}$ (with units of cm) as electrons propagate through a material by the relation

$$\sigma_{el} = \frac{A_t}{N_A \rho \Lambda_{el}} \tag{3.13}$$

where $A_t$ is the atomic weight and $N_a$ is Avogadro's number. Removing the extraneous physical constants from the Rutherford cross-section in equation (3.12) and combin-

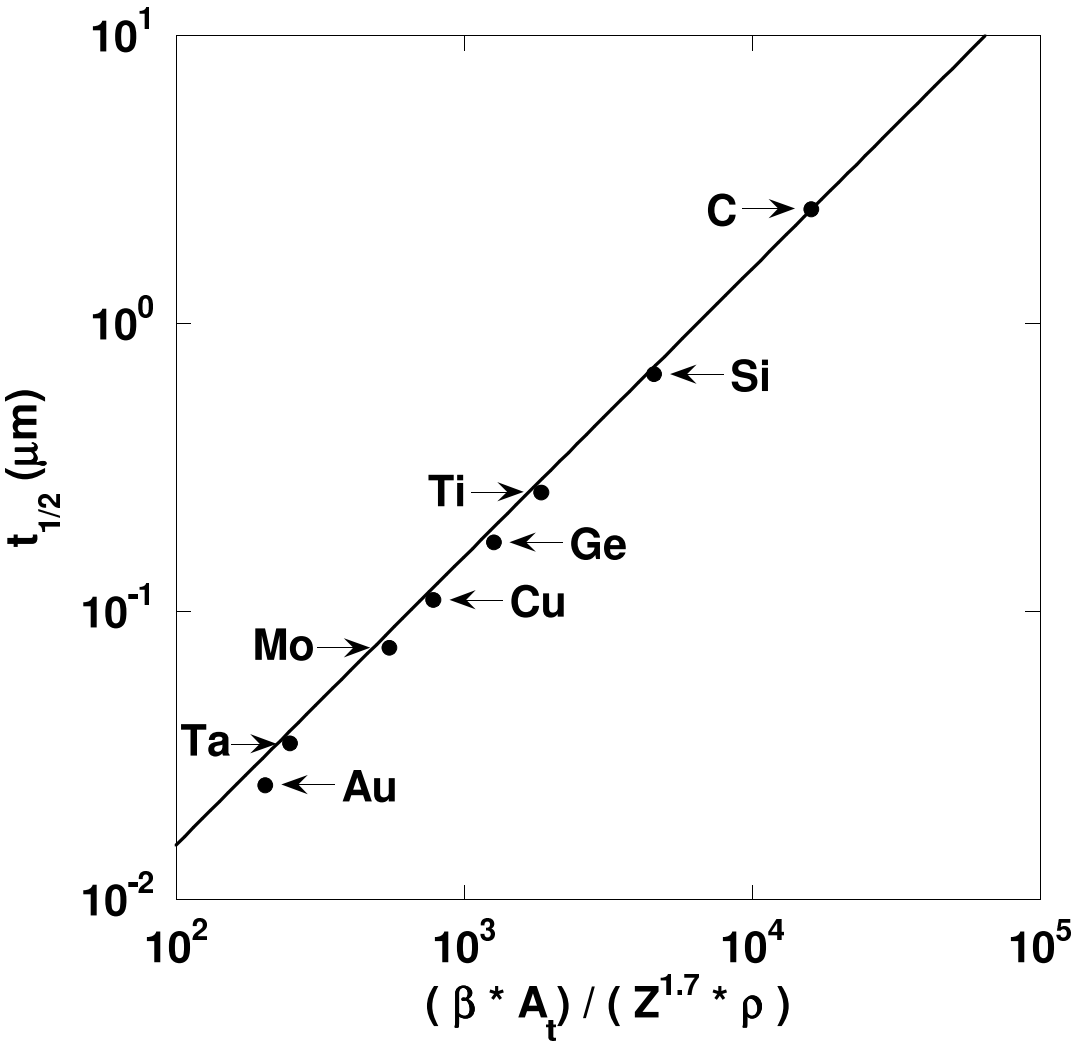


Figure 3.11: A log-log plot of a material's elastic mean-free-path as calculated by the Rutherford cross-section for 100keV electrons against the thickness at which 50% of incident electrons scatter > 100mrad for various elements. The Rutherford calculation uses the empirically derived $Z^{1.7}$ dependence (see equation (3.12)). The simulations and calculations utilize a wide range of materials producing a general relationship. Equation 3.16 gives a linear fit to the data that estimates the cutoff thickness $t_{1/2}$ above which IBF-STEM images exhibit higher SNR compared to HAADF-STEM.

ing with equations (3.11) and (3.13) yields a general relationship between fundamental material parameters and the IBF cutoff thickness as

$$t_{1/2} \propto \left( \frac{\beta A_t}{Z^{1.7} \rho} \right) \tag{3.14}$$

where $t_{1/2}$ has units $\mu$m. $\beta$ is a correction for relativistic energies calculated by

$$\beta = E^2 \left( \frac{E + 2E_0}{E + E_0} \right)^2 \tag{3.15}$$

Figure 3.11 shows a log-log plot of $\Lambda_{el}$ against $t_{1/2}$ for 100keV electrons using equation 3.14 and the parameters provided in table 3.2. The linear relationship holds for a wide range of materials, and can therefore predict the IBF cutoff thickness for any material. Figure 3.12 shows similar data for 100, 200 and 300keV incident STEM electron energies and a fit of the data for all energies given by

$$t_{1/2} = 1.11 \times 10^{-4} \left( \frac{\beta A_t}{Z^{1.7} \rho} \right) \text{ in } \mu\text{m} \tag{3.16}$$

This equation determines the thickness at which an IBF-STEM detector with outer collection angle of 100mrad provides superior imaging conditions compared to a complementary HAADF detector.

$t_{1/2}$ for some lighter materials (such as C) is too large to be considered as a realistic TEM specimen thickness, and only HAADF should be used for those materials. Equation 3.16 is most useful to determine the suitable imaging technique for thick cross-sections containing high-$Z$ materials taking into account the full range of thicknesses encountered throughout tomographic data acquisition (3× increase at 70°). High SNR is important for images acquired at high tilts that sample high-frequency information along the sample thickness ($k_z$ in figure 1.4). Otherwise, fine details are lost in the noise obscuring critical structural features along the projection direction in the final three-dimensional reconstruction.

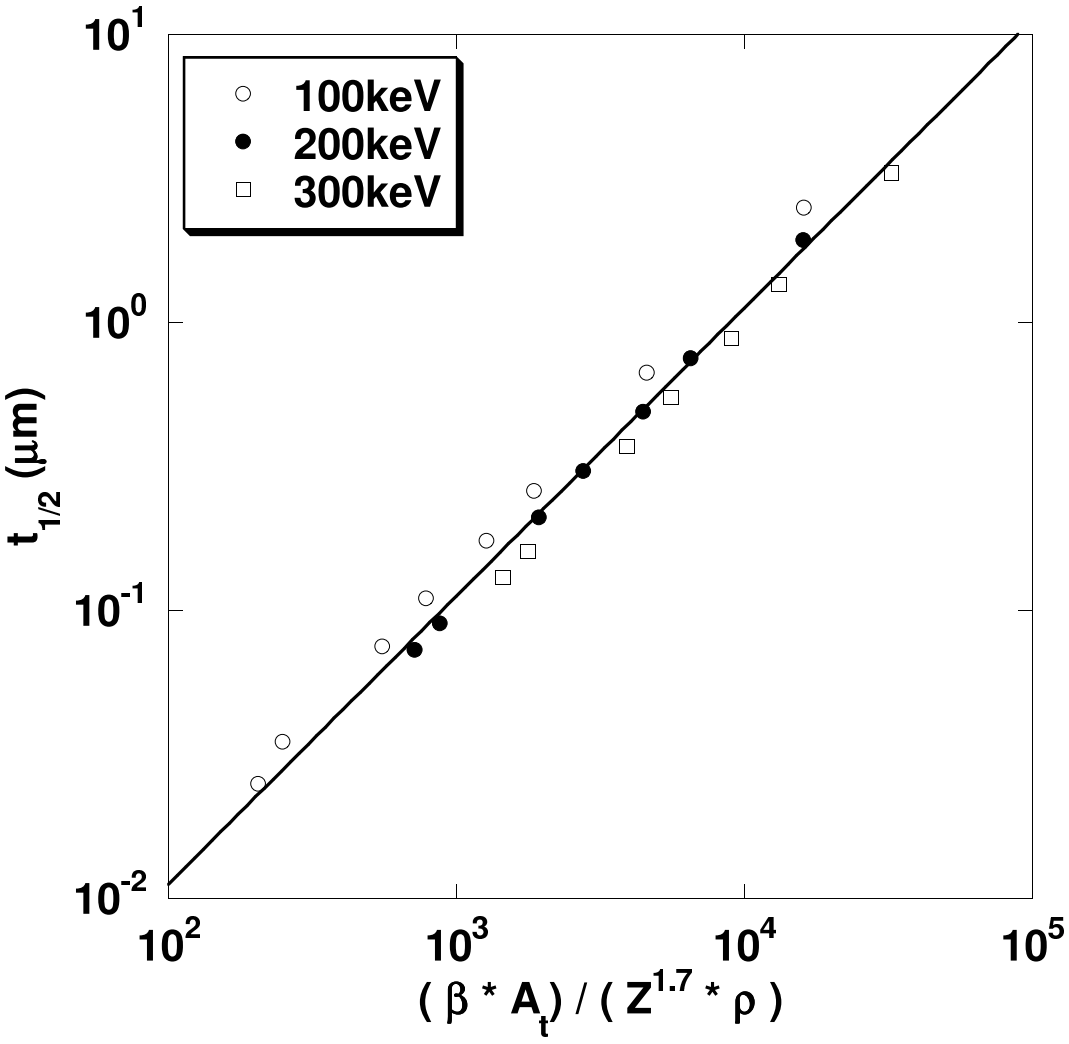


Figure 3.12: A log-log plot of the thickness at which the signal-to-noise ratio of the HAADF and IBF imaging techniques are equal for various elements against the material mean-free-path as calculated by the Rutherford cross-section for 100, 200 and 300keV electrons. The Rutherford calculation uses the empirically derived $Z^{1.7}$ dependence, assumes a perfect ADF detector and assumes the outer IBF collection angle is 100mrad. The linear fit detailed in equation 3.16 provides a general estimation for the cutoff thickness $t_{1/2}$ above which IBF-STEM images exhibit higher SNR than HAADF-STEM for any material.

## 3.5 Conclusions

Conventional electron microscopies have proven inadequate for imaging complicated structures due to the overlap of features in projection. The emergence of smaller and denser devices in microelectronics will necessitate the application of electron tomography for a complete understanding of their three-dimensional structure. Traditional techniques produce transmission functions with a non-monotonic dependence of intensity on thickness for common microelectronic materials, making them unsuitable for tomography. We wrote a custom MC electron single-scattering code to investigate scattering interactions between high-energy electrons that cause contrast reversal in HAADF-STEM imaging and developed a novel IBF-STEM technique capable of imaging ultra-thick cross-section of highly-scattering materials.

The size of an electron beam propagating in a material increases, which reduces the attainable image resolution for a given specimen thickness. MC simulations provided the radius that contains 90% of electrons at the exit surface of a thick substrate ($R_{90\%}$), which is biased to large values by relatively few high-angle scattering events. A large discrepancy exists between $R_{90\%}$ and the measured FWHM of a Au feature at the sample's exit surface, indicating $R_{90\%}$ is a poor estimation of image resolution. We expect image resolution is maintained even for ultra-thick cross-sections for electron tomography.

Contrast reversals occur in HAADF-STEM images when the majority of electrons are scattered beyond the detector's outer collection angle. The average scattering angle of transmitted electrons and the electron backscatter yield increase with thickness for any material, and contrast reversals are ultimately unavoidable for HAADF. Some low-$Z$ materials, however, require projected thicknesses of several microns to reverse

contrast at 200keV. The phenomenon is especially prominent in ET, because projected material thickness increases as the secant of the tilt angle, leading to a 3× increase at the highest tilt angles. Chapter 2 concludes that the most efficient use of ET involves reconstruction of a relatively large portion of the overall structure for a statistically significant sampling of possible device variations. ADF-STEM does not always provide monotonic image intensities throughout a tomographic tilt-series, which may produce image artifacts indistinguishable from material voids in a reconstruction.

IBF-STEM presents an alternative imaging technique complementary to traditional HAADF-STEM but exhibits monotonic, predictable behavior capable of producing artifact-free three-dimensional reconstructions of material cross-sections up to 1$\mu$m in thickness that are not possible with traditional HAADF-STEM. This allows many measurements of critical device parameters for statistically relevant sampling of extended structures. A large noise component due to the unscattered electron beam incident on the IBF detector can overwhelm any signal at low thicknesses, but the signal and noise simultaneously improve with increased material thickness compared to the complementary ADF technique. The IBF technique provides superior imaging conditions, as measured by SNR, even before HAADF reverses contrast, and this chapter provides an equation to determine the suitable imaging technique for any given material thickness. This is especially useful for minimizing SNR in projection images of ultra-thick cross-sections for well defined material feature boundaries that allow accurate structural measurements in three-dimensional reconstructions.

CHAPTER 4

# USE OF IBF-STEM IMAGING TO RECONSTRUCT ULTRA-THICK CROSS-SECTIONS OF HIGHLY-SCATTERING MATERIALS

In the current chapter, we compare experimental incoherent bright field (IBF) and annular dark field (ADF) STEM images of an ultra-thick cross-section to demonstrate IBF's validity for electron tomography (ET) when traditional imaging techniques fail to provide directly interpretable image contrast. A tilt-series acquired by high-angle annular dark field (HAADF) STEM of a stress void at the juncture of a Cu Damascene via-to-wire interconnect structure shows that contrast reversal artifacts propagate into the final three-dimensional reconstruction. IBF tilt-series images of the same ultra-thick cross-section produce a faithful three-dimensional reconstruction of the stress void without artifacts, and allow qualitative analysis of the stress void.

## 4.1 STEM Projection Images of an Ultra-Thick Cross-Section

As discussed in section 1.4.1, a STEM rasters a beam of electrons focused to an Ångstrom sized spot across the surface of a specimen and uses post-specimen single-channel detectors to collect transmitted electrons scattered within a specific solid angle at each raster position. The inner and outer collection angles of a STEM detector determine the contrast mechanisms that dominate the resulting image. HAADF detectors collect only highly-scattered electrons (see figure 3.4) to provide incoherent image intensities that vary with the atomic number ($\propto Z^{1.7}$) and projected thickness of the target material – known as $Z$-contrast imaging [2, 55, 59]. Regions of higher mass-thickness in a TEM specimen of typical thickness (20 – 50nm) produce higher, or whiter, image intensity [55]. In general, the atomic number of the target atoms at each raster potion

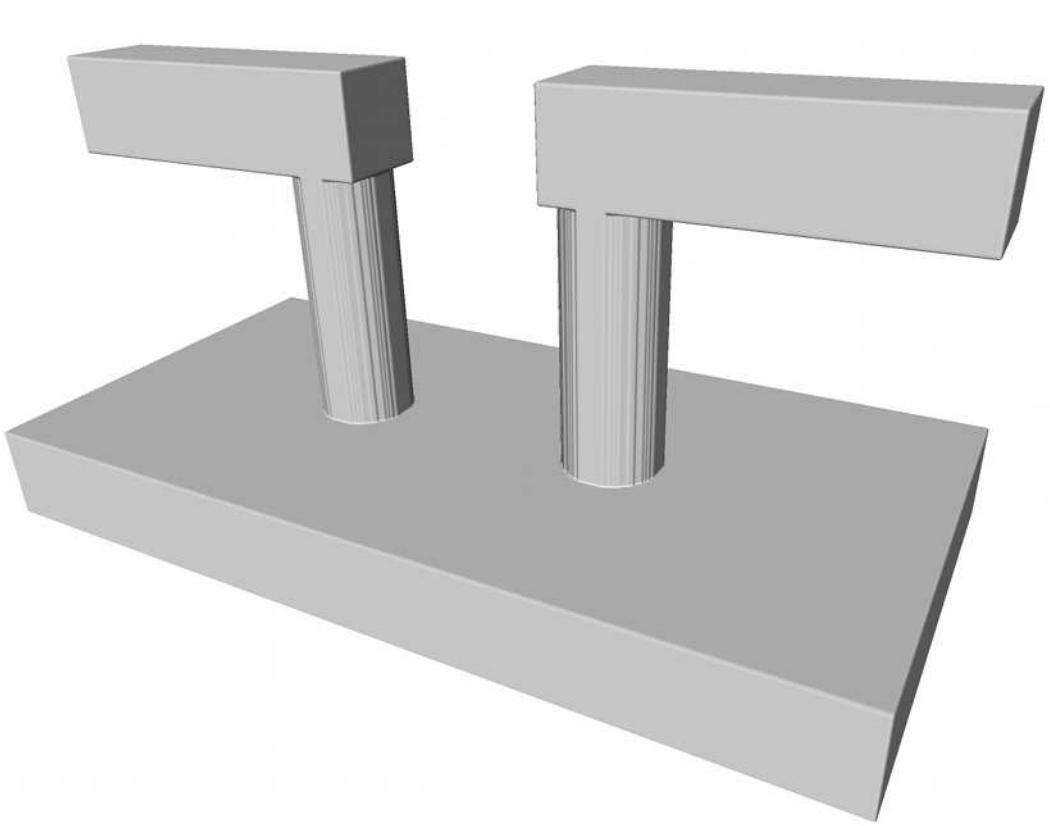

Figure 4.1: A three-dimensional model of the Cu wire-to-via structure, excluding the stress void, used to test the incoherent bright field (IBF) technique throughout this chapter. The top Cu wires have approximately square cross-sections and are connected to the lower extended Cu pad by round Cu vias. This figure simply shows a perspective view of the interconnect geometry corresponding to figure 4.2's top-down SEM image and figure 4.3's cross-section STEM image. The figure does not show an experimental reconstruction.

dominates the ADF-STEM image contrast allowing direct material differentiation by image intensity.

### 4.1.1 Cu Damascene Interconnect Structure with Stress Void

The Cu interconnect used for ET in this chapter is an example of IBM's first generation of devices manufactured with Cu metallization [12]. The investigated structure consists of two wire segments above an extended solid pad with two round vias connecting the upper and lower structures. Figure 4.1 shows a three-dimensional model of the wire-to-via structure in perspective, clearly indicating the interconnect's overall geometry for comparison with figure 4.2 and figure 4.3, excluding the stress void. The figure does not show an experimental reconstruction.

Figure 4.2 shows a scanning electron microscope (SEM) image from above of the nominally 280nm wide interconnects composed of a TaN/Ta barrier layer filled with Cu by the dual-Damascene process discussed in section 1.1.2. The subsurface structure was imaged using high-energy incident electrons that penetrate deep into the material and backscatter out [101]. The slight discoloration above the left via is the stress void of interest, but the void's size and extent under the via are indeterminate from this perspective. More detailed analysis is required to deduce whether the void reduces the interconnect's current carrying capacity or results in an open circuit.

The entire structure between the dashed lines in figure 4.2 is extracted from the substrate using a focused ion beam (FIB) technique known as *lift-out* for cross-sectional TEM analysis [54]. The resulting ultra-thick cross-section is $\sim$ 500nm thick, which proves difficult to image by traditional STEM techniques without artifacts. Lynne Gignac prepared the sample for analysis at the IBM T.J. Watson Research Center.

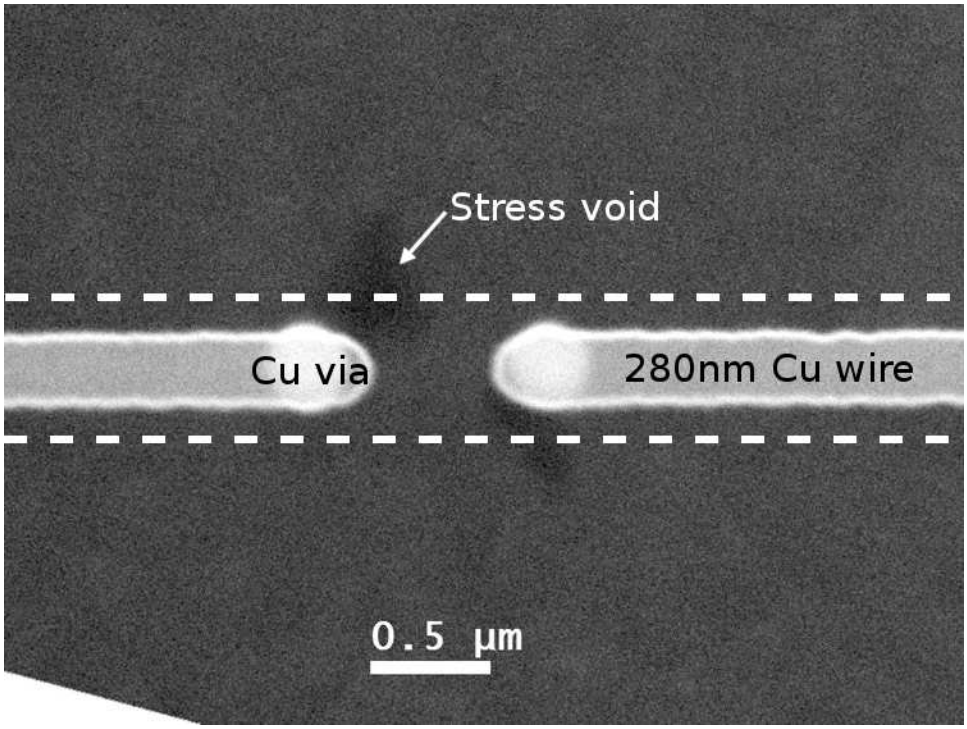


Figure 4.2: A scanning electron microscope (SEM) image of Cu Damascene interconnect wire-to-via structures. A backscatter electron detector was used to image the subsurface features from high-energy incident electrons that penetrate deep into the specimen surface and backscatter out [101]. The wires are 280$\mu$m wide, including the TaN/Ta barrier layer. The slight discoloration is a stress void, but the extent to which the void undercuts the via is obscured by the via itself. A large void at this location would create an open electrical connection. The entire structure is cut from the bulk along the dotted lines to make a TEM specimen nearly 0.5$\mu$m thick. Image courtesy of Lynne Gignac, IBM.

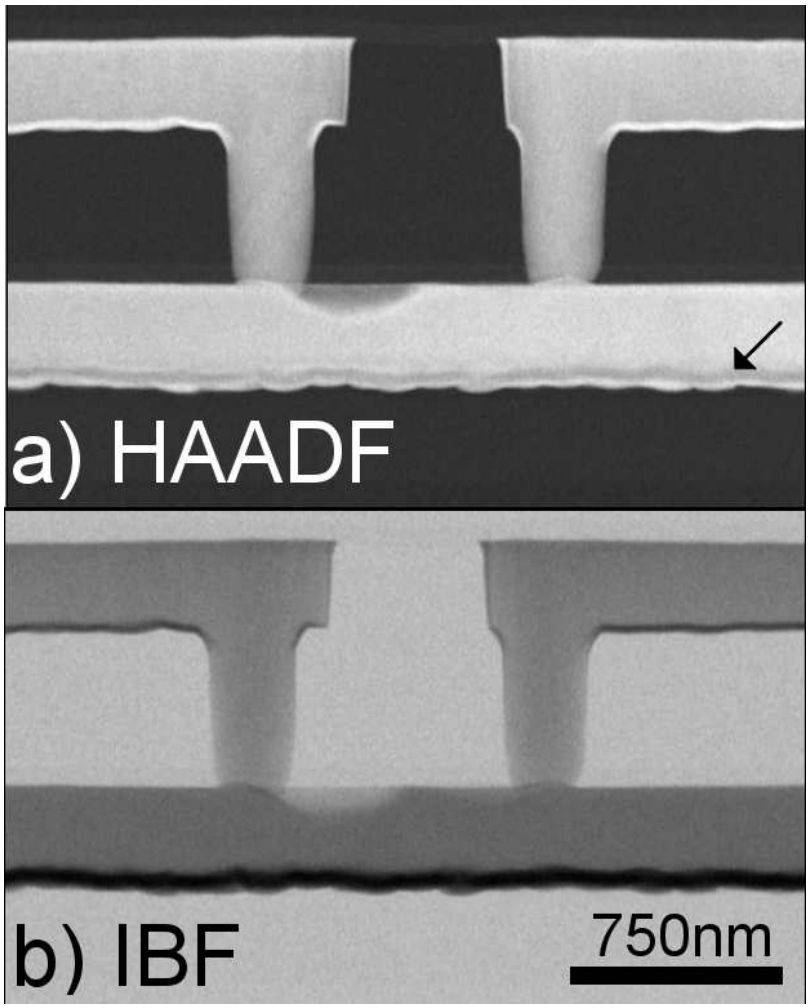


Figure 4.3: a) HAADF-STEM and b) IBF-STEM cross-sectional images of the via-to-wire structure at 0° tilt with a stress void near the left via. The 500nm thick sample contains the entire interconnect structure. The black arrow on the HAADF image marks a contrast-reversal artifact at the Cu/Ta interface resembling a void, which is not present in the IBF image. This TEM cross-section is therefore thick enough to reverse contrast even at 0° tilt. HAADF-STEM *Z*-contrast is non-monotonic and unsuited to three-dimensional reconstruction by electron tomography.

Figure 4.3a) shows a 0° tilt HAADF-STEM image of the interconnect structure in cross-section acquired by the FEI Tecnai F20 STEM equipped with a Fischione HAADF detector at Cornell University. The approximate HAADF collection angles are $65 < \theta_C < 323$mrad. The exact size or position of the stress void near the left via cannot be determined from the cross-sectional view due to the overlap of features along the projection direction. A black arrow on the HAADF image marks a dark band along the lower Cu/Ta barrier interface that resembles a void if *Z*-contrast is assumed. In fact, this void-like feature is an image artifact produced by contrast reversal of the highly-scattering Ta barrier (as discussed in chapter 2), which challenges the reliability of HAADF *Z*-contrast image intensities for other features. Figure 4.3b) shows an IBF-STEM image of the same interconnect structure with image contrast complementary to the corresponding HAADF image, but the void-like dark band at the lower Cu/Ta interface is not shown. We implemented the IBF imaging technique by shifting the beam axis between the HAADF detector's inner and outer radius (as outlined in section 3.3.1) to create an IBF detector with an $\sim$ 130mrad outer collection angle. The make-shift IBF detector is not symmetrical like a normal BF detector but is a sufficient approximation to test the technique's validity. This structure is ideal to test IBF-STEM's imaging capabilities for an ultra-thick TEM specimen that reverses contrast.

### 4.1.2 Contrast Reversal at High Tilts for Electron Tomography

As shown in figure 4.3a), the interconnect cross-section investigated in this chapter contains sufficient material in projection for some features to reverse contrast at 0° tilt. This effect worsens at high tilt angles required for three-dimensional ET due to increased projected thickness. To demonstrate this effect, figure 4.4a) shows a HAADF-STEM image of a rectangular wire and a round via acquired at 0° tilt, which exhibits normal

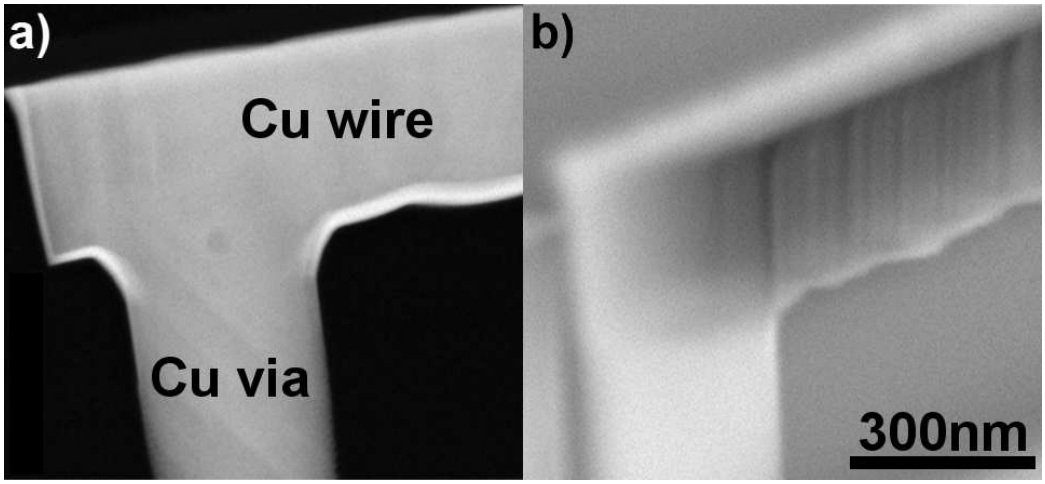


Figure 4.4: Two HAADF-STEM cross-section images of the Cu Damascene interconnect structure with a TaN/Ta barrier layer. A rectangular Cu wire connects horizontally to a round, vertical via. a) At 0° tilt the ADF-STEM image exhibits consistent *Z*-contrast: high density materials produce higher, or whiter, intensities. b) The structure is tilted to 70° around the vertical image axis, increasing the projected thickness of the rectangular Cu wire by 3×. The wire reverses contrast along its length due to the majority of electrons scattering beyond the HAADF detector's outer collection range. The round via maintains the same projected thickness and does not reverse contrast. Non-monotonic behavior of HAADF intensities for high mass-thickness materials produce image artifacts similar to material voids that appear in three-dimensional ET reconstructions.

*Z*-contrast image intensities for the Cu and Ta features. Figure 4.4b) shows the same structure tilted to 70° around the vertical image axis, which now exhibits anomalous image intensities along the Cu wire. The wire overlaps in projection when titled around the axis perpendicular to its length, resulting in a 3× larger projected thickness relative to its width (see figure 3.6). At 70° tilt the wire should be the brightest object in the image, but its intensity is lower than expected due to electrons that scatter beyond the HAADF detector's outer collection angle (see diagrams in figure 3.4). The resulting non-monotonic

HAADF behavior with increasing thickness produces image artifacts similar to actual material voids. The round via, unlike the wire, in figure 4.4 presents the same projected thickness regardless of tilt angle and does not reverse contrast. ET reconstruction algorithms assume a monotonic relationship between image intensity and projected mass-thickness [68], and therefore contrast reversal artifacts are interpreted as voids in the structure. Accurate assessments of features are difficult for three-dimensional reconstructions with contrast reversal artifacts, because apparent voids could be caused by contrast reversal or actual material voiding.

Sections 3.2 and 3.3 show MC simulations of expected transmitted electron intensity for various material thicknesses as collected by HAADF- and IBF-STEM detectors. The interconnect structure is tilted to 70° to test HAADF- and IBF-STEM image intensities at the highest tilts required for ET. Figure 4.5a) and b) show images of the structure tilted around the vertical image axis. Various structures reverse contrast in the HAADF image, but IBF-STEM provides monotonic image intensities for all points in the image. Arrows overlaid on each image indicate the location of intensity line profiles - plotted in figure 4.6 - measured along the rectangular Cu wire. The wire initially increases in thickness as measured along its length away from the sample edge, but eventually results in a constant projected thickness. Both experimental intensity profiles match predictions from Monte-Carlo (MC) simulations for increasing projected thickness plotted in figure 3.8 and 3.5b). As expected, IBF-STEM provides monotonic image intensities throughout a tilt-series from ±70° for a faithful reconstruction of the interconnect structure.

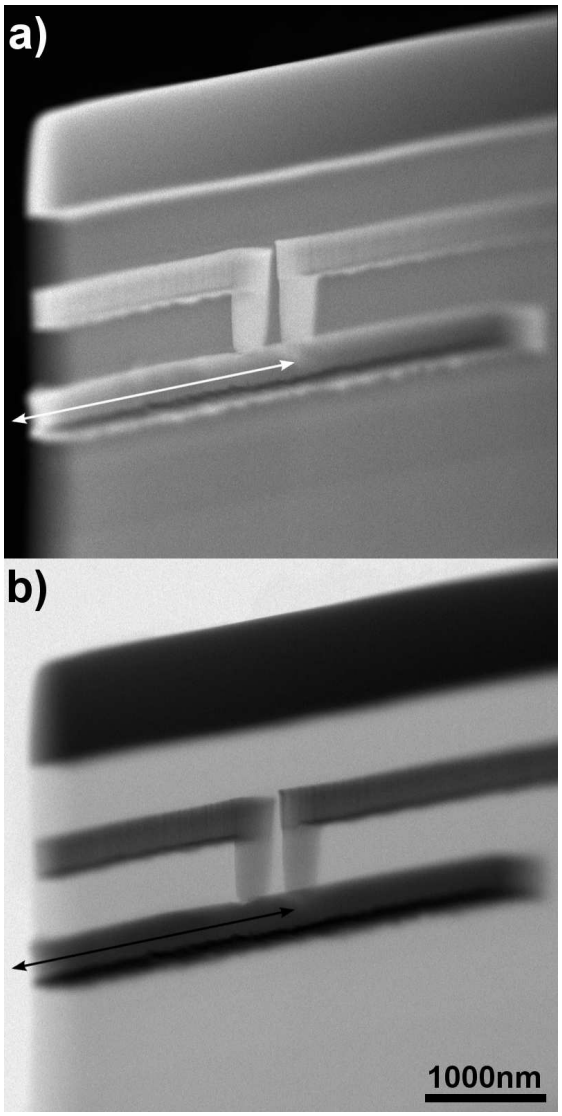


Figure 4.5: STEM images of an ultra-thick cross-section of a Cu interconnect structure tilted to 70° around the vertical image axis. The a) HAADF image exhibits non-monotonic image intensities that reverse contrast along the rectangular Cu wire as its projected thickness increases from the sample's left edge. b) The IBF-STEM image shows monotonic image intensities at all points along the wire, which is required to produce a faithful three-dimensional reconstruction by electron tomography. The arrows on each image indicate the location of intensity line profiles plotted in figure 4.6.

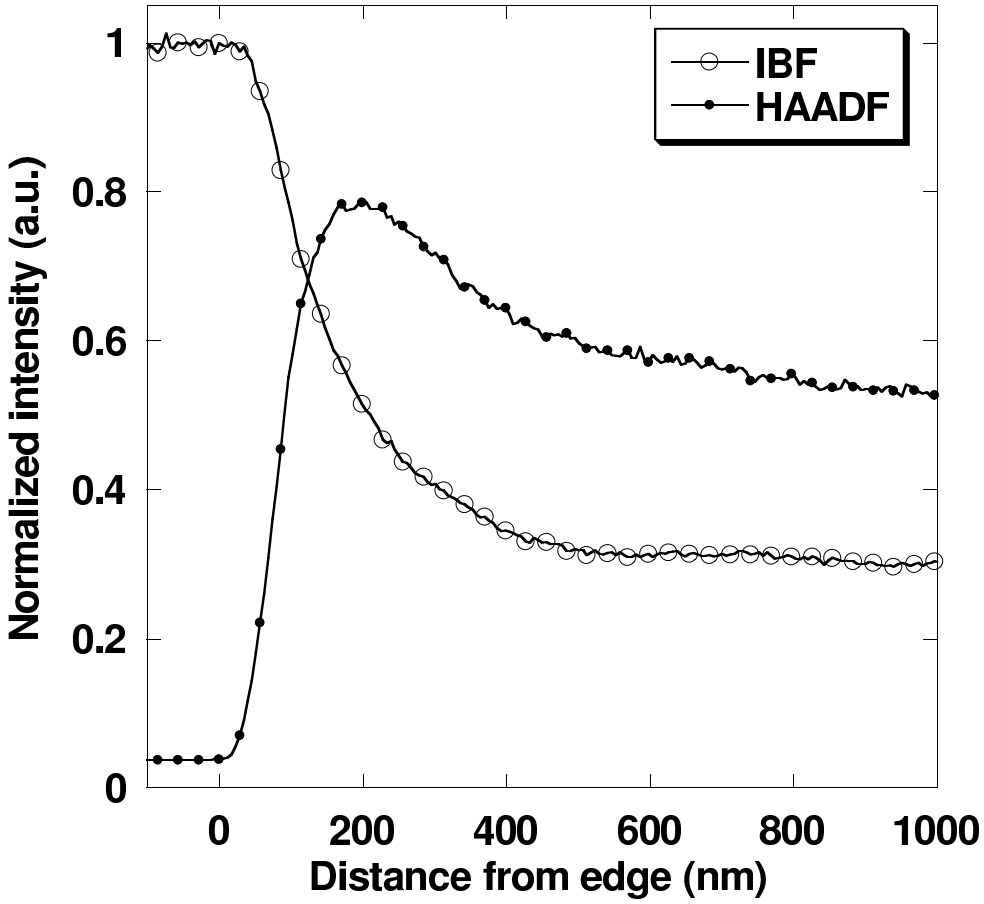


Figure 4.6: Line profiles of HAADF- and IBF-STEM intensities measured along a rectangular Cu line tilted to 70° as shown in figure 4.5. The HAADF intensity transmission function is non-monotonic and shows a reversal of contrast as predicted by Monte-Carlo simulations shown in figure 3.5. The monotonic IBF intensity transmission function is monotonic at every point along the wire and varies inversely with projected thickness as predicted by simulations shown in figure 3.8.

## 4.2 Three-Dimensional Reconstruction of Ultra-Thick Cu Interconnect by IBF- and HAADF-STEM Electron Tomography

The previous sections motivated use of the IBF-STEM technique to produce an accurate three-dimensional reconstruction of highly-scattering materials contained in an ultra-thick TEM cross-section. Therefore to test IBF's suitability to tomography, a series of projection images of the ultra-thick cross-section were acquired at increments of 2° from ±70° using both the HAADF- and IBF-STEM imaging techniques. Figure 4.7 shows 0° tilt projection images acquired by both imaging techniques which show the specific portion of the structure included in the reconstruction. A black arrow overlayed on the HAADF image marks a void-like artifact produced by contrast reversal as mentioned previously (see figure 4.3). Both STEM tilt-series' consist of 70 images aligned by automatic cross-correlation and manual shifting methods using IDL 6.1 [87]. The three-dimensional reconstruction was produced by the simultaneous iterative reconstruction technique (SIRT) with 30 iterations (discussed in section 1.5.3 and [78]) implemented in IDL 6.1.[1]

### 4.2.1 Resolution of the Reconstruction

Resolution of the final reconstruction is estimated by equations 1.3 and 1.4 from section 1.5.4. The tilt axis is the vertical image axis (the y-axis) in figure 4.7 and exhibits resolution limited by the original experimental resolution of the projection images: 0.96 nm/pixel. According to the tilt-series parameters given earlier, the estimated resolution of the 280nm wide interconnects along the x-axis (perpendicular to the tilt axis) and the

[1] Appendix A is a tutorial outlining the details of tilt-series acquisition, alignment and reconstruction necessary to produce high-quality three-dimensional reconstructions. Manual methods are emphasized to obtain the best possible results.

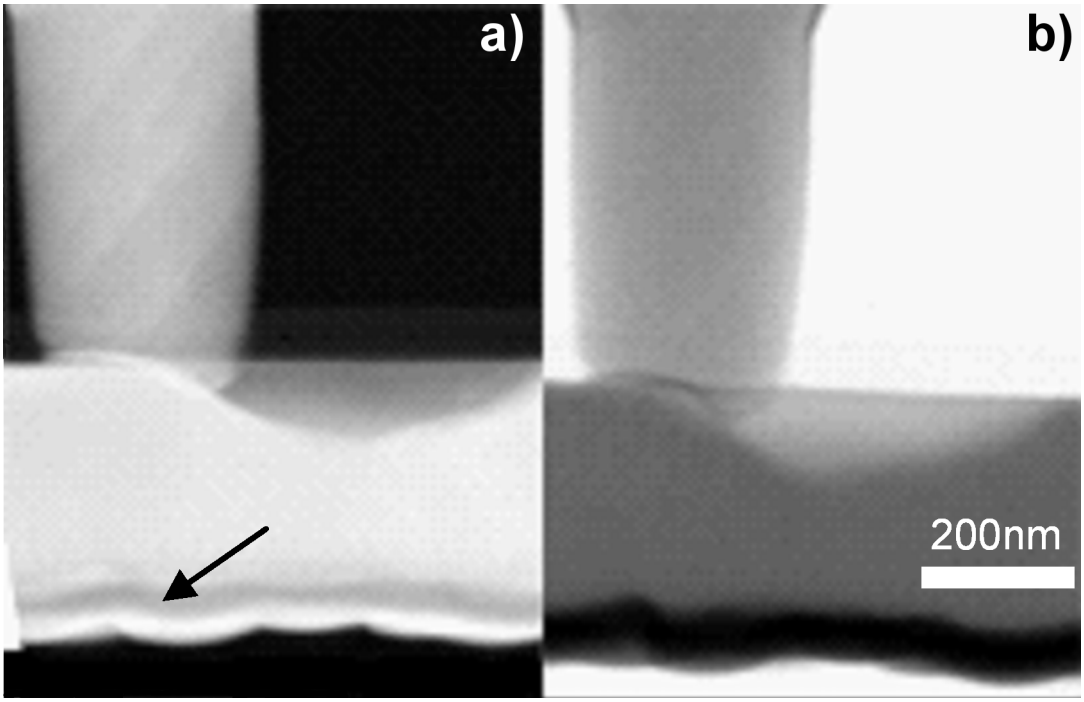


Figure 4.7: a) The original HAADF two-dimensional projection image at 0° tilt shows both the real stress void and second void-like artifact at the bottom of the Cu interconnect (labeled with a black arrow) created by contrast reversal of the Ta liner. b) The original two-dimensional IBF projection image of the interconnect showing the stress void, but the contrast reversal artifact is eliminated. Both projection images, a) and b), suggest that the interconnect possibly undercuts the via, but three-dimensional analysis is necessary to determine the void's precise location.

z-axis (projection direction) are 12nm and 16nm respectively. The tilt increment could be lowered to 1° resulting in $\sim 2\times$ better resolution, but analysis of such large features will not significantly benefit from the improved resolution compared to the additional time necessary to acquire, align and reconstruct all 140 images.

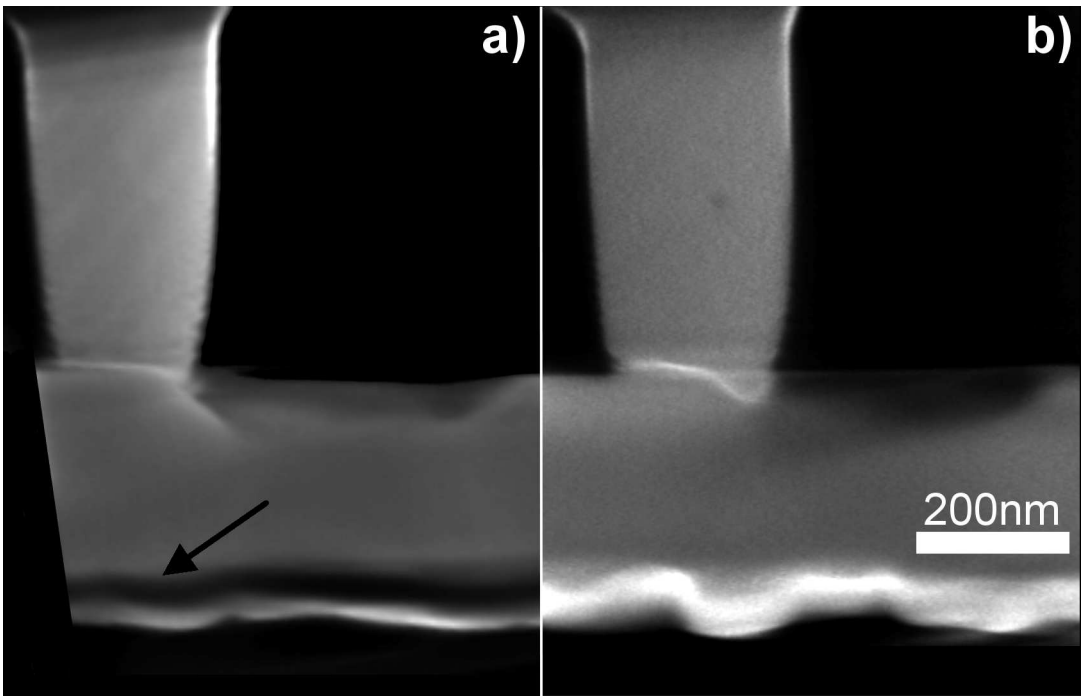


Figure 4.8: a) A 2nm thick slice from the HAADF three-dimensional reconstruction shows that the artificial void persists in the reconstructed data. b) A slice of the IBF three-dimensional reconstruction with inverted image intensities for comparison with HAADF. Only the true void is present in this slice.

### 4.2.2 Quantitative Three-Dimensional Analysis

Figure 4.8 compares 2nm thick slices from the reconstructions produced from each imaging technique. The Ta liner at the base of the bottom pad is washed out in the HAADF reconstruction and a large void (marked with a black arrow) is shown between the Ta liner and Cu pad. The void is a reconstruction artifact that was included in the reconstruction due to contrast reversal artifacts in the original tilt-series images seen in figure 4.7a). The IBF reconstruction, shown with inverted image intensities for easy comparison with the HAADF, shows no artifacts and well defined features.

Figure 4.9a) shows the thresholded HAADF reconstruction which should map the Cu surface, but a slice through the reconstruction reveals an artificial void at the Cu/Ta interface. The reconstruction produces a poor visualization of the stress void as expected from equation (3.16), which determines the suitable STEM imaging technique for a given material thickness as discussed in section 3.4. $t_{1/2}$ is only 120nm for Cu, less than half the Cu interconnect thickness, indicating IBF provides superior image SNR. The IBF images produce an artifact-free reconstruction with better defined features showing the precise location and size of the stress void. The cutaway of the thresholded IBF reconstruction in figure 4.9b) shows no contrast reversal artifacts.

Projection images, as in figure 4.7, suggest that the stress void partially interrupts the via's connection to the Cu pad, but the IBF reconstruction in figure 4.9b) clearly shows this does not occur. Also, facets in the stress void are visible in three directions, which may have implications for its method of formation. Finally, a process known as segmentation (see appendix A) was used to define the void's three-dimensional boundaries in every 3.9nm slice of the reconstruction, from which the volume is calculated: $(210\text{nm})^3$.

## 4.3 Conclusions

The emergence of smaller and denser devices in microelectronics will necessitate the application of ET for a complete understanding of their three-dimensional structure. The IBF technique allows for reconstructions without the mass-thickness and diffraction artifacts that make HAADF and conventional TEM unreliable for tomography of thick sections. MC simulations suggest it is possible to investigate samples in excess of 1$\mu$m with STEM, and we reconstruct a 500nm thick cross-section containing 280nm wide Cu

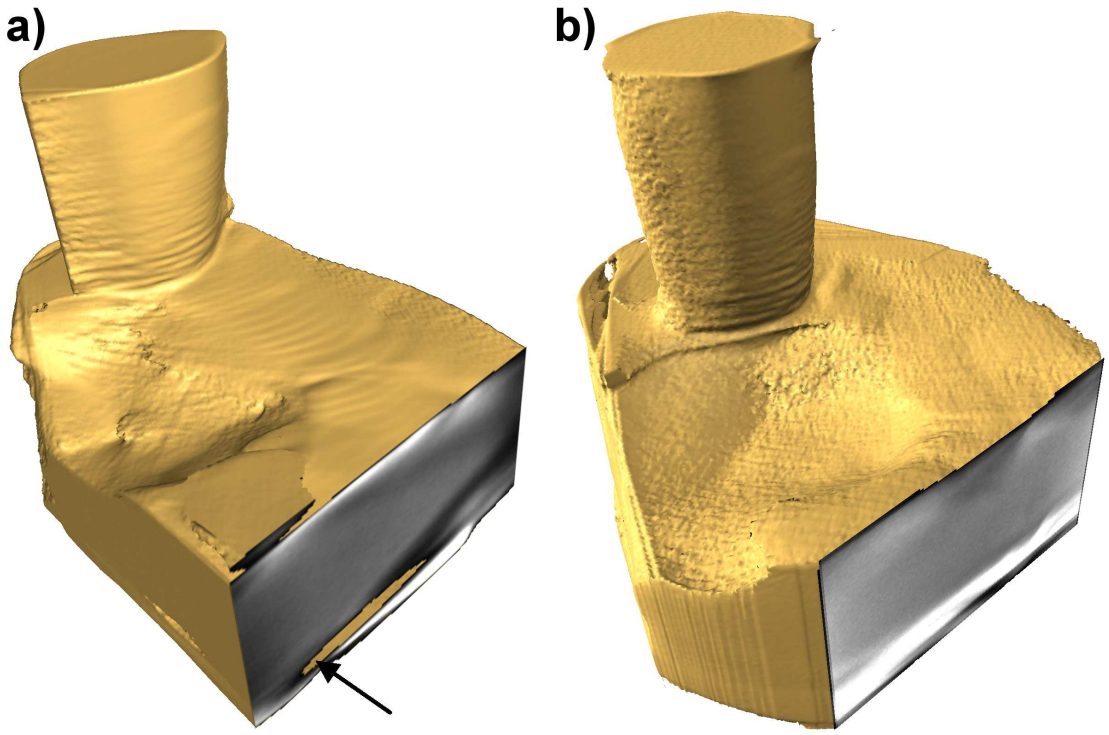


Figure 4.9: a) The thresholded HAADF reconstruction, which should map the copper surface, shows an artificial void at the lower Cu/Ta interface due to contrast reversal in the original projection images. f) The thresholded IBF reconstruction correctly maps the interconnect surface and also shows the stress void is faceted near the via-to-wire junction. The round vertical via is 280nm thick indicating the scale of other features.

interconnects. Possible applications of IBF-STEM tomography include multi-layered integrated circuit interconnects, electromigration barriers, void structures, and metallic particles.

CHAPTER 5

# CONCLUSIONS

## 5.1 Summary

The success or failure of modern microelectronic devices depends on defects at the one-nanometer scale and below in devices 10 – 50nm in size. Scanning transmission electron microscopes (STEM) offer sub-nanometer lateral resolution for imaging and analysis but only produce a two-dimensional projection through the thickness of a specimen. Electron tomography (ET) extracts the lost information in the projection direction from a series of STEM projection images to produce a quantitative three-dimensional reconstruction of the original structure with 1 – 2nm resolution. We applied ET to directly measure nanoscale features buried inside ultra-thick cross-sections of semiconductor devices, which provides accurate predictions of device performance and reliability.

Chapter 1 introduced the equipment, techniques and general problems associated with microelectronic fabrication and metrology of metal interconnections between transistors. Improved processor performance and reliability resulted from replacing Al with lower resistivity Cu by the dual-Damascene process, but also introduced new challenges. Resistivity unexpectedly increases for scaled interconnects, threatening the main advantage of Cu metallization, while Cu electromigration and stressmigration produce voids significantly lowering the mean time to interconnect failure. Nanometer scale analysis of interconnect structures in three-dimensions is necessary to fully understand the effects of these defects on device performance.

Scanning electron microscopes (SEM) traditionally image and analyze defects in integrated circuits (IC) but are incapable of resolving the smallest relevant features in

modern devices. Transmission electron microscopes (TEM) provide the necessary lateral resolution for specimens 10 – 50nm thick but only provide two-dimensional projections of the investigated structure. ET produces a three-dimensional representation of the original structure from a series of projection images with the requirement that image intensities vary monotonically with the structure's projected mass-thickness at every tilt. Traditional coherent imaging techniques - such as conventional TEM (CTEM) and bright field (BF) STEM - are dominated by phase and diffraction conditions within the specimen, which are not directly interpretable. Instead, annular dark field (ADF) STEM provides incoherent *Z*-contrast in images capable of differentiating materials according to image intensity. Thus, ADF-STEM imaging is used to reconstruct thin cross-sections of crystalline materials commonly found in IC devices in three-dimensions.

In Chapter 2, we report a systematic study of the effect of line edge roughness (LER) on the apparent cross-sectional area of 90nm Cu wires with a TaN/Ta barrier measured by conventional ADF-STEM two-dimensional projection imaging and three-dimensional ET. The roughness exhibits defects along the wires' length with a spatial frequency of ~100nm, and a single projection image of the defect prone structure poorly estimates the overall wire cross-sectional area. Proper statistical sampling from projections requires preparation and measurement of many cross-sections to determine the average Cu cross-sectional area - a time consuming endeavor. The time and effort necessary to acquire, align and reconstruct a tilt series for ET is significant but allows for many measurements along the entire wire section contained within the TEM specimen, thus efficiently sampling an extended portion of the LER.

Our measurements of Cu cross-sectional area (a critical parameter needed to calculate wire resistivity) made by projection images and tomography show a 5% discrepancy, which significantly impacts the calculated resistivity for this particular wire. Projection

images are biased to low cross-sectional area measurements due to the overlap of LER defects along the wire's length. It was further shown that measurements by two- and three-dimensional techniques converge for wire cross-sections <50nm thick (for this particular wire), half the defect spatial frequency. Nanoscale size variations increasingly contribute to device performance degradation as dimensions are further scaled; full analysis of current/future devices requires quantitative three-dimensional imaging techniques to predict their performance.

A structure's size has little effect on the considerable time required to produce a high-quality reconstruction. Thus, ET is most efficiently used to investigate large structures contained within an ultra-thick TEM specimen, but traditional TEM techniques are unsuited to imaging thick sections of dense, crystalline materials with directly interpretable contrast at many different tilting angles. In chapter 3, we use a custom Monte-Carlo (MC) electron scattering program to quantitatively model the interaction between an electron beam and a solid - specifically for large thicknesses. Attainable resolution for such thick cross-sections is a major concern and is typically estimated by the radius that contains 90% of incident electrons after scattering through a given material thickness ($R_{90\%} \propto t^{3/2}$). This measure is overly pessimistic due to relatively few electrons scattered far outside the central beam. The measured full-width-at-half-maximum (FWHM) of a buried feature exhibits up to 5× better resolution, indicating image resolution can be maintained even in ultra-thick material cross-sections up to ~1$\mu$m.

We further simulated the transmitted electron intensity collected by STEM detectors with various configurations to investigate contrast reversals for many thicknesses of different materials. Problems occur for ADF-STEM when thick cross-sections containing high mass-thickness materials scatter a majority of electrons beyond the ADF detector's outer collection range (backscatter is an extreme example). This lost signal appears as

a contrast reversal where highly-scattering objects that should appear intensely bright in an ADF image as instead dark. Hence, discerning whether voids in an image are due to missing material or image artifacts is difficult, which challenges the validity of $Z$-contrast for material differentiation in images and reconstructions. The high tilts required by ET can increase projected material thickness by up to 3×, which exacerbates this effect.

All incident STEM electrons must exit the specimen by transmission or backscatter. Therefore, contrast reversals could be avoided by collecting all highly-scattered electrons, but this impossibly requires a detector that completely encompasses the specimen. Instead, we propose collecting the complement of the ADF signal in the form of the forward-scattered electrons contained in the STEM bright field (BF) signal. BF-STEM (0 – 10mrad) is typically dominated by coherent image contrast unsuited to ET, but the BF signal is made incoherent by increasing the outer detector angle up to 100mrad. Our MC simulations predict that the novel incoherent bright field (IBF) STEM imaging technique produces monotonic image contrast for all material thicknesses and provides information complementary to ADF-STEM while avoiding contrast reversal.

The IBF-STEM technique is known as an alternative imaging method to ADF-STEM for specimens likely to reverse contrast, but we compare the expected image quality from both methods for various material thicknesses to illustrate the specific circumstances in which each should be utilized. High signal compared to noise in STEM images provides well defined material feature boundaries for accurate structural measurements. Therefore, MC simulations of signal-to-noise ratios (SNR) for various material thicknesses provide a metric for image quality. At low thicknesses, an ADF detector collects relatively few electrons initially exhibiting superior SNR, but this advantage diminishes as increased material thickness enhances electron scattering. The initially

weak IBF signal is dominated by a large noise component from the strong unscattered beam continually incident on the detector, but increased electron scatter beyond the IBF detector leads to simultaneous improvements in detector noise and signal. Evidently, the two imaging techniques demonstrate opposing dependencies of signal and noise on material thickness. The IBF method expectedly yields similar or improved image quality (as measured by the SNR) for thick material sections in addition to dependable monotonic behavior at all thicknesses. IBF SNR is superior to HAADF SNR when 50% of incident electrons scatter beyond the IBF detector, which occurs at a material specific thickness, $t_{1/2}$. The Rutherford scattering cross-section is directly related to $t_{1/2}$, and we provide a general relationship to determine the suitable imaging technique for any given material thickness.

Chapter 4 applies the IBF-STEM imaging technique to image thick cross-sections of highly-scattering, crystalline materials common in microelectonic devices without artifacts. To test IBF's suitablility to ET, we reconstructed a stress-void in a 250nm wide Cu interconnect with TaN/Ta electromigration barrier layers. IBF-STEM image intensities are monotonic at every tilt angle from $\pm 70^{\circ}$, unlike ADF-STEM, for a faithful reconstruction of the original interconnect structure. We determine the stress-void's precise location and size in three-dimensions and show faceting of the void along three distinct surfaces with implications for its growth mechanisms.

Three-dimensional ET is a powerful technique for analyzing structures at the nanometer scale. We introduce the novel IBF-STEM imaging technique as an alternative to HAADF-STEM to reconstruct ultra-thick cross-sections for efficient and accurate measurement of critical dimensions and defects. Denser features in future integrated circuit (IC) devices will necessitate the application of three-dimensional analysis to properly predict their performance and reliability.

## 5.2 Future Work

In this thesis, we applied ET to reconstruct relatively large structures, enabling measurements of nanoscale features to predict the performance and reliability of IC devices. The pixel size of the original STEM projection images sets the best resolution of our reconstructions, but the estimated theoretical resolution limit for ET is 1 – 2nm assuming a discrete number of projections. Also, we used an incomplete tilting scheme (with limited maximum tilt angle) resulting in an anisotropic point spread function (PSF) elongated along the original projection direction due to missing information from high tilts $> 70^{\circ}$. The structures presented in this thesis do not directly show these fundamental limitations, but reconstruction of a material with simple ~1nm features would allow direct experimental determination of resolution and elongation.

Modern low-$\kappa$ dielectrics consist of a silicon-dioxide matrix permeated with a network of pores ~1nm in size, which directly affect the electrical and mechanical properties of the bulk material. Ellipsometric porosimetry provides indirect measurements of nanoscale porosity, but STEM ET is capable of imaging the porous network in real space to directly measure pore size distribution, connectivity and shape. Figure 5.1 shows orthogonal cross-sections approximately 75nm across through a three-dimensional reconstruction of a low-$\kappa$ dielectric material. Differentiation between the pores and the matrix throughout the sampled volume was accomplished by automatic segmentation with thresholding after determination of the average intensity value at the vacuum/dielectric boundary. Figure 5.2 shows the distribution of pore diameters which fits a log-normal distribution with an average of 1.2 – 1.9nm, and 95% of all pores are less than 5.9nm across. An independent measurement of the bulk porosity statistics by ellipsometric porosimetry produced similar results. ET does not resolve pores <1nm, and only gives an upper bound to the average pore size. STEM ET provides adequate resolution and

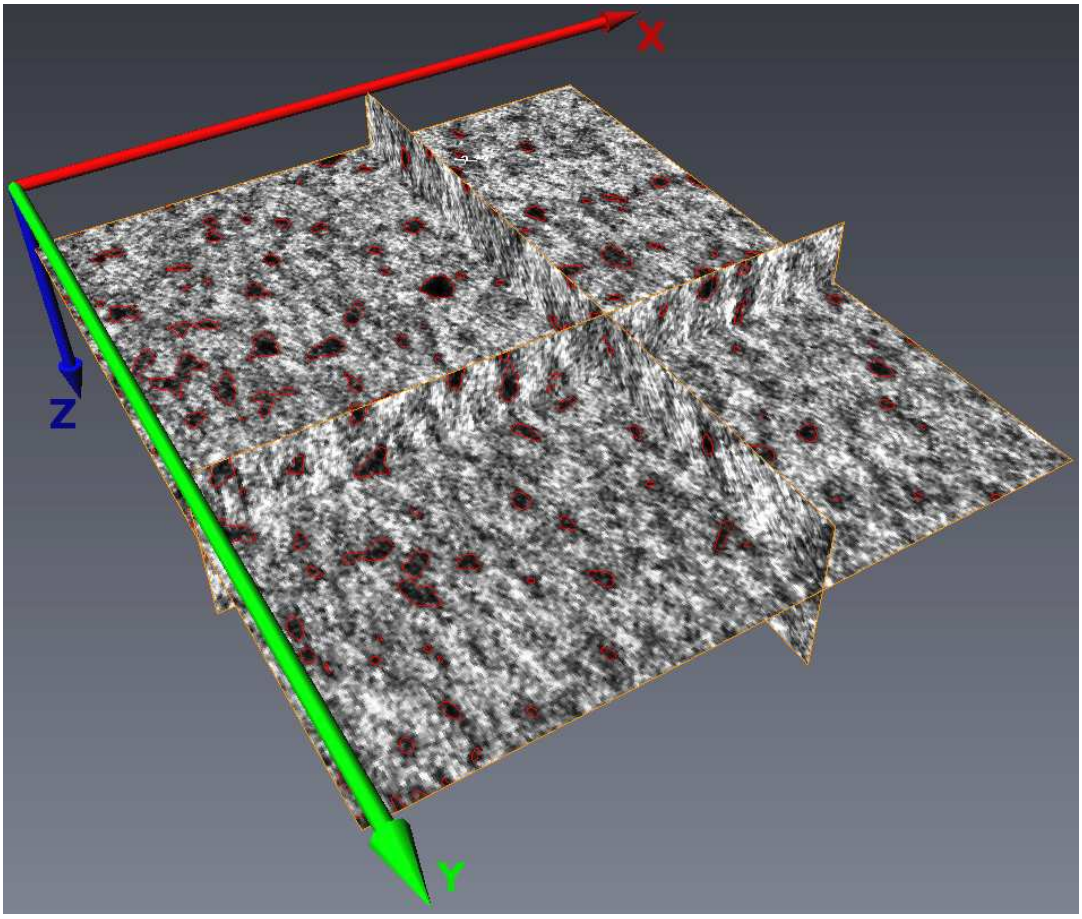


Figure 5.1: Orthogonal slices approximately 75nm across through the three-dimensional reconstruction produced by electron tomography of a porous low-$\kappa$ dielectric showing randomly distributed 1nm pores. The network shows little connectivity for the larger scale porosity and the pore diameters follow a log-normal distribution with an average diameter of 1.2 – 1.9nm. The reconstruction does not resolve pores < 1nm in diameter and therefore only provides information for the larger scale porosity.

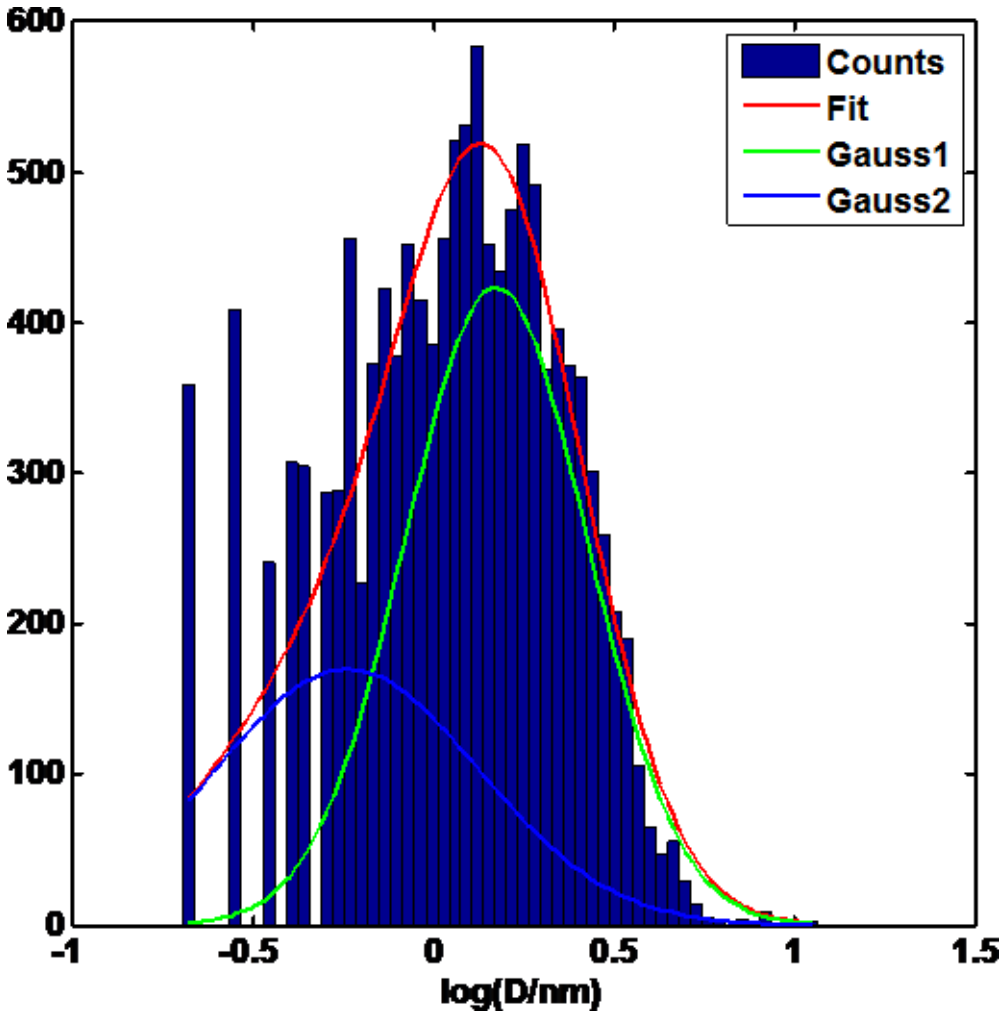


Figure 5.2: Log-normal distribution of the pore diameters for the porous low-$\kappa$ dielectric material as determined by automatic segmentation from an electron tomography reconstruction. The average pore diameter is 1.2 – 1.9nm and 95% of all pores are less than 5.9nm across. The distribution matches independent measurements by ellipsometric porosimetry (not shown).

contrast even for these small, lightly scattering features. Future work will examine a series of low-$\kappa$ dielectric materials with various expected pore parameters to determine how the porous network affects the material's electrical and mechanical behavior.

Next generation electron microscopes include spherical-aberration ($C_s$) correctors for improved spatial resolution and beam current. How do these advances affect electron tomorgaphy? A non-aberration corrected microscope exhibits 1 – 2 Ångstrom resolution laterally and a ~50nm depth of focus, larger than the typical TEM specimen thickness. The entire sample is always in focus, and STEMs produce true projections of the examined structure suitable for ET. $C_s$ correction improves STEM lateral resolution below 1 Ångstrom and depth resolution to the order of 1nm. Thus, $C_s$ corrected microscopes do not provide a simple projection through the thickness of the specimen. The improved depth resolution suggests a new type of three-dimensional imaging sometimes called *depth sectioning*: images are acquired in layers with different STEM defocus values separated by ~1nm to produce a three-dimensional reconstruction. Theory [102] and experiments [103] show that through-focal reconstructions of extended structures suffer from severe elongation along the projection direction similar in magnitude to traditional tilting tomography with a maximum tilting angle of 1-3°. Even so, we propose a hybrid method to acquire a through-focal series at all tilt angles from ±70° separated by 3° increments, which theoretically resolves 1nm features. This technique is required to accomplish ET with a $C_s$ corrected STEM, but needs much fewer tilt angles for nanoscale resolution. Currently, only direct Fourier inversion is used to reconstruct the hybird data. More work is necessary to devise a real-space reconstruction algorithm that avoids interpolation in Fourier space.

APPENDIX A

# ELECTRON TOMOGRAPHY: ALIGNMENT, ACQUISITION AND RECONSTRUCTION

As in all aspects of transmission electron microscopy (TEM), good sample preparation and post-processing is critical for high-resolution electron tomography (ET) results. A typical high-resolution TEM specimen is 20 – 50nm thick to minimize multiple scattering effects. ET requires significant time to acquire, align and reconstruct a tilt-series and is most efficiently used to reconstruct a large portion of a structure contained within an ultra-thick (>> 50nm) TEM specimen. ET resolution is limited to ~1 – 2nm due to errors in tilt-series image registration, the discrete number of projection images, and the maximum tilt-angle achieved. Thus, we tolerate modest beam spreading in an ultra-thick specimen with a minimal impact on the final reconstruction's quality.

Site selective sample preparation is typically accomplished by the *lift-out* technique in a focused ion beam (FIB) [54]. Older FIBs have a fixed electron beam energy (typically 30keV) that creates ~30nm damage layer on any milled surface, but modern FIBs offer low ion beam energies near 2keV to minimize amorphous damage induced in the sample's surface. Thus, we expect little to no structural modification of the sample due to the lift-out procedure in modern FIBs.

Tomographic acquisition, alignment and reconstruction seem like very complex processes, but we will attempt to describe the procedures (and the possible mistakes) at each step. High-quality reconstructions often require manual intervention by the user to ensure every step is accomplished properly. An ideal specimen for automatic computer reconstruction is covered in small Au fiducial markers that provide high contrast features compared to the structures of interest. Existing software packages - such as *IMOD* and FEI's *Inspec 3D* - are specifically written to take advantage of these fiducial

markers, but most solid-state structures consist of high-contrast, repeating features that confuse automatic alignment procedures. We emphasize manual alignment procedures, which, although they may be tedious, provide a good understanding of the tomographic method to avoid problems introduced by automatic alignment procedures.

In this appendix, we first outline preliminary alignment procedures of the scanning transmission electron microscope's (STEM) optics and tilting stage. Then, we discuss the parameters and processes involved with tilt-series data acquisition. Finally, we outline the necessary steps for tilt-series alignment and reconstruction.

## A.1 STEM and Stage Alignment

High-resolution STEM images require a very stable source and detector; thus, we rotate the specimen in the electron beam to acquire a series of images at many different tilt angles. ET reconstruction algorithms require image intensities that vary monotonically with projected thickness throughout a tilt-series and regularly, accurately spaced angular increments ($1 - 2^{\circ}$) between projection images. A high-tilt single-axis tomography holder capable of $\pm 80^{\circ}$ tilt is discussed, although newer holders are capable of full $\pm 90^{\circ}$ rotation.

These calibration procedures are specifically written for the FEI Tecnai F20 with the FEI XPlore 3D version 2.2 tomography acquisition software. A. Voigt and C. Kubel wrote a document - available on the microscope's hard drive - detailing the necessary calibration steps, but their procedure lacks some details. We follow their alignment procedures, adding context and improvements where necessary.

### A.1.1 Align STEM Beam and Scanning Coils Prior to ET Acquisition

A crystal tilted onto a known zone axis provides the best structure to properly align the STEM at high resolution, but high-tilt tomography holders only tilt around one axis. We suggest imaging Si lattice with a normal double-tilt holder before inserting the sample for tomography, which ensures the STEM beam will produce faithful projections without distortions.

The STEM must be properly aligned with the beam traveling straight down the column before the tomography acquisition software is started, and we center the beam on the optical axis with the following procedure. Acquire a STEM image and set a beam marker in the exact center of the image (double click to set x, y to 0, 0). Exit STEM diffraction mode and lower the magnification to find the beam - remove the HAADF detector if necessary. Center the beam on the screen at 100kx with the ”Beam Shift” direct alignment and adjust the objective rotation center with the ”Rotation center (intensity)” direct alignment. Return to diffraction mode and avoid moving/deflecting the beam for any reason. Follow this procedure every time before enabling the STEM tomography software to ensure a consistent STEM alignment and accurate calibrations for every tilt-series acquisition.

### A.1.2 One-time STEM Alignments

The behavior of the microscope during certain actions must be calibrated to allow automatic software control during tilt-series acquisitions. The calibrations listed in the FEI STEM tomography component’s Basic Calibrations are only performed once bar-

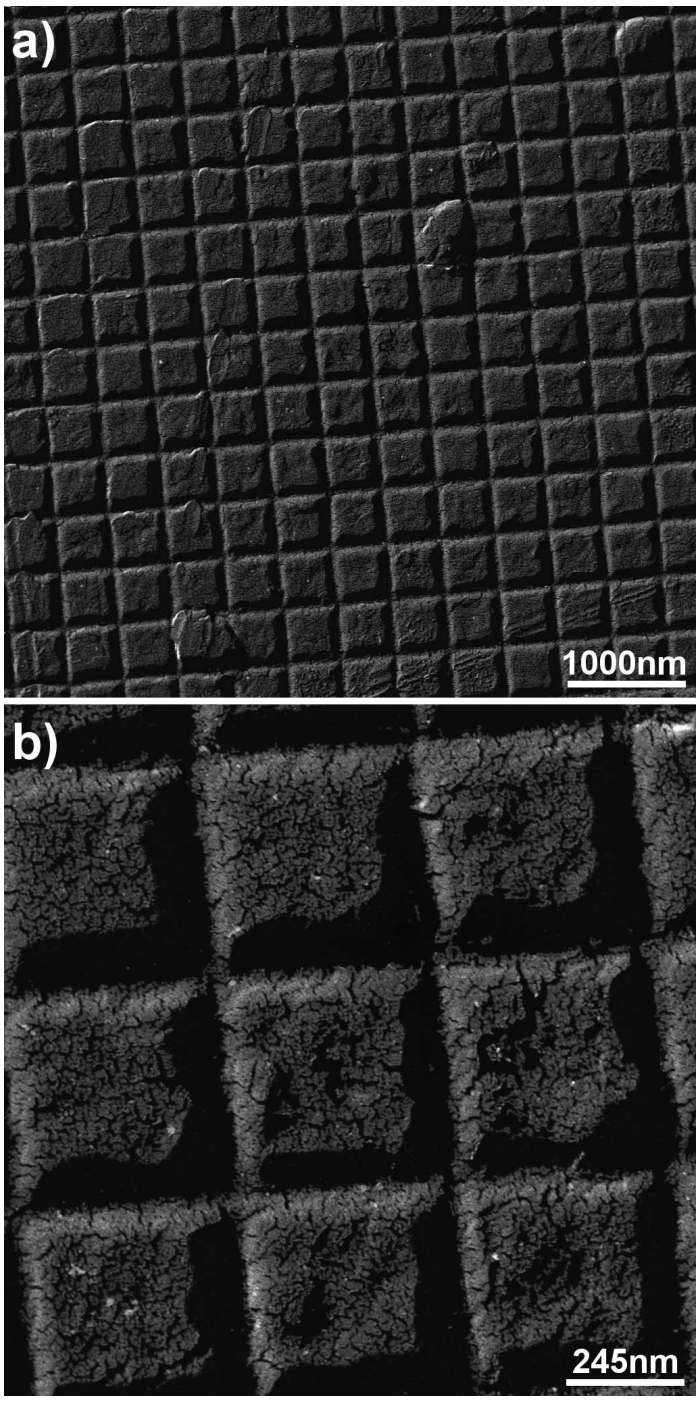


Figure A.1: ADF-STEM images of Au cross-grating sample at a) 20kx magnification and b) 80kx magnification. The grid squares are 463nm apart.

ring major modifications to the STEM scanning system, lens alignments or stage. The standard *cross-grating* sample provides a well-known structure with 2160 lines/mm, or 463nm between grid squares. The grid pattern is produced by evaporating Au onto a carbon film shadowed by a cross-grating and is shown in figure A.1 at two different magnifications. Every image should be carefully focused for the best calibration results.

**STEM Scan Distortion**

The STEM must be properly aligned with the beam traveling straight down the column (see section A.1.1) providing an easily reproducible setup of the microscope. The first calibration mini mizes image distortions produced by the STEM scanning coils. Insert the standard cross-grating sample in any holder and wait for thermal drift to subside. Set the STEM scan rotation to $-90°$, which approximately aligns the stage's tilt-axis to the principal scan direction (the horizontal image axis). A separate program named *scan-distortion.exe* (located in the folder *c:\tecnai\tools*) measures and corrects for scan distortions. Run this program and check the "Use current rotation" option to start with a $-90°$ STEM scan rotation. Set the STEM magnification such that an image contains approximately $13 - 15$ grid squares horizontally. Press "Next" and follow the program's instructions to completion. Close the program after it has finished.

**Magnification Calibration**

Next, run the "Magnification Calibration" procedure (accessible though the STEM tomorgaphy Basic Calibrations) to determine the field-of-view at 20kx STEM magnification using the known distance between grids on the cross-grating sample. This single measurement defines the field-of-view for all other magnifications, affects many

other subsequent calibrations, and allows quantitative measurements of the final three-dimensional reconstructions. The result should be approximately 2.876nm/pixel.

**Stage Shift Calibration and Tilt-Axis Angle Measurement**

The actual distance the microscope shifts the stage is now calibrated with the ”Stage Shift Calibration.” The procedure acquires an image, applies a small stage shift and measures the physical distance the sample moved in a subsequent image by cross-correlation. Put a check mark in the box next to ”Use MCF for shift measurement”, which filters the cross-correlation for improved accuracy. The cross-correlation algorithm may fail to properly measure the shift between the two images due to the cross-grating’s periodic structure. Center a large, unique feature in the image before running this procedure, but the strongly periodic grid pattern often causes this procedure to fail. Instead, use the random micro-structure of the Au, best seen at 115kx STEM magnification, to provide a high-contrast, unique pattern. The ”Stage Shift Calibration” procedure also determines the angle of the microscope’s tilt-axis, which is approximately $-73^\circ$ for the Cornell Tecnai F20. The tomography acquisition software automatically sets the STEM scan rotation to this value when started, and the horizontal image axis throughout a tilt-series will be nearly parallel to the tilt-axis (see section A.3.6 to see why this is important during post-processing). If the scan rotation value changes by $>10^\circ$, repeat the scan distortion, magnification calibration and stage shift calibration to ensure all alignments are accurate.

**Image Shift Calibration**

The software corrects for small shifts during tilt-series acquisition with beam shifts. The actual distance the microscope shifts the beam for a given lens excitation is now calibrated with the ”Image Shift Calibration.” The procedure acquires an image, applies a beam shift and measures the physical distance shifted in a subsequent image with cross-correlation. Again, use the MCF filter option and 115kx STEM magnification for improved results.

**Focus Scale Calibration for Dynamic Focusing**

The STEM beam in the F20 has an ~50nm depth-of-focus. The entire specimen is in focus for low tilt angles, but regions far from the tilt-axis are out of focus at higher tilt angles as shown in figure A.2. The tomography software's dynamic focus feature varies the objective lens' defocus value while the beam rasters across the sample to keep the entire image in focus. The ”Focus Scale Calibration” determines the relationship between objective lens excitation and the microscope defocus in nanometers to determine how the defocus value should change during image acquisition. The procedure changes the stage z-height a known amount (±5$\mu$m for example) and measures the change in defocus necessary to re-focus the sample. Start with a 20$\mu$m calibration step, which will vary the stage z-height by ±10$\mu$m from the current position. The automatic focus feature acquires images at many different defocus values separated by coarse and fine steps and uses auto-correlation to determine the quality of focus. Set the coarse focus step to 1.5$\mu$m and the search cycle (the number of images) to 15 - encompassing a large defocus range to refocus on the sample, which is now 10$\mu$m out of focus. Set the fine focus step to 0.1$\mu$m such that the fine defocus range covers one coarse defocus step. The

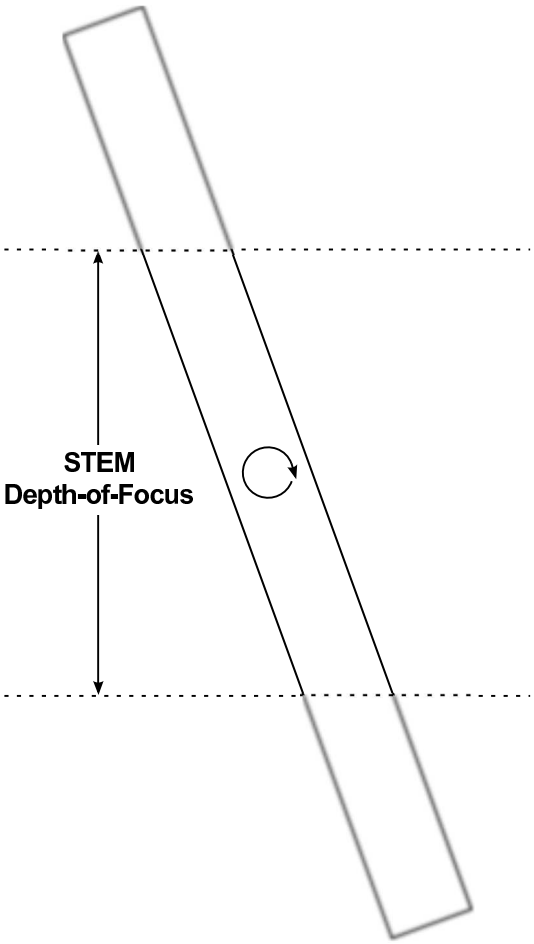


Figure A.2: The STEM has an ~50nm depth of focus. Regions of the sample far from the tilt-axis will be out of focus at high tilt angles. The tomography software's dynamic focusing feature varies the objective focus to keep the entire specimen in focus.

resulting ratio of stage displacement along the z-axis to the defocus necessary to refocus the sample (StageZ / DeltaF") should be approximately −1.335.

Run the "Auto Eucentric Height" procedure in the "STEM Auto Functions" twice to verify this calibration. The measured eucentric height should be constant to within 100nm. Also, acquire an image using the "Adjust Imaging Conditions" procedure with

the dynamic feature enabled of the cross-grating sample titled to 60° and ensure the entire image is in focus.

### A.1.3 Sample Holder Alignments

The entire structure must be in the field-of-view at every tilt angle to acquire as much information about the structure as possible. Each holder interacts differently with the microscope's stage, but the software accounts for these variations before and during a tilt-series acquisition. A holder's exact center will not coincide with the STEM optical axis, and the beam should be shifted to the holder's center. Also, the region of interest shifts predictably during stage tilting, and we measure these shifts allowing the software to apply automatic corrections between image acquisitions. Small random shifts also occur during data acquisitions but are easily corrected by tilt-series alignment procedures during post-processing (see section A.3).

Load a carbon grid covered in 2 – 9nm Au particles, called fiducial marks, and setup the STEM at 80kx magnification. Check that the STEM auto-focus parameters are reasonable for this sample. The FEI instructions suggest enabling only the fine focus settings for the sample holder alignments, which we find risky. The long, tedious "Optimized Position Calibration" procedure fails completely if image focus is not properly determined at any one step. We suggest using a 10$\mu$m course defocus step, 0.1$\mu$m fine step, and 11 image search cycle to ensure the procedure succeeds.

**Optimized Position Calibration**

The optimized position of the beam that coincides with a holder's center is unique for each holder. Note the old optimized position value for comparison with the new result before attempting the "Optimized Position Calibration" procedure. The microscope will vary the beam position numerous times during the procedure, and the user fixes astigmatism and tomo rotation center for each step. Insert the largest $C_2$ aperture (probe forming aperture) to simplify these manual alignments, but recenter the proper $C_2$ aperture (the second smallest aperture) and refocus on the sample when finished. The automatic procedure tilts the sample and determines the focus after each tilt. As mentioned before, we suggest using a 10$\mu$m course defocus step, 0.1$\mu$m fine step, and 11 image search cycle for the automatic focus settings to ensure the procedure succeeds. Press the "Pause" button and manually focus an image between each tilt if necessary, because the procedure fails completely if image focus is not properly determined at any one step. The optimized position varies between holders, but Cornell's Fischione model 2040 tilt-rotate holder currently has an optimized position of $-0.279\mu$m.

**Holder Tilt Alignment**

The region of interest shifts predictably for each holder between tilt increments, and a holder calibration measures these shifts allowing the software to correct for them automatically in subsequent tilt-series acquisitions. First, determine the maximum tilt-angle for both the positive and negative directions at which a region containing many fiducial markers is still visible. Set the STEM magnification to 80kx and run the "Holder Calibration" procedure with the desired parameters. Use a tilt increment of $3-5^\circ$ to expedite the procedure, because the software is capable of interpolating shifts for unmeasured tilt angles. The region of interest may shift far outside the field-of-view during tilting at

high tilt-angles, and the software automatically lowers the tilt increment to the ”high tilt step angle” for all tilt-angles greater than the ”high tilt switch angle.” Disable this feature for well behaved samples/holders by setting the ”high tilt switch angle” to the maximum tilt angle. We exclusively use the continuous acquisition scheme for all tomography data acquisition, which starts acquisition at the maximum negative tilt-angle and continuously acquires images through the entire tilt-range. The alternative ”Start at 0° ” tilt scheme starts at 0° and acquires images continuously through to the maximum negative tilt-angle. The software then returns to 0° and acquires images continuously through to the maximum positive tilt-angle. This allows the software to more easily track the region of interest, but the stage never returns exactly to the same position at 0°. The region of interest is usually lost at the switch from negative to positive tilts, and we observe small - yet significant - rotations in the plane of the specimen difficult to correct during post-processing.

Press the ”Apply” button to set the parameters before starting the acquisition procedure. The holder will incrementally tilt from 0° to the maximum negative tilt-angle while compensating for shifts of the region of interest. Once the region of intereste is centerd at the maximum negative tilt, the procedure continuously tilts to the maximum positive tilt angle. The procedure only begins to save alignments once the maximum negative tilt angle is reached. Thus, a holder calibration requires 50% more time to complete compared to a normal tilt-series acquisition. The holder calibration procedure saves an image at every tilt angle, and the resulting tilt-series provides a data set to check the holder alignemtn and to practice post-processing procedures.

## A.2 Tilt-series Acquisition

The previous ”one-time” alignments enable automatic tilt-series acquisitions with little user intervention for acquisitions at low- to medium-magnifications (< 160kx). The tomography software corrects for all sample shifts with beam shifts, and many little shifts in one direction eventually distort the STEM beam. Beam distortions are less important at low magnifications but must be corrected at higher magnifications (>160kx) to attain 1 – 2nm tomographic resolution.

The following acquisition procedures are specifically written for the FEI Tecnai F20 with the FEI XPlore 3D version 2.2 tomography acquisition software. A. Voigt and C. Kubel wrote a document - available on the microscope’s hard drive - detailing the necessary acquisition steps, but their procedure lacks some details. We supplement their document with additional context and improvements where necessary

### A.2.1 Preparing for Tomography Acquisition

The STEM should be well aligned as in section A.1.1 including beam tilt pivot points and intensity rotation center. Find the maximum allowable (positive and negative) tilt such that the region of interest is visible, and ensure that the HAADF detector camera length and gain do not clip image intensities at any tilt.

#### Image Acquisition Parameters

The user can test the STEM acquisition parameters for specific imaging tasks necessary during tilt-series acquisitions with the ”Adjust Image Conditions” procedure in the

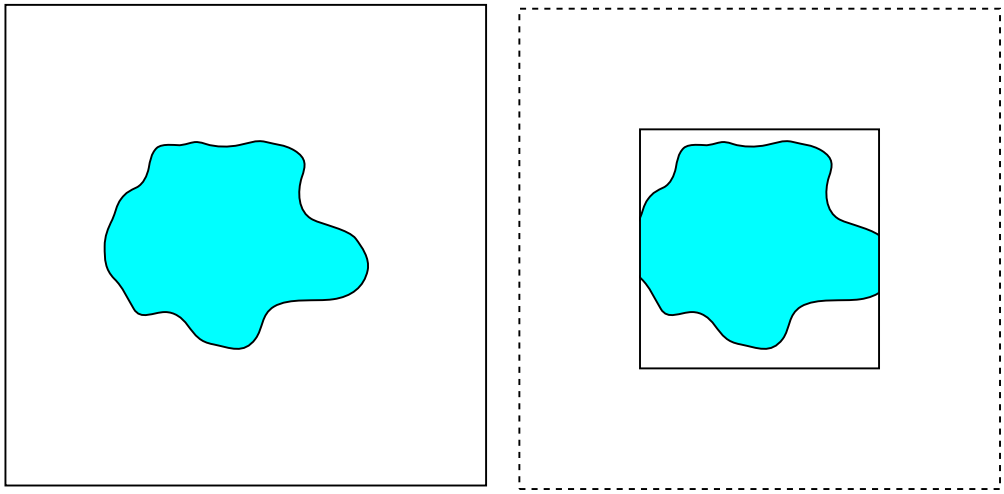

Figure A.3: A diagram showing how the size preset option in tomography acquisition affects the final image. a) The full field-of-view is scanned with $M \times M$ pixels to create an image of the structure. b) The center half of the field-of-view is scanned with the same number of pixels ($M \times M$). Image b) exhibits 2× better resolution than image a).

STEM Auto Functions tomography component. The procedure features four separate acquisition settings: search, focus, exposure and tracking. Each acquisition setting produces a different quality image specifically tailored to accomplish an intended task with minimal acquisition time.

For each setting, the STEM magnification sets the size of the full field-of-view. ”STEM binning” refers to binning with respect to a full $2048 \times 2048$ raster scan, and therefore binning 4 produces an image of the full field-of-view with $512 \times 512$ pixels. Higher binning lowers the image resolution and the acquisition time.

The ”size preset” refers to the central portion of the full field-of-view over which the beam is scanned, which in STEM amounts to additional magnification. For example, the ”Half” setting scans the beam only in the center half of the full field-of-view with the same number of pixels, which results in 2× greater magnification. TIn figure A.3a)

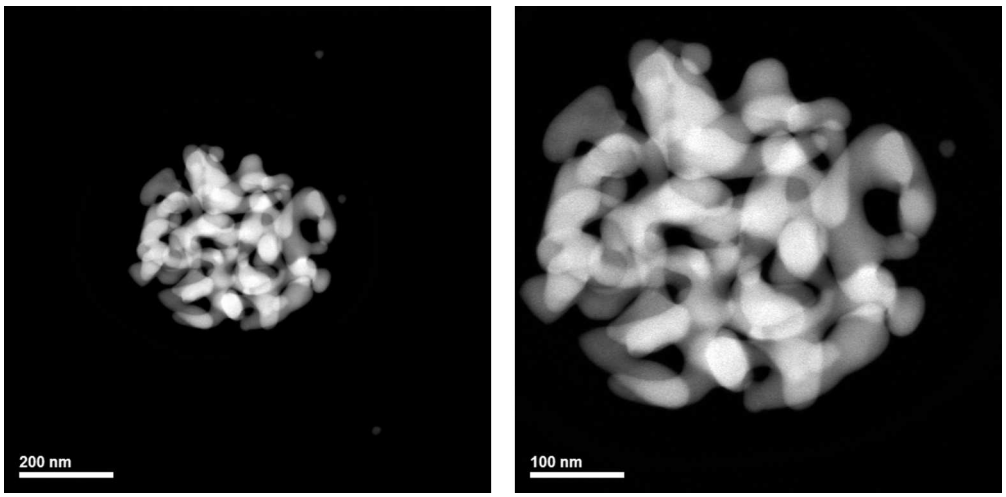


Figure A.4: Two HAADF-STEM images of a porous gold particle acquired with different ”size presets” for electron tomography. a) 512 pixel image scanned over the full field-of-view and b) $512 \times 512$ pixel image scanned over the center half of the full field-of-view. Image b) shows the object at $2\times$ higher magnification that a).

the beam scans over the full field-of-view with the number of pixels set by the ”STEM binning” value, but in figure A.3b) the beam scans over only the center half of the field-of-view with the same number of pixels. Therefore, in image b) the object is sampled at the same number of locations, and the pixel size is one-half that of image a). Figure A.4 shows two experimental HAADF-STEM images, each with $512 \times 512$ pixels, of a porous Au particle. For figure A.4b), the beam was rastered only over the middle half of the full field-of-view shown in figure A.4a), which results in $2\times$ higher magnification. The software (and the user) is capable of focusing an image more accurately at a higher magnification, and we suggest setting the ”size preset” for the STEM Focus acquisition settings to ”Half.”

The four STEM acquisition settings (*search, focus, exposure* and *tracking*) are specifically tailored for efficient tilt-series acquisition. The full field-of-view for ev-

ery STEM acquisition is set by the current STEM magnification. The *search* acquisition settings should produce a fast-raster, low-quality image for near real-time imaging, useful for searching for the region-of-interest if necessary. The *focus* acquisition settings yield a medium-quality image with a low frame time, allowing quick determination of the proper defocus by the automatic focus routine. This routine acquires 10 – 20 images to determine the correct defocus, which adds a substantial amount of time to a tilt-series acquisition. Minimize the STEM *focus* frame time for efficient (faster) tomographic acquisitions. The *exposure* acquisition settings dictate the quality of the actual projection images used in the final reconstruction and should be very high quality. $1024 \times 1024$ images with 20 – 40 second frame times are typical for high-contrast STEM images, but beam damage may limit dwell time per pixel for some samples. The *tracking* acquisition settings should produce images of similar quality to the focus setting and capable of measuring shifts between tilts by cross-correlation. The top-left pixel, bottom-right pixel, frame time and dwell time values change automatically depending on the binning and size preset settings, and should yield sensible results.

**Adjust Filtering**

The software applies a filter before cross-correlating images to improve feature tracking. Proper filter settings enhance feature(s) to be aligned at every tilt-angle and allow the software to automatically center the region-of-interest. A Sobel filter enhances feature edges and is generally useful for high-contrast features. A Hanning window removes intensity at the edge of each image, and the software will only track features in the center. This reduces confusion due to periodic structures but also reduces the field-of-view for tracking such that the region-of-interest may not be visible. The high and

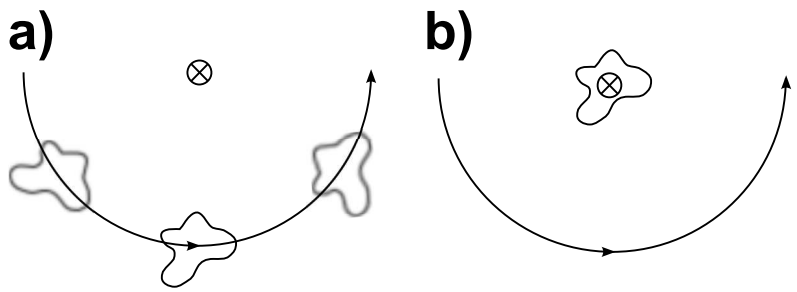


Figure A.5: The diagrams show the movement of an object located at different positions with respect to the holder's eucentric height marked by an ⊗. a) An object located below the eucentric height rotates and shifts when tilted about the eucentric height. b) An object located at the eucentric height does not shift during tilting, which is ideal for tomographic acquisitions.

low cutoff frequencies dampen small and large features respectively. Always click the "Apply" button to set the parameters before testing the image filter.

**Auto Eucentric Height**

With the sample at the eucentric height, sample shifts during tilting are minimized. Figure A.5a) shows an object located below the eucentric height, marked by an ⊗, with the electron beam traveling from top to bottom. The object shifts and rotates when tilted around the eucentric height. Figure A.5b) show the object located exactly at the holder's eucentric height, and it simply rotates - as desired - without any spatial translation. The "Auto Eucentric Height" procedure varies the position of the object along the projection direction and minimizes lateral drift in images at different tilts. Three successive measurements of the eucentric height with ±15° stage tilts should produce values within 100 – 200nm.

**Auto Focus**

Adjust the auto focus parameters to quickly determine focus after each tilting step. These values cannot be changed once acquisition has begun. Enable only the fine search feature to significantly reduce the total tilt-series acquisition time. With coarse search disabled, automatic focusing may fail for some tilts, and the user must manually focus the image. Set the coarse defocus to 1 – 3$\mu$m, the fine focus to 0.5$\mu$m, and search cycle to 6 – 11 images, but these parameters vary depending on the sample and its thickness. Review section A.1.2 for a description of these parameters.

**Exposure Image Parameters**

Exposure images are the projection images of the region-of-interest used for alignment and three-dimensional reconstruction. Check that the parameters chosen in section A.2.1 produce best-quality images even at high tilt-angles. The dynamic focus feature should keep the entire region-of-interest (not necessarily the entire image) in focus, and the image intensity levels must fit within the total allowable intensity range of the detector (do not clip the image intensities). Be sure to account for the generally higher HAADF-STEM image intensities at higher tilts due to 3× increase in projected thickness at ±70° tilt-angles.

### A.2.2 Automatic Tilt-series Acquisition

All calibrations and image acquisition parameters for tomography are now set properly. Start the STEM Tomography component and select the ”Acquire Tilt Series” procedure. The tilt-series parameters are now shown in a single window. Set the negative and posi-

tive maximum tilt-angles, choose the ”continuous tilting” scheme and use 2 seconds for the stage relaxation time between tilts. Set the ”partial tilt angle” to the maximum negative tilt angle. This option allows the user to acquire a partial tilt-series starting at any tilt angle, but we want to acquire a complete series. Select the linear tilt scheme, 1° or 2° increments at low tilts, the desired high-tilt switch angle and the desired tilt increment for high tilts. The high-tilt increment should be less than the low-tilt increment for better feature tracking, but we usually use the same tilt increment throughout an acquisition.

All acquisition data is saved in a single MRC file in the desired directory with the desired name. The software saves each exposure image after acquisition, and the accumulated data is readable even if an interruption aborts the acquisition. So, all previously acquired tilt-series images are available if the acquisition aborts before the the maximum positive tilt angle is achieved.

Manually set the eucentric height and focus at the region-of-interest, and disable the ”Start at eucentric height” and ”Start with auto focus” features. The holder calibration file contains corrections for lateral shifts ($X$ and $Y$) and shifts along the projection direction ($Z$). The software applies XYZ, XY or no corrections with beam shifts, and we suggest applying only $X$ and $Y$ shifts. The automatic focus procedure corrects for shifts along the $Z$-axis. All shifts are corrected with beam shifts, and the stage should not be physically moved to keep all calibrations consistent.

The software can automatically correct the focus before image exposure acquisitions, but the frequency of automatic focus correction is variable. Acquisitions at low magnifications require fewer focus corrections compared to acquisitions at higher magnifications. Set the frequency to 1 – 2 for the best results but a longer overall acquisition time.

Set both the ”applied defocus (at 0° tilt)” and ”shift focus area” to 0. These options are not used.

The software automatically centers the region-of-interest after and/or before each image exposure acquisition. Only allow tracking before acquisitions, if at all. The holder calibration measurements keep the region-of-interest centered within reason after each tilt, and small shifts are corrected during post-processing alignment as discussed in the section A.3. The user may enable manual tracking at any time to correct for large shifting errors with beam shifts.

Press the ”Apply” button to set all parameters and the ”Proceed” button to begin an acquisition. For the continuous tilting scheme, the microscope immediately begins tilting to the maximum negative tilt-angle. Quickly lower the STEM magnification and press the STEM ”Search” button in TIA to observe the specimen rotate, and manually center the region-of-interest with the stage track-ball while the stage tilts. Objects look very different at $-70°$, and the region-of-interest may be difficult to identify after the microscope finishes tilting. Press the ”Proceed” button once the region-of-interest is properly centered at the maximum negative tilt-angle. This is the last time the stage should be physically moved.

Automatic focusing and tracking are most difficult at large tilt-angles. Ensure the software properly images and tracks the specimen for the first few exposures and intervene if necessary by placing a check mark next to the ”Manual...” option of choice. Automatic acquisition procedures yield higher success rates at lower tilt-angles.

I possible, keep track of overall sample shifts in any one direction during the whole acquisition process, because large beam shift corrections applied by the software can lead to astigmatism and other STEM lens misalignments. Dynamic focus especially

relies on accurate rotation center alignments to avoid image distortions. Periodically pause the titl-series acquisition and check these alignments (astigmatism and rotation center) to minimize image distortions.

### A.2.3 Manual Tilt-series Acquisition

Successful tilt-series acquisitions at high-resolution often necessitate tedious manual intervention. Also, the user often focuses and tracks the region-of-interest more quickly than automatic routines, which can limit the object's radiation exposure. The software may lose a small region-of-interest between every tilt. Thus if necessary, disable all holder calibration corrections (X, Y and Z), use manual tracking before and manual focusing. Further avoid beam distortions due to beam shifts by instead moving the stage to track the region-of-interest. Use the software to tilt accurately and organize the data in an MRC file for simplified post-processing. Tedious manual tilt-series acquisition is necessary for successful reconstruction of radiation sensitive materials and/or small objects.

## A.3 Tilt-series Alignment Procedures

Tilt-series alignment removes all shifts of the region-of-interest between projection images introduced during acquisition. Improper alignment yields reconstructions that may, at first glance, appear correct but in fact contain numerous artifacts. Automated alignment procedures generally succeed for low-contrast biological specimens covered in fiducial markers (1 – 10$\mu$m Au particles) but usually fail for high-contrast and/or peri-

odic features. Manual alignment procedures - though tedious - produce superior results, and we outline the necessary steps in this section.

### A.3.1 IDL Scripts

We will describe scripts originally developed by Matthew Weyland [87] with updates by Peter Ercius and Huolin Xin. The scripts were written for RSI IDL 6.1 or lower, and some known compatibility issues exist with IDL version 7. Any text editor is capable of reading the scripts' source code. Future work should involve porting these scripts to the current software.

Comments included in each script describe its general function. We encourage new users to familiarize themselves with IDL and the scripts' source code for a better understanding of the alignment process. Blind application of alignment procedures without attention to details usually produces low-quality reconstructions unsuited to quantitative investigations of the original structure.

#### IDL Language Syntax and Properties

Each script has the file extension *.PRO*, which are readable with any standard text editor. The scripts are essentially a list of commands executed by IDL sequentially. IDL is not a case-sensitive language, and therefore the command $a = 1$ is equivalent to $A = 1$. Many commands and/or scripts in IDL have required and optional inputs. All optional inputs are denoted by brackets [ ] in the following SYNTAX descriptions. IDL commands also have *KEYWORDS* that allow the user to optionally pass scalars or arrays to the script.

*KEYWORDS* must be in all capital letters and followed by an equals sign (=). Array numbering starts at 0 in IDL.

### A.3.2 Saving data

We recommend saving the IDL *session* often to avoid any data loss. The built-in **SAVE** command saves all variables currently stored by IDL in memory to a single file on the hard disk.

SYNTAX: SAVE, FILENAME=*StringFileName*

The built-in **RESTORE** command loads all data in a file into memory.

SYNTAX: RESTORE, *StringFileName*

The **RESTORE** command will import all varaibles to IDL exactly as they were saved. Thus, one can easily backup and restore all work acomplished in IDL.

### A.3.3 Sample Tilt-series

We use a tilt-series of a porous Au particle supported on a thin SiN window to demonstrate correct (and incorrect) alignment procedures. The large particle exhibits well-defined features for easy alignment, but its full structure is not easily determined from two-dimensional projection images. Figure A.7 shows a HAADF-STEM image of the particle at 0° tilt for reference. The original tilt-series images are $1024 \times 1024$ pixels.

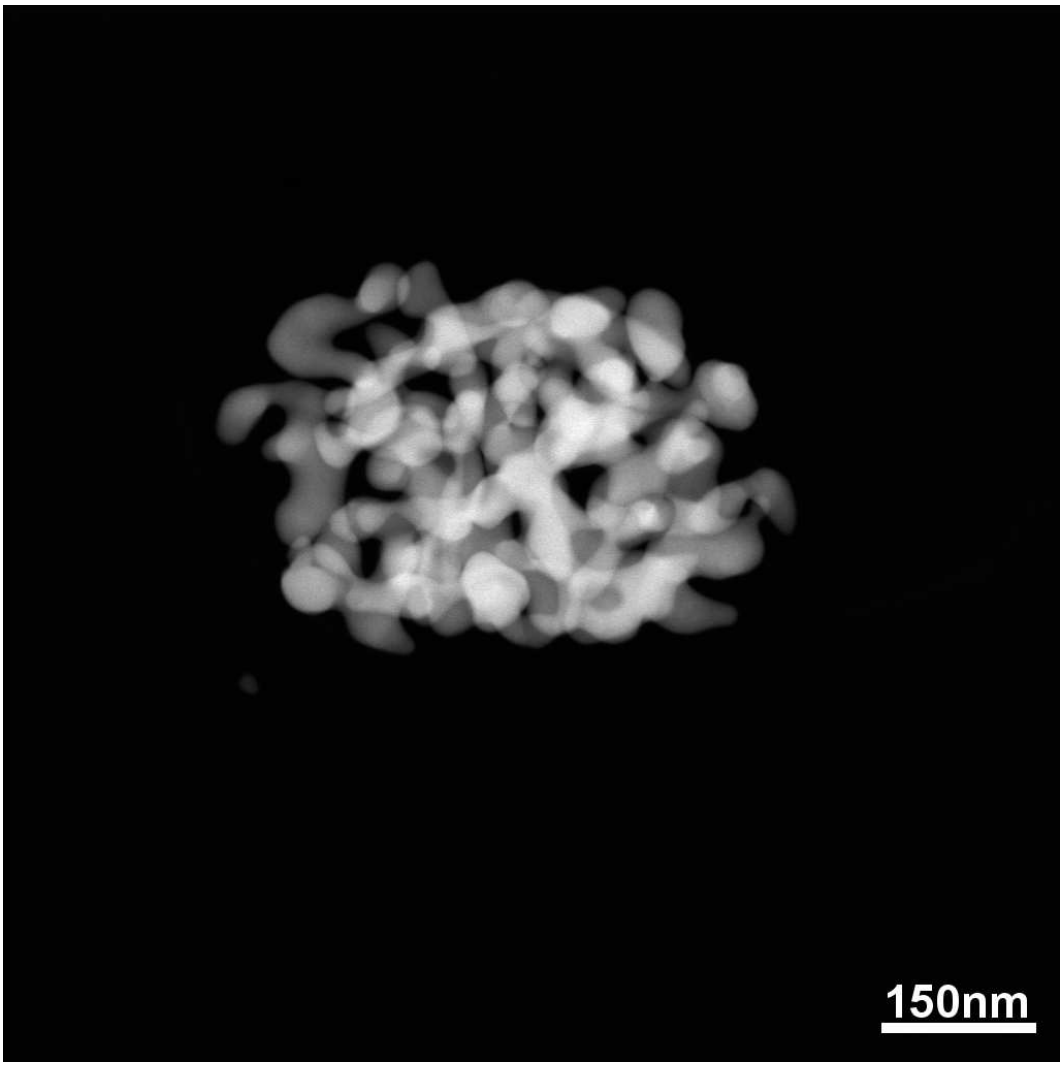


Figure A.6: HAADF-STEM image of the full field-of-view of a porous Au particle at 0° tilt at 115kx magnification. The large particle exhibits well-defined features for easy alignment, but its full structure is not easily determined from two-dimensional projection images.

### A.3.4 Import Data into IDL

FEI's *Xplore 3D* tomography acquisition software creates four files for each tilt-series acquisition. The file with the *.RAWTLT* extension contains a list of all tilt-angles. The file with the *.TXT* extension holds all parameters for the tilt-series acquisition including maximum tilt-angles, binning, applied corrections and many more parameters. The *_shifts.TXT* file contains all X, Y and defocus shifts applied during acquisition. These three files are read with any standard text editor. The file with the *.MRC* extension contains the STEM magnification, number of image pixels, actual pixel size in nanometers, full field-of-view and all exposure images encoded as binary data.

The IDL script named **MRC.PRO** reads the binary data in an *MRC* data file into memory as a named array:

SYNTAX: MRC, *ArrayName*, [SUB = *Scalar*], [SHIFTS = *ArrayName*]

The script asks the user to "Enter final image size (nxn)", which determines the image binning. Initially, bin the images by a factor of 2 or 4 smaller to create a data cube occupying less memory, which speeds up data processing for initial rough estimates of spatial alignment. Final alignments on unbinned images produce the best results, and binning images to sizes larger than native resolution allows sub-pixel alignments. The image binning occurs after shift alignments are applied. The SUB keyword allows the user to specify the size of a central region to clip from each image. Image clipping occurs before rebinning but after shift alignments are applied. For example, set SUB = 512 to select only the central $512 \times 512$ pixels of each image. The SHIFTS keyword allows the user to apply a series of shifts from a separate data array. Shift arrays have size [n,2] where n is the number of images, and array entries specify the number of pixels to shift along the vertical and horizontal directions for each image. **MRC.PRO** applies shifts

before binning. We include two example commands (in bold) and a description of the results:

**mrc, ser** - use final image size of 256, 512 or 1024 for 4×, 2× or no binning respectively.

**mrc, ser, SUB = 512** - The script clips all image data outside the center $512 \times 512$ portion of the full field-of-view. Use final image size of 256 or 512 for 2× or no binning respectively.

Check that all image intensities in the data cube are positive after the **MRC.PRO** script finishes. IDL may incorrectly import data as **signed integers** ($-32,768$ to $+32,767$), but the original data is formated as **unsigned integers** (0 to $65,535$). Simply subtract the minimum integer value from all array values to produce an all-positive array.

### Define Tilt Angles

Some alignment scripts require an array of size [n,1] containing the tilt-angle associated with each image. The following IDL command produces an array of integer values from $-70^\circ$ to $+70^\circ$ with $2^\circ$ tilt increments:

**angles = findgen(70)*2 - 70**

### Tilt-series Inspection

The tilt-series data cube has size (n, M, M) where n is the number of tilt images and M is the image size in pixels. The built-in function **TVSCL** displays two-dimensional arrays as images on the screen with scaled image intensities. This function is very basic, and a custom script named **IM.PRO** produces better formatted images. For example,

the command **im, ser(0,*,*)** displays the first image in the tilt-series at the maximum negative tilt.

SYNTAX: TVSCL, *ArrayName*

SYNTAX: IM, *ArrayName*

Each two-dimensional slice of the data can be shown sequentially along any axis of the data cube with the **MOVIEF.pro** script. The script prompts the user to choose a direction, which indicates the array index to cycle through. For example, enter 1 to show each tilt-series image in succession - similar to a movie. The second optional input controls delay time between images and has a default value of 1. Press ”q” at any time to stop the movie.

SYNTAX: MOVIEF, *ArrayName*, [*Scalar*]

The **CLICKMOVIE.PRO** script provides image-by-image inspection of the tilt-series controlled by the user. The left-mouse button advances the tilt-series to the next image ($n + 1$) and the right-mouse button advances the tilt-series to the previous image ($n - 1$). Click the center mouse button on the image to exit the script.

SYNTAX: CLICKMOVIE, *ArrayName*

### A.3.5 Spatial Tilt-series Alignment

There are two aspects of tilt-series alignment. The first procedure aligns a feature visible in every image to the same spatial position. We use image cross-correlation for automatic spatial alignment and pixel-by-pixel shifting for manual alignment. The procedure aligns all images to a common tilt-axis. The second procedure aligns the tilt-axis

with the horizontal image axis (the x-axis), as required by reconstruction algorithms in IDL.

We recommend logging all alignment procedures applied to a tilt-series in a text file. The alignment process requires iteration and trial-and-error to produce a final, aligned tilt-series, and a log provides a list of accomplished steps to produce a specific alignment. This is very useful for reproducing or verifying a particular alignment at a later date.

**Rough Spatial Alignment: Automatic**

Automatic image registration by cross-correlation of sequential tilt images provides the first approximation of a spatial alignment. The **ALIGN_SEQUENTIAL.PRO** script calculates the cross-correlation of an image at tilt $n$ with the image at tilt $n + 1$, and measures the shift of the cross-correlation peak from the center. The procedure starts at the first image in the series ($n = 0$) and yields a second data array of shifted images. We recommend setting the optional argument to a variable name (such as *shifts1*) to save the alignment shifts, useful to reproduce this alignment with the SHIFTS keyword of **MRC.PRO**.

SYNTAX: ALIGN_SEQUENTIAL, *InputArray*, *OutputArray*, [*ShiftsArray*]

Account for the binning of the data cube used for this rough alignment with respect to the original data, because the **MRC.PRO** script shifts images before binning. If the original images were binned by two then multiply each shift value in the *shifts1* array by two. Otherwise, the **MRC.PRO** script shifts the original data by one-half the correct number of pixels, yielding an incorrect alignment.

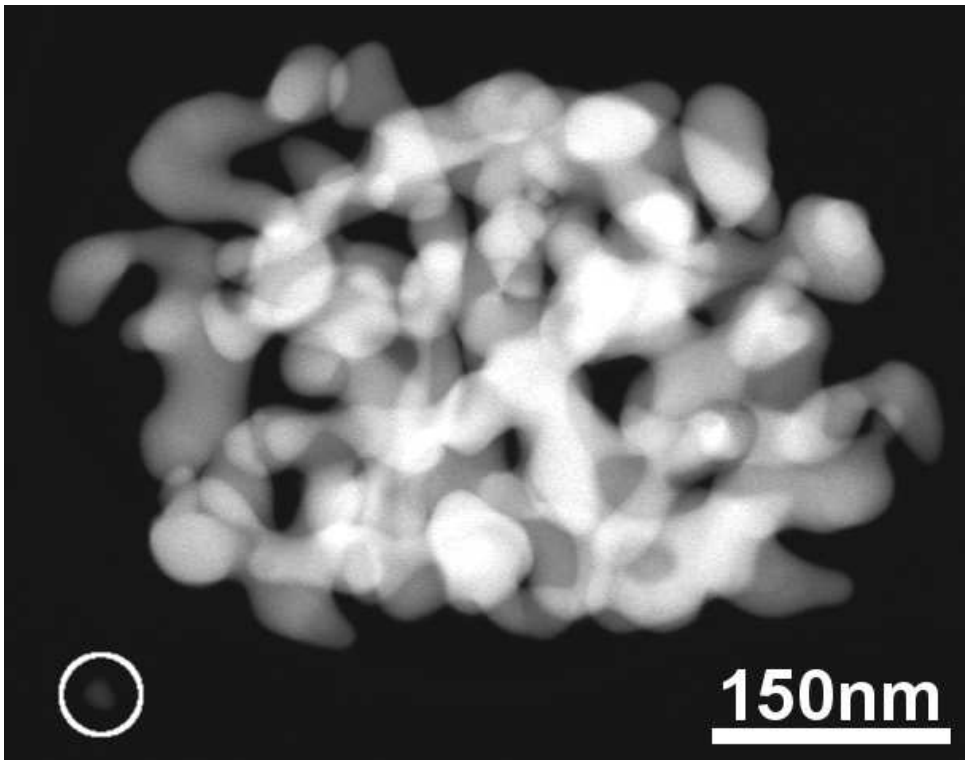


Figure A.7: HAADF-STEM image of a porous Au particle at 0° tilt. The small Au particle in the lower left is circled in white and is visible in all tilt-series images. This feature provides an ideal marker for manual spatial tilt-series alignment.

The overall alignment process is iterative, and each set of alignments (automatic or manual) should be saved in separate arrays (shifts1, shifts2, shifts3, etc.). An alignment that fails to improve the overall spatial alignment is then easily ignored. Aggregate all shifts from every spatial alignment in one array named *total_shifts*, but account for binning when adding them together. An example command for adding shifts measured from a tilt-series binned by 2 is: **total_shifts = shifts1*2**

**Rough Spatial Alignment: Manual**

The **MAN_CORR_SEQ** script allows manual pixel-by-pixel alignment of sequential tilt images and is best used to correct large errors uncorrected or introduced by automatic cross-correlation.

SYNTAX: MAN_CORR_SEQ, *Inputarray*, *Outputarray*, [*ShiftsArray*]

Choose a single feature visible in all images throughout the tilt-series such as the small Au particle circled in the lower left corner of figure A.7. Shift this feature to approximately the same spatial coordinates in every image to ensure an accurate spatial alignment, but notice that the feature need not be located at the center of the image. Any feature is a possible alignment mark regardless of its distance from the image center, but it must be visible in every image of the tilt-series.

**Check Rough Spatial Alignment**

View each exposure image in rapid succession with the script **MOVIEF.PRO** along the first axis of the data cube, which shows projection images of the original object at every tilt $\theta$. The object should rotate fairly smoothly about a single (nearly) horizontal axis.

Image representations of the tilt-series data cube along the other two axes also reveal the alignment quality. The data cube has three perpendicular axes that do not all measure spatial distances. The first axis has size $n$ equal to the number of tilt images and is referred to as the *$\theta$-axis*. The second axis has size $M$ equal to the image size and is referred to as the *x-axis*, which is nearly parallel to the tilt-axis. The third axis has size $M$ equal to the image size and is referred to as the *r-axis* to indicate distance from the tilt-axis.

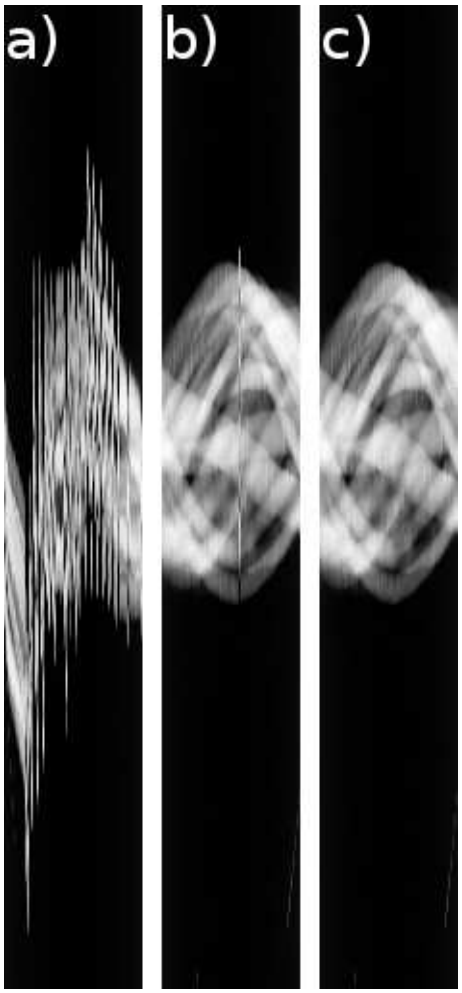


Figure A.8: Three image representations of the porous Au particle as viewed along the tilt-axis of the data cube, which show the projected intensity measured at a given tilt-angle $\theta$ at varying distances $r$ from the tilt axis. The horizontal image axes is the $\theta$-axis and the vertical image axis is the $r$-axis. a) The center sinogram of the original tilt-series with no spatial alignments. b) The center sinogram of the tilt-series after automatic spatial alignment. Only one major misalignment is seen near the center of the sinogram. b) All large misalignments are corrected and features roughly follow sinusoidal paths from left to right.

Image representations of the data cube along the tilt-axis are called *sinograms* and show the projected intensity measured at a given tilt-angle $\theta$ at varying distances $r$ from the tilt-axis. Figure A.8a) shows the center sinogram of the original data cube before any spatial alignments. The horizontal axis is the $\theta$-axis, and the vertical axis is the $r$-axis. The image is quite confused and shows complete misalignment of all features. Figure A.8b) shows the same sinogram after a first-pass automatic cross-correlation alignment (see section A.3.5) with only one major misalignment near the center $\theta$-slice, which is corrected in figure A.8c). A well aligned tilt-series shows roughly sinusoidal movements of features with the form $r = cos(\theta)$ in corresponding sinograms.

**Fine Spatial Alignment: Automatic**

Fine alignment procedures begin once all large shifts are removed from the tilt-series. The sequential rough alignment by **MAN_CORR_SEQ.PRO** does not correct for sub-pixel alignment and can introduce a slow spatial drift in one direction from tilt to tilt. The fine alignment procedure starts at the 0° tilt-image (call this $n = n_0$) and aligns subsequent tilts out to each extreme tilt-angle independently. A structure appears stretched by $1/cos(\theta)$ perpendicular to the tilt-axis with respect to the 0° structure, which affects accurate image registration. The **TOMO_ALIGN.PRO** script corrects for this distortion to remove small misalignments and allows fine automatic or manual alignment starting from the 0° projection image with optional stretching.

SYNTAX: TOMO_ALIGN, *InputArray*, *OutputArray*, *AnglesArray*, [*ShiftsOutput*]

The script offers five different alignment methods based on the desired stretching algorithm and reference image for each cross-correlation. The first three alignment methods start at the 0° tilt image ($n_0$) and align images sequentially at each tilt $n$ to

the previous tilt $n - 1$. "Stretch based on whole tilt range" stretches each image by the exact angles at each tilt in the *AnglesArray*, and "Stretch based on tilt increment" assumes regular tilt increments between each image. "No stretch" aligns images without correcting for $1/cos(\theta)$ stretch distortions. The last two methods align the structure at each tilt angle $n$ to the 0° tilt image $n_0$ with or without stretching. The tilt-axis is the "x" axis in most cases. Initially input "n" to initiate an automatic alignment, but produce the final alignment by manual shifting with this script. Sobel, high-pass and band-pass filters enhance feature edges, sharp small points and large features respectively. Experiment with each filter to determine which best enhances the desired features for your specific structures. Apply the automatic **TOMO_ALIGN** procedure iteratively to the resulting *OutputArray* to further refine the alignment. Save each iterative *ShiftsArray* as separate variables, and add them to the *total_shifts* array properly (accounting for binning).

**Sub-pixel Alignment**

Image binning applied during data import with the **MRC.PRO** script controls the accuracy of the alignment. Images binned 2× are aligned to two pixel accuracy. Import the data with **MRC.PRO** with an image size larger than the native resolution (such as 2048 × 2048) for sub-pixel alignment, but the resulting data cube displaces a large amount of memory. The SUB keyword allows sub-pixel binning with smaller image sizes. For example, import the original data with the command **MRC, ser, SUB = 512, SHIFTS = total_shifts** and image size 1024. The script first aligns the original tilt-series according to *total_shifts*, selects the center 512 × 512 portion of each image and scales/interpolates each image to 1024 × 1024 pixels. The **TOMO_ALIGN** procedure

therefore calculates alignments with sub-pixel accuracy, and the resulting *ShiftsArray* should be multiplied by 0.5 before being added to *total_shifts*.

### Fine Spatial Alignment: Manual

The fine automatic alignment procedures usually yield good alignments, but can leave small random 0.5 – 1 pixel shifts between images at different tilts. Inspect the aligned image stack at full pixel resolution with **MOVIEF.PRO** and/or **CLICKMOVIE.PRO** while paying attention to fine jitter between images. Manual alignment of a single well-defined feature visible at every tilt-angle (such as the small Au particle circled in the lower left corner of figure A.7) should provide a nearly perfect, smooth alignment. Shift such a feature to the same spatial coordinates in every image using the manual option of the **TOMO_ALIGN** script without stretching. Use the *a, z, o, p* keys to shift each image one pixel up, down, left and right respectively, and continue to the next tilt angle by pressing *q*. Ignore movement of all other features, and focus on aligning only the selected feature. Any feature provides an acceptable alignment mark regardless of its distance from the image center, but it must be visible in every image of the tilt-series. The tilt-axis adjustment in section A.3.6 compensates for the location of this feature with respect to the center of the image.

Often, a manual alignment introduces a slow drift of the feature due to biased, single-pixel misalignments in the same direction throughout a tilt-series. Ignore all other features in the image and align the same feature to the same pixel, or spatial coordinates, in every image.

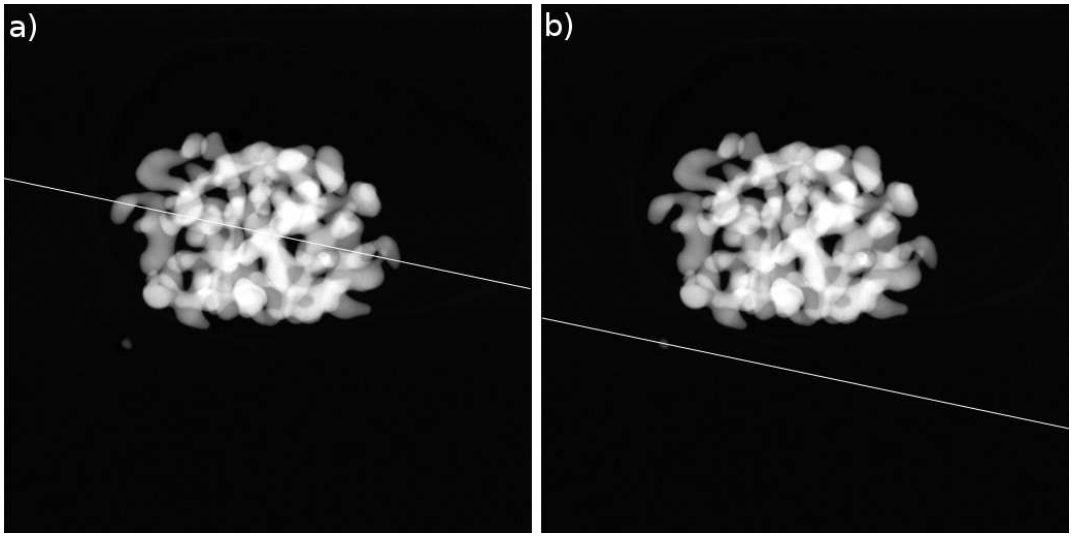


Figure A.9: Two HAADF-STEM images of the porous Au particle with overlays of the tilt-axis location and angle $\psi$ shown as white lines. a) Automatic alignment as in section A.3.5 shifts the tilt-axis - as a first guess - nearly to the center of the object, but the exact location is not guaranteed. The location of the tilt-axis is more difficult to guess for less well defined, compact objects such as this large porous Au particle. b) Manual alignment to a small point-like object - such as the small Au particle to the lower left of the larger porous Au particle - shifts the tilt-axis along the vertical direction to this feature, but the angle $\psi$ is maintained.

### A.3.6 Tilt-Axis Determination

The tomography "Stage Shift Calibration" procedure described in section A.1.2 sets the STEM scan rotation such that the horizontal image axis is nearly parallel with the stage's tilt-axis - usually within $\pm 5^\circ$. Post-processing spatial alignment procedures align a certain feature onto the same tilt-axis in every image. Automatic spatial alignments tend to align the object onto a tilt-axis running through the object's center, but manual fine alignments shift the tilt-axis vertically such that it passes through this feature. Figure A.9 shows the $0^\circ$ tilt image with the tilt-axis superimposed as a white line at an angle $\psi$

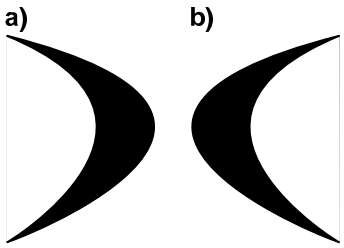


Figure A.10: Two common *crescent*-like distortions of a round object due to misalignment of the tilt-axis. a) Left-pointing and b) right-pointing tails indicate both vertical misalignments and a tilt-axis that is not parallel with the horizontal image-axis. More complex distortions are possible, but the two shown are the most common.

with respect to the horizontal image axis. Automatic spatial alignment tends to align the tilt-axis through the center of the object as seen in figure A.9a), but this is only a first guess. Further investigation is necessary to determine the exact location of the tilt-axis even for automatic alignments. Manual spatial alignments shifts the tilt-axis along the vertical axis - still at the angle $\psi$ - to the feature used for alignment as seen in figure A.9b). Thus, determination of the tilt-axis involves two independent variables: vertical displacement $d$ and angle $\psi$.

**Tilt-axis Alignment**

Analysis of the aligned tilt-series summed along the $\theta$-axis gives a rough estimate of $\psi$. View the summed tilt-series along the $\theta$-axis with the command **im, total(*SeriesName*, 1)**. Objects rotated around an axis move perpendicular to that axis when viewed as a series of projection images. Thus, the object will appear smeared-out perpendicular to the tilt-axis in a summation of all projection images. Measure the general angle of the smear for a rough estimation of the tilt-axis angle $\psi$.

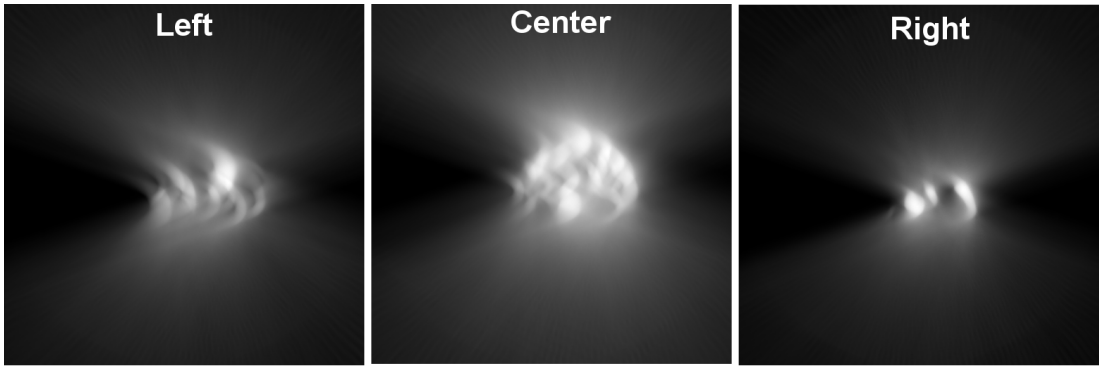


Figure A.11: Three images showing reconstructions of the left, right and center slices respectively from the **TOMO_AXIS.PRO** script. In this first set, neither the tilt-axis location $d$ nor the tilt-angle $\psi$ are correctly determined. Features exhibit distortions with *crescent*-like tails to the left in all thrre images (see figure A.10), which indicates negative pixel shifts along the vertical image-axis are necessary.

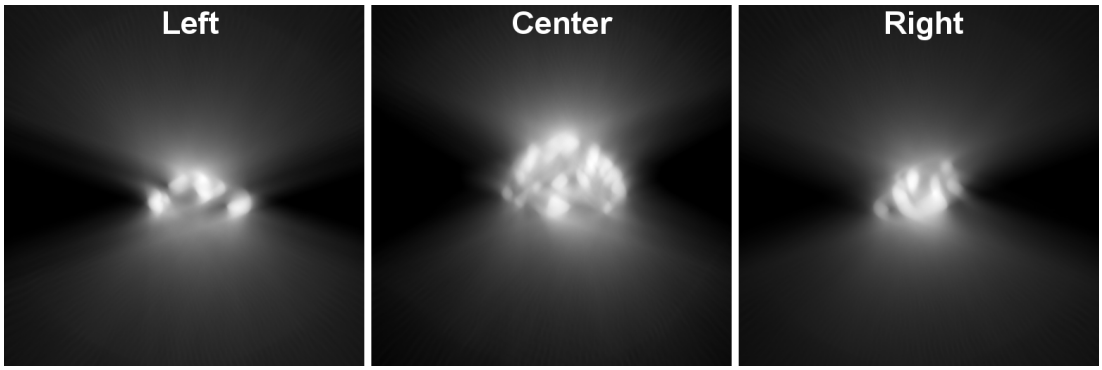


Figure A.12: Three images showing reconstructions of the left, right and center slices respectively from the **TOMO_AXIS.PRO** script. Correct distortions with right- and left-pointing tails in the center image (ignoring the left and right images) with the *a* and *z* keys respectively. We shifted the data $-16$ pixels to minimize left-pointing distortions similar to figure A.10a); compare the corrected center image in this figure to the misaligned features in figure A.11. Similar distortions are still seen in the left and right images, because the tilt-axis is rotated at an angle $\psi$ with respect to the horizontal image axis.

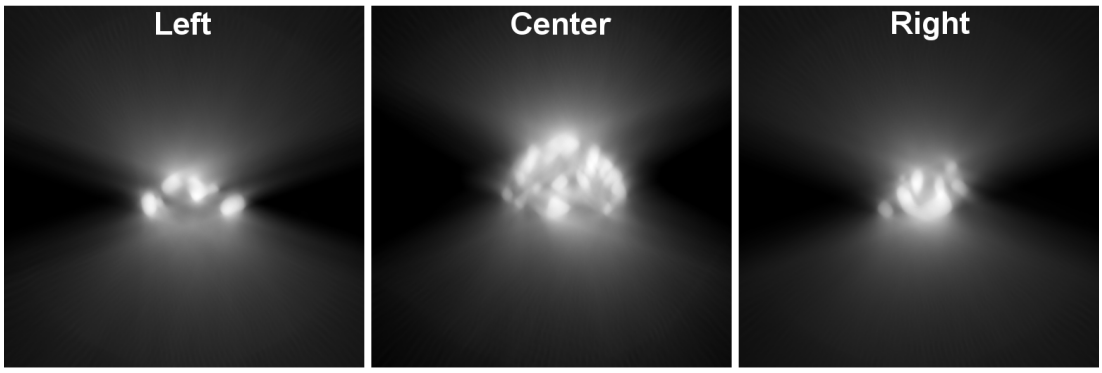


Figure A.13: Three images showing reconstructions of the left, right and center slices respectively from the **TOMO_AXIS.PRO** script. We have corrected for distortions with right- or left-pointing tails in the left image with the *o* or *p* keys, respectively. Equivalently, correct for distortions with right- or left-pointing tails in the right image with the *p* or *o* keys, respectively. We applied a rotation of $-4.55^\circ$ to produce the final tilt-axis alignment seen in this figure. Compare all three images to the corresponding images in figures A.11 and A.12.

The script **TOMO_ AXIS.PRO** allows a more accurate determination of the tilt-axis location and angle $\psi$.

SYNTAX TOMO_ AXIS, *ArrayName, AnglesArray*

The script initially shows the $0^\circ$ STEM image and asks the user to choose one high-intensity feature on the left side and right side of the image center. The script then shows four windows: reconstructions of the left, center and right slices chosen by the user and the $0^\circ$ STEM projection image. The user shifts the tilt-axis up and down with the *a* and *z* keys respectively, and the user rotates the tilt-axis counter-clockwise and clockwise with the *o* and *p* keys respectively. Press the *w* key to apply a weighting filter to the slices, which usually enhances features for alignment but also increases computation time between shifts/rotations.

The general tilt-axis alignment method involves first shifting the tilt-axis vertically to minimize *crescent*-like distortions (see figure A.10) in the center slice, and then rotating the tilt-axis to minimize similar distortions in the left and right slices. Figure A.11 shows the three reconstructed slices without any alignment of the tilt-axis. *Crescent*-like distortions with left-pointing tails - similar to figure A.10a) - are visible in the center slice. Figure A.12 shows the tilt-axis shifted $-16$ pixels to minimize the distortions in the center slice, but similar distortions are still visible in the left and right slices. Figure A.13 shows the tilt-axis rotated to $-4.55^\circ$ (including the $-16$ pixel shift) which corrects the distortions in the left and right slices. The location and angle of the tilt-axis are now determined, but the script only indicates the necessary shift and rotation corrections. The user often applies this method many times ensuring an accurate alignment, and each set of values is noted in the alignment log.

This script uses an approximation ($sin(\theta) = \theta$) to speed up computation, and the script should not be used to correct rotations above $\sim 5^\circ$. Instead, use the **ROT3D.PRO** script (described below) to rotate the tilt-series by large angles $\geq 5^\circ$ before using **TOMO_AXIS.PRO** to fine tune the rotation.

Once the user settles on $d$ and $\psi$, the original data is properly shifted and rotated. First, add the proper vertical shift to the y-axis values of the *total_shifts* array with the command: **total_shifts(1,*) = total_shifts + *scalar*** where the *scalar* is the pixel value $d$. Account for the binning of the data cube used for tilt-axis alignment when adding the vertical shift to the *total_shifts* array. Second, rotate the data cube with the **ROT3D.PRO** script.

SYNTAX ROT_3D, *InputArray*, *OutputArray*, *Angle*

where the *Angle* argument is $\psi$ with units of degrees. Always rotate the array around the first (1) axis, the $\theta$-axis. All tilt-series alignments are now complete, and three-

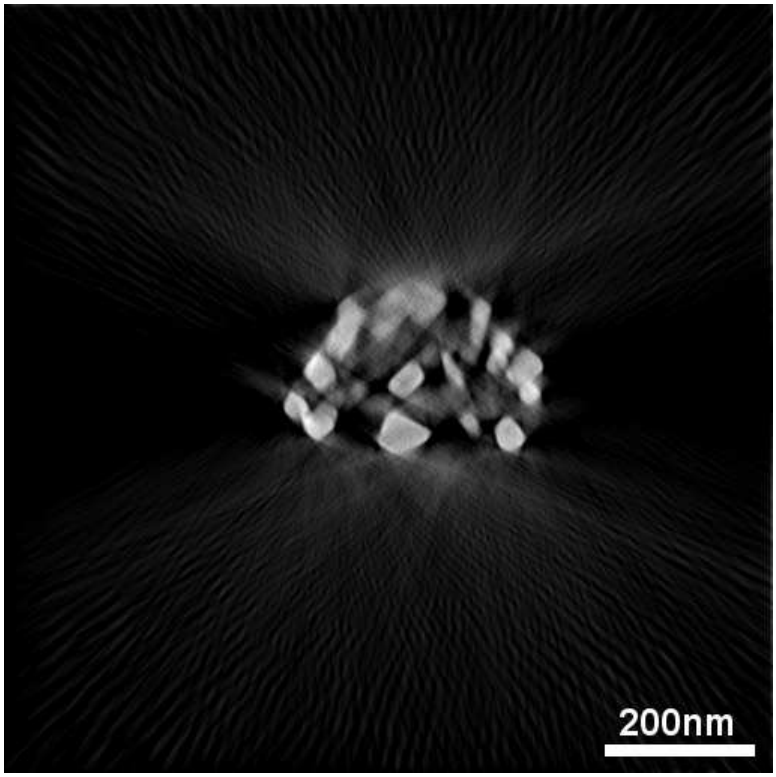


Figure A.14: The central slice of a weighted back-projection reconstruction of the porous Au particle as seen along the tilt-axis. The vertical image axis is the original 0° projection direction. The reconstruction includes extraneous intensity above and below the particle due to the discrete number of projection images and the missing wedge of information (see section 1.5)

dimensional reconstruction can commence. Backup all data in IDL's memory with the **SAVE** command before continuing.

## A.4 Tomographic Reconstruction

### A.4.1 Weighted Back-projection Reconstruction

The details of the following reconstruction methods are described in section 1.5. The weighted back-projection method provides an initial, rapid reconstruction of the tilt-series to ensure the quality of the alignment. The **TOMO_RADONWB.PRO** script implements the weighted back-projection algorithm using IDL's built-in **RADON** function, which allows the user to specify the location of the tilt-axis.

SYNTAX: TOMO_RADONWB, *InputArray*, *AnglesArray*, [AXISCENTER = *scalar*]

The optional *AXISCENTER* keyword specifies the horizontal pixel row corresponding to the location of the tilt-axis, and the default value is the image center ($M/2$). Positive scalars locate the tilt-axis above the image center, and negative scalars locate the tilt-axis below the image center. This advanced and optional feature allows the user to shift the tilt-axis along the vertical image axis after rotation to center any object without affecting the alignment. Input a filename for the output reconstruction data, which is written as 32-bit float binary data. Include all relevant information regarding the reconstruction in the filename, such as the pixel size along all three dimensions of the output reconstruction and the reconstruction method: 1RoundParticle_flt512,512,512.WB. This example filename implies a reconstruction of one round particle with $512 \times 512 \times 512$ pixels of float numbers created by weighted back-projection - all necessary information to read the binary data file for visualization and analysis. Load a reconstruction into IDL by creating an empty array of the proper type/size named *rec*, opening the file to read, loading the data and closing the file. Use the following example commands in IDL:

```
rec = fltarr(512,512,512)
openr, 1, '1RoundParticle_flt512,512,512.WB'
readu, 1, rec
close, 1
```

Figure A.14 shows a central slice through a weighted back-projection reconstruction of the Au particle seen along the tilt-axis. The original projection direction is equivalent to the vertical image axis. The reconstruction includes artifacts, such as extraneous intensity above and below the particle, due to the discrete number of projection images and the missing wedge of information (see section 1.5). These artifacts are common to weighted back-projection reconstructions.

### A.4.2 Iterative Reconstruction

Iterative reconstruction methods require more time but produce high-quality results for analytical analysis. The **TOMO_RADON.PRO** command implements the simultaneous iterative reconstruction technique (SIRT) algorithm, described in section 1.5.3 and figure 1.15, using IDL's built-in **RADON** function. This script also allows the user to specify the location of the tilt-axis as described in the previous section.

SYNTAX: TOMO_RADON, *InputArray*, *AnglesArray*, [AXISCENTER = *scalar*]

The user must enter the desired number of iterations, which value varies from 10 – 30 depending on the specimen and signal-to-noise of the original tilt-series projection images. The user determines the number of iterations necessary to produce a clear reconstruction by watching the iteration process on-screen. Interrupt the script and restart the process with the optimized number of iterations.

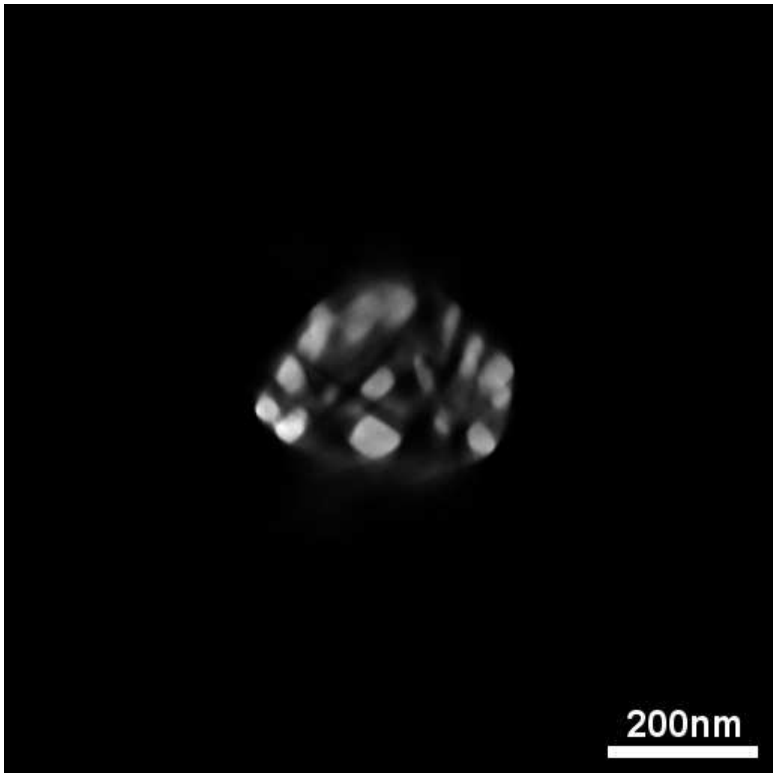


Figure A.15: The central slice of a simultaneous iterative reconstruction technique (SIRT) algorithm reconstruction of the porous Au particle as seen along the tilt-axis. The vertical image axis is the original 0° projection direction. The reconstruction is slightly more blurred compared to the weighted back-projection reconstruction seen in figure A.14, but excludes reconstruction artifacts (see section 1.5).

Figure A.15 shows a central slice through the SIRT reconstruction of the Au particle as seen along the tilt-axis with less extraneous intensity compared to the weighted pack-projection reconstruction in figure A.14. Figure A.16 is a three-dimensional representation of the Au particle's surface. The perspective view shows the three-dimensional porous structure not possible from two-dimensional projections. The *isosurface* module in the Avizo 6.0 software environment from Mercury Computer Systems was used to produce this visualization.

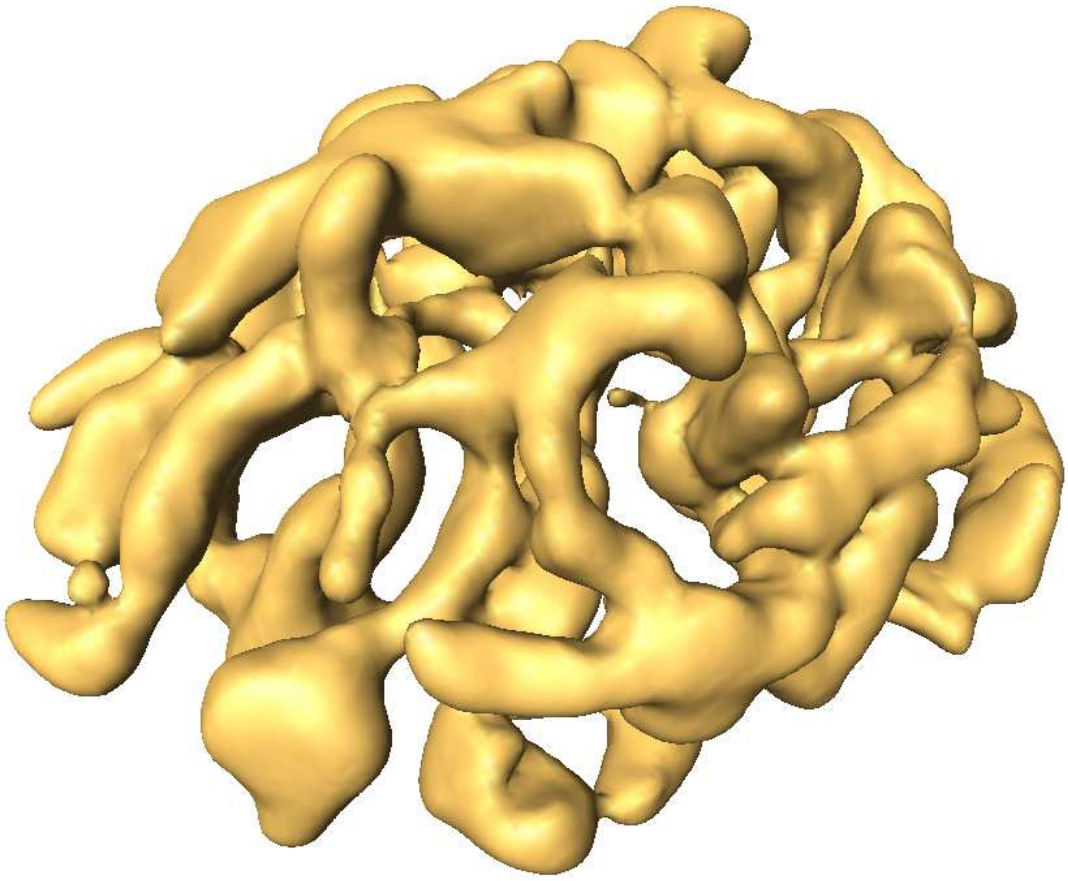

Figure A.16: Perspective view of the thresholded HAADF-STEM three-dimensional reconstruction of a Au porous particle, which maps the Au surface. The *isosurface* module in the Avizo 6.0 software environment from *Mercury Computer Systems* was used to produce this visualization.

## BIBLIOGRAPHY


[1] International Roadmap Committee. *International Technology Roadmap for Semiconductor*, 2007. http://www.itrs.net.

[2] P.A. Midgley and M. Weyland. 3d electron microscopy in the physical sciences: the development of z-contrast and eftem tomography. *Ultramicroscopy*, 96:413–431, 2003.

[3] Hiroshi Jinnai, Yukihiro Nishikawa, Richard J. Spontak, Steven D. Smith, David A. Agard, and Takeji Hashimoto. Direct measurement of interfacial curvature distributions in a bicontinuous block copolymer morphology. *Physical Review Letters*, 84(3):518, 2000.

[4] Peter Ercius, Lynne M. Gignac, C.-K. Hu, and David A. Muller. Three-dimensional measurement of line edge roughness in copper wires using electron tomography. *Microscopy and Microanalysis*, 2009.

[5] Peter Ercius, Matthew Weyland, David A. Muller, and Lynne M. Gignac. Three-dimensional imaging of nanovoids in copper interconnects using incoherent bright field tomography. *Applied Physics Letters*, 88:243116, 2006.

[6] Gordon E. Moore. Cramming more components onto integrated circuits. *Electronics*, 38(8), 1965.

[7] Shyam P. Murarka, Igor V. Verner, and Ronald J. Gutman. *Copper-Fundamental Mechanisms for Microelectronic Applications*. John Wiley and Sons, Inc., New York, 2000.

[8] Andrea Scorzoni, Bruno Neri, Candida Caprile, and Fausto Fantini. Electromigration in thin-film interconnection lines: models, methods and results. *Materials Science Reports*, 7(4-5):143–220, 1991.

[9] C.-K. Hu, K.P. Rodbell, T.D. Sullivan, K.Y. Lee, and D.P. Bouldin. Electromigration and stress-induced voiding in fine al and al-alloy thin-film lines. *IBM Journal of Research and Development*, 39(4):465–497, 1995.

[10] D.A. Porter and K.E. Easterling. *Phase Transformations in Metals and Alloys*. Chapman and Hall, London, 2nd edition, 1992.

[11] C. K. Hu and J. M. E. Harper. Copper interconnections and reliability. *Materials Chemistry and Physics*, 52(1):5–16, 1998.

[12] Dan Edelstein, J. Heidenreich, R. Goldblatt, C. Cote, N. Lustig, P. Roper, T. McDevitt, W. Motsiff, A. Simon, J. Dukovic, R. Wachnik, H. Rathore, R. Schulz, L. Su, S. Luce, and J. Slattery. Full copper wiring in a sub-0.25um cmos ulsi technology. In *International Electron Devices Meeting*, pages 773–776, 1997.

[13] R. Rosenberg, D.C. Edelstein, C.-K. Hu, and K.P. Rodbell. Copper metallization for high performance silicon technology. *Annual Review of Materials Science*, 30:229–262, 2000.

[14] Jon Reid, Steve Mayer, Eliot Broadbent, Erich Klawuhn, and Kaihan Ashtiani. Factors influencing damascene feature fill using copper pvd and electroplating. *Solid State Technology*, 43(7):86–98, 2000.

[15] Stephen Campbell. *The Science and Engineering of Microelectronic Fabrication*. Oxford University Press, London, 2nd edition, 2001.

[16] J.M. Steigerwald, Shyam P. Murarka, and Ronald J. Gutman. *Chemical Mechanical Planarization of Microelectronic Materials*. John Wiley and Sons, New York, 1997.

[17] Parshuram B. Zantye, Ashok Kumar, and A. K. Sikder. Chemical mechanical planarization for microelectronics applications. *Materials Science and Engineering: R: Reports*, 45(3-6):89–220, 2004.

[18] M.R. Oliver, editor. *Chemical-Mechanical Planarization of Semiconductor Materials*. Springer, New York, 2004.

[19] Kazuaki Suzuki and Bruce W. Smith, editors. *Microlithography: Science and Technology*. CRC Press, 2nd edition, 2007.

[20] Marc Madau. *Fundamentals of Microfabrication*. CRC Press, Boca Raton, 1997.

[21] Stephen A. Campbell. *Fabrication Engineering at the Micro- and Nanoscale*. Oxford University Press, New York, 3rd edition, 2008.

[22] Panos C. Andricacos. Copper on-chip interconnections. *The Electrochemical Society Interface*, 8(1):32–37, 1999.

[23] Yuan Taur and Tak H. Ning. *Fundamentals of Modern VLSI Devices*. Cambridge University Press, Cambridge, 1998.

[24] S.M. Sze and Kwok K. Ng. *Physics of Semiconductor Devices*. Wiley-Interscience, Hoboken, third edition, 2007.

[25] Dan Edelstein, C. Uzoh, C. Cabral, P. DeHaven, P. Buchwalter, A. Simon, E. Cooney, S. Malhotra, D. Klaus, H. Rathore, B. Agarwala, and D. Nguyen. A higher performance liner for copper damascene interconnects. In *International Interconnect Technology Conference*, pages 9–11, Burlingame, CA, 2001. IEEE.

[26] A. E. Kaloyeros and E. Eisenbraun. Ultrathin diffusion barriers/liners for gigascale copper metallization. *Annual Review of Materials Science*, 30(1):363, 2000.

[27] J. M. E. Harper, Jr. C. Cabral, P. C. Andricacos, L. Gignac, I. C. Noyan, K. P. Rodbell, and C. K. Hu. Mechanisms for microstructure evolution in electroplated copper thin films near room temperature. *Journal of Applied Physics*, 86(5):2516–2525, 1999.

[28] C. K. Hu, L. Gignac, and R. Rosenberg. Electromigration of cu/low dielectric constant interconnects. *Microelectronics and Reliability*, 46(2-4):213–231, 2006.

[29] J. Proost, T. Hirato, T. Furuhara, K. Maex, and J. P. Celis. Microtexture and electromigration-induced drift in electroplated damascene cu. *Journal of Applied Physics*, 87(6):2792–2802, 2000.

[30] C. S. Hau-Riege and C. V. Thompson. Electromigration in cu interconnects with very different grain structures. *Applied Physics Letters*, 78(22):3451–3453, 2001.

[31] C.-K. Hu, L. Gignac, S. Malhotra, E. Liniger, and A.K. Stamper. Scaling rule for electromigration in cu dual-damascene interconnects on w. In *Advanced Metallization Conference*, page 139, Montreal, CA, 2003. Materials Research Society.

[32] C. K. Hu, L. Gignac, R. Rosenberg, E. Liniger, J. Rubino, C. Sambucetti, A. Domenicucci, X. Chen, and A. K. Stamper. Reduced electromigration of cu wires by surface coating. *Applied Physics Letters*, 81(10):1782–1784, 2002.

[33] Christine S. Hau-Riege. An introduction to cu electromigration. *Microelectronics Reliability*, 44(2):195–205, 2004.

[34] C.-K. Hu, L.M. Gignac, R. Rosenberg, B. Herbst, S. Smith, J. Rubino, D. Canaperi, S.T. Chen, S.C. Seo, and D. Restaino. Atom motion of cu and co in cu damascene lines with a cowp cap. *Applied Physics Letters*, 84(24):4986–4988, 2004.

[35] P. Borgesen, J. K. Lee, R. Gleixner, and C. Y. Li. Thermal-stress-induced voiding in narrow, passivated cu lines. *Applied Physics Letters*, 60(14):1706–1708, 1992.

[36] Baozhen Li, Timothy D. Sullivan, Tom C. Lee, and Dinesh Badami. Reliability challenges for copper interconnects. *Microelectronics Reliability*, 44(3):365–380, 2004.

[37] K.Y.Y. Doong, R.C.J. Wang, S.C. Lin, L.J. Hung, C.C. Chiu, D. Su, K. Wu, K.L. Young, and Y.K. Peng. Stress-induced voiding and its geometry dependency characterization. In *International Reliability Physics Symposium*, pages 156–60. IEEE, 2003.

[38] F. Chen, B. Li, T. Lee, C. Christiansen, J. Gill, M. Angyal, M. Shinoskyl, C. Burke, W. Hasting, R. Austin, T. Sullivan, D. Badami, and J. Aitken. Technology reliability qualification of a 65nm cmoscu/low-k beol interconnect. In *International Symposium on the Physical and Failure Analysis of Integrated Circuits (IPFA)*, volume 13, pages 97–105. IEEE, 2006.

[39] E.T. Ogawa, J.W. McPherson, J.A. Rosal, K.J. Dickerson, T.-C. Chiu, L.Y. Tsung, M.K. Jain, T.D. Bonifield, J.C. Ondrusek, and W.R. McKee. Stress-induced voiding under vias connected to wide cu metal leads. In *International Reliability Physics Symposium*, pages 312–321, Dallas, TX, 2002. IEEE.

[40] Werner Steinhogl, Gunther Schindler, Gernot Steinlesberger, and Manfred Engelhardt. Size-dependent resistivity of metallic wires in the mesoscopic range. *Physical Review B*, 66:075414, 2002.

[41] L.M. Gignac, C.-K. Hu, B.W. Herbst, and B.C. Baker-O'Neal. The effect of microstructure on resistivity and reliability in copper interconnects. In A.J. McKerrow, Y. Shacham-Diamand, S. Shingubara, and Y. Shimogaki, editors, *Advanced*

*Metallization Conference 2007*, Berkeley, California, 2007. Materials Research Society.

[42] W.F.A. Besling, M. Broekaart, V. Arnal, and J. Torres. Line resistance behaviour in narrow lines patterned by a tin hard mask spacer for 45nm node interconnects. *Microelectronic Engineering*, 76:167–174, 2004.

[43] Kenji Hinode, Yuko Hanaoka, Ken-ichi Takeda, and Seiichi Kondo. Resistivity increase in ultrafine-line copper conductor for ulsis. *Japanese Journal of Applied Physics*, 40(10B):L1097–L1099, 2001.

[44] Choong-Un Kim, Jaeyong Park, Nancy Michael, Paul Gillespie, and Rod Augur. Study of electron-scattering mechanism in nanoscale cu interconnects. *Journal of Electronic Materials*, 32(10):982–987, 2003.

[45] L.H.A. Leunissen, W. Zhang, W. Wu, and S.H. Brongersma. Impact of line edge roughness on copper interconnects. *Journal of Vacuum Science and Technology B*, 24(4):1859–1862, 2006.

[46] H. Marom, J. Mullin, and M. Eizenberg. Size-dependent resistivity of nanometric copper wires. *Physical Review B*, 74:045411, 2006.

[47] J.J. Plombon, E. Andideh, V.M. Dubin, and J. Maiz. Influence of phonon, geometry, impurity, and grain size on copper line resistivity. *Applied Physics Letters*, 89:113124, 2006.

[48] Werner Steinhogl, Gunther Schindler, M. Traving, and M. Engelhardt. Impact of line edge roughness on the resistivity of nanometer-scale interconnects. *Microelectronic Engineering*, 76:126–130, 2004.

[49] W. Wu, S.H. Brongersma, M. Van Hove, and K. Maex. Influence of surface and grain-boundary scattering on the resistivity of copper in reduced dimensions. *Applied Physics Letters*, 84:2838, 2004.

[50] W. Zhang, S.H. Brongersma, Z. Li, D. Li, O. Richard, and K. Maex. Analysis of the size effect in electroplated fine copper wires and a realistic assessment to model copper resistivity. *Journal of Applied Physics*, 101:063703, 2007.

[51] H.B. Zhang, X.L. Zhang, Y. Wang, and Akio Takaoka. Tomography experiment of an integrated circuit specimen using 3 mev electrons in the transmission electron microscope. *Review of Scientific Instruments*, 78:013701, 2007.

[52] Joseph Goldstein, Dale E. Newbury, David C. Joy, Charles E. Lyman, Patrick Echlin, Eric Lifshin, L.C. Sawyer, and J.R. Michael. *Scanning electron microscopy and X-ray microanalysis*. Springer, 3rd edition, 2003.

[53] P. M. Voyles, J. L. Grazul, and D. A. Muller. Imaging individual atoms inside crystals with adf-stem. *Ultramicroscopy*, 96(3-4):251 – 273, 2003. Proceedings of the International Workshop on Strategies and Advances in Atomic Level Spectroscopy and Analysis.

[54] Lucille A. Gianuzzi and Fred A. Stevie. *Introduction to Focused Ion Beams: Instrumentation, Theory, Techniques and Practice*. Springer, New York, 2004.

[55] David B. Williams and C. Barry Carter. *Transmission Electron Microscopy: A Textbook for Materials Science*. Springer, New York, 2004.

[56] John M. Cowley. Image contrast in a transmission scanning electron microsocpe. *Applied Physics Letters*, 15(2):58–59, 1969.

[57] E. Zeitler and M.G.R. Thomson. Scanning transmission electron microscopy. *Optik*, 31:258–366, 1970.

[58] A. Engel. The principle of reciprocity and its application to conventional and scanning dark field electron microscopy. *Optik*, 41:117–126, 1974.

[59] Earl J. Kirkland, Russell F. Loane, and John Silcox. Simulation of annular dark field stem images using a modified multislice method. *Ultramicroscopy*, 23(1):77–96, 1987.

[60] Earl J. Kirkland and Malcolm G. Thomas. A high efficiency annular dark field detector for stem. *Ultramicroscopy*, 62:79–88, 1996.

[61] A. Howie. Image contrast and localized signal selection techniques. *Journal of Microscopy*, 117:11–23, 1979.

[62] Judy J. Cha, Matthew Weyland, Jean-Francois Briere, Ivan P. Daykov, Tomas A. Arias, and David A. Muller. Three-dimensional imaging of carbon nanotubes deformed by metal islands. *Nano Letters*, 7(12):3770–3773, 2007.

[63] Joachim Frank. Introduction: Principles of electron tomography. In Joachim Frank, editor, *Electron Tomography: Methods for Three-Dimensional Visualization of Structures in the Cell*, pages 1–15. Springer, New York, 2006.

[64] Han Sung Kim, Seon Oh Hwang, Yoon Myung, Jeunghee Park, Seung Yong Bae, and Jae Pyoung Ahn. Three-dimensional structure of helical and zigzagged nanowires using electron tomography. *Nano Letters*, 8(2):551–557, 2008.

[65] Gilman E. S. Toombes, Surbhi Mahajan, Matthew Weyland, Anurag Jain, Phong Du, Marleen Kamperman, Sol M. Gruner, David A. Muller, and Ulrich Wiesner. Self-assembly of four-layer woodpile structure from zigzag abc copolymer/aluminosilicate concertinas. *Macromolecules*, 41(3):852–859, 2008.

[66] Marcel A. Verheijen, Rienk E. Algra, Magnus T. Borgstrom, George Immink, Erwan Sourty, Willem J. P. van Enckevort, Elias Vlieg, and Erik P. A. M. Bakkers.

Three-dimensional morphology of gap-gaas nanowires revealed by transmission electron microscopy tomography. *Nano Letters*, 7(10):3051–3055, 2007.

[67] A.J. Koster, U. Ziese, A.J. Verkleij, A.H. Janssen, and K.P. de Jong. Three-dimensional electron microscopy: A novel imaging and characterization technique with nanometer scale resolution for materials science. *Journal of Physical Chemistry B*, 104:9368–9370, 2000.

[68] P.W. Hawkes. The electron microscope as a structure projector. In Joachim Frank, editor, *Electron Tomography: Three-Dimensional Imaging with the Transmission Electron Microscope*. Plenum Press, New York, 1992.

[69] Noboru Kawase, Mitsuro Kato, Hideo Nishioka, and Hiroshi Jinnai. Transmission electron microtomography without the ”missing wedge” for quantitative structural analysis. *Ultramicroscopy*, 107(1):8–15, 2007.

[70] K. Thompson, D. Lawrence, D. J. Larson, J. D. Olson, T. F. Kelly, and B. Gorman. In situ site-specific specimen preparation for atom probe tomography. *Ultramicroscopy*, 107(2-3):131–139, 2007.

[71] G.T. Herman. *Image Reconstruction from Projections: Implementation and Applications*, volume 32 of *Topics in Applied Physics*. Academic Press, New York, 1979.

[72] R.A. Crowther, D.J. DeRosier, and A. Klug. The reconstruction of a three-dimensional structure from projections and its application to electron microscopy. *Proceedings of the Royal Society of London A*, 317(1530):319 – 340, 1970.

[73] Russell M. Mersereau. Direct fourier transform techniques in 3-d image reconstruction. *Computers in Biology and Medicine*, 6(4):247–258, 1976.

[74] J. Radon. Uber die bestimmung von funktionen durch ihre integralwerte langs gewisser mannigfalttigkeiten. *Berichte Sachsische Akademie der Wissenschaften. Lepizig, Math. - Phys. Kl.*, 69:262–267, 1917.

[75] S.R. Deans. *The Radon Transform and Some of its Applications*. Wiley, New York, 1983.

[76] D.J. DeRosier. The reconstruction of three-dimensional images from electron micrographs. *Contemporary Physics*, 12:437–452, 1971.

[77] Peter W. Hawkes. The electron microscope as a structure projector. In Joachim Frank, editor, *Electron Tomography: Methods for Three-Dimensional Visualization of Structures in the Cell*. Springer, New York, 2006.

[78] Gilbert. Iterative methods for the three-dimensional reconstruction of an object for projections. *Journal of Theoretical Biology*, 36(1):105–117, 1972.

[79] R. F. Egerton, P. Li, and M. Malac. Radiation damage in the tem and sem. *Micron*, 35(6):399–409, 2004.

[80] Bruce F. McEwen, Michael Marko, Chyong-Ere Hsieh, and Carmen Mannella. Use of frozen-hydrated axonemes to assess imaging parameters and resolution limits in cryoelectron tomography. *Journal of Structural Biology*, 138(1-2):47–57, 2002.

[81] Pradeep K. Luther. Sample shrinkage and radiation damage of plastic sections. In Joachim Frank, editor, *Electron Tomography: Methods for Three-Dimensional Visualization of Structures in the Cell*. Springer, New York, 2006.

[82] James E. Evans, Crispin Hetherington, Angus Kirkland, Lan-Yun Chang, Henning Stahlberg, and Nigel Browning. Low-dose aberration corrected cryo-

electron microscopy of organic specimens. *Ultramicroscopy*, 108(12):1636–1644, 2008.

[83] D.L. Misell. Conventional and scanning transmission electron microscopy: Image contrast and radiation damage. *Journal of Physics D: Applied Physics*, 10(8):1085–1107, 1977.

[84] H. Reimer, L. Kohl. *Transmission Electron Microscopy*, volume 36 of *Springer Series in Optical Sciences*. Springer, fifth edition, 2008.

[85] S. Bals, C. Kisielowski, M. Croitoru, and G. Van Tendeloo. Tomography using annular dark field imaging in tem. *Microscopy and Microanalysis*, 11:2118–2119, 2005.

[86] Earl J. Kirkland. *Advanced Computing in Electron Microscopy*. Plenum Press, New York, 1998.

[87] Matthew Weyland. *Two and Three Dimensional Nanoscale Analysis: New Techniques and Applications*. PhD thesis, Cambridge University, 2001.

[88] A.A. Sousa, M.F. Hohmann-Marriott, G. Zhang, and R.D. Leapman. Monte carlo electron-trajectory simulations in bright-field and dark-field stem: Implications for tomography of thick biological sections. *Ultramicroscopy*, 109(3):213 – 221, 2009.

[89] David A. Muller and John Silcox. Radiation damage of ni3al by 100kev electrons. *Philosophical Magazine A*, 71(6):1375–1387, 1995.

[90] Sara Bals, Wim Tirry, Remco Geurts, Zhiqing Yang, and Dominique Schryvers. High-quality sample preparation by low kv fib thinning for analytical tem measurements. *Microscopy and Microanalysis*, 13(2):80–86, 2007.

[91] David Joy. *Monte Carlo Modeling for Electron Microscopy and Microanalysis*. Oxford University Press, New York, 1995.

[92] J.I Goldstein, J.L. Costley, G.W. Lorimer, and S.F.B. Reed. Quantitative x-ray analysis in the electron microscope. In O. Johari, editor, *Scanning Electron Microscopy*, volume 1, page 315. IITRI, Chicago, 1977.

[93] John David Jackson. *Classical Electrodynamics*. John Wiley & Sons, Inc., New York, 3rd edition, 1999.

[94] Lucien Pages, Evelyne Bertel, Henri Joffre, and Laodamas Sklavenitis. Energy loss, range, and bremsstrahlung yield for 10-kev to 100-mev electrons in various elements and chemical compounds. *Atomic Data and Nuclear Data Tables*, 4:1–27, 1972.

[95] David A. Muller. Alternatives to core-loss compositional imaging. In M. Yacaman, editor, *14th International Congress on Electron Microscopy*, Cancun, Mexico, 1998.

[96] Zachary H. Levine. Tomography in the multiple scattering regime of the scanning transmission. *Applied Physics Letters*, 82(22):3943–3945, 2003.

[97] Zachary H. Levine. Theory of bright-field scanning transmission electron microscopy for tomography. *Journal of Applied Physics*, 97(3):033101, 2005.

[98] E. J. Kirkland. Z-contrast in a conventional tem. *Proceedings of Microscopy and Microanalysis*, 2A:1147–1148, 1997.

[99] Personal conversation with E.J. Kirkland at Cornell University.

[100] Ray Egerton. *Electron Energy-Loss Spectroscopy in the Electron Microscope*. Plenum Press, 1996.

[101] L. M. Gignac, M. Kawasaki, S. H. Boettcher, and O. C. Wells. Imaging and analysis of subsurface cu interconnects by detecting backscattered electrons in the scanning electron microscope. *Journal of Applied Physics*, 97(11):114506, 2005.

[102] Varat Intaraprasonk, Huolin L. Xin, and David A. Muller. Analytic derivation of optimal imaging conditions for incoherent imaging in aberration-corrected electron microscopes. *Ultramicroscopy*, 108(11):1454–1466, 2008.

[103] L. Xin Huolin, Intaraprasonk Varat, and A. Muller David. Depth sectioning of individual dopant atoms with aberration-corrected scanning transmission electron microscopy. *Applied Physics Letters*, 92(1):013125, 2008.